University of Arkansas, Fayetteville

ScholarWorks@UARK

Theses and Dissertations

5-2021

Study of static and dynamical properties of complex antiferroelectrics materials

Kinnary Yogeshbhai Patel
University of Arkansas, Fayetteville

Follow this and additional works at: https://scholarworks.uark.edu/etd

 Part of the Ceramic Materials Commons, Condensed Matter Physics Commons, Dynamics and Dynamical Systems Commons, and the Statistical, Nonlinear, and Soft Matter Physics Commons

Citation

Patel, K. Y. (2021). Study of static and dynamical properties of complex antiferroelectrics materials. *Theses and Dissertations* Retrieved from https://scholarworks.uark.edu/etd/3955

This Dissertation is brought to you for free and open access by ScholarWorks@UARK. It has been accepted for inclusion in Theses and Dissertations by an authorized administrator of ScholarWorks@UARK. For more information, please contact ccmiddle@uark.edu.

Study of static and dynamical properties of complex antiferroelectrics materials

A dissertation submitted in partial fulfillment
of the requirements for the degree of
Doctor of Philosophy in Physics

by

Kinnary Yogeshbhai Patel

Sadar Patel University
Bachelor of Science in Electronics, 1994
Maharaja Sayajirao University of Baroda
Master of Applied Physics, 1996
Western Illinois University
Master of Science in Physics, 2014

May 2021
University of Arkansas

This dissertation is approved for recommendation to the Graduate Council.

Laurent Bellaiche, Ph.D.
Dissertation Director

Huaxiang Fu, Ph.D.
Committee Member

Sergey Prosandeev, Ph.D.
Committee Member

Peter Pulay, Ph.D.
Committee Member

Abstract

The aim of this dissertation is the investigation of the static and dynamical properties of the complex antiferroelectric materials using Effective Hamiltonian method and First principles calculations. In chapter 3, a novel elemental interatomic coupling in perovskite materials which bilinearly couples the antiferroelectric displacements of cations with the rotations of the oxygen octahedra. This new coupling explains a very complex crystal structure of prototypical antiferroelectric $PbZrO_3$. My explanation provides a unified description of many other complex antipolar crystal structures in variety of perovskite materials, including the occurrence of incommensurate phases in some of them. In chapter 4, results and analysis of atomistic simulations explaining the dynamics of antiferroelectric distortions in $BiFeO_3$ (BFO) bulk under hydrostatic pressure are reported. This system undergoes a phase transition on cooling from paraelectric $Pm\bar{3}m$ state at high temperatures to an intermediate $P4/mbm$ phase followed by *Pnma* state at low temperatures. On the basis of my calculations, I prepared an analytical model of these phase transitions. The model developed can be easily applied to predict dynamics of antipolar cation motion in improper ferroelectrics. I found out that the antipolar modes do not soften themselves in the high temperature regime but they soften in the intermediate and *Pnma* phases, due to trilinear energetic coupling term. In chapter 5, the finite temperature behavior of the polar, antipolar, and antiferrodistortive phonons in a prototypical hybrid improper ferroelectric $(BiFeO_3)_1/(NdFeO_3)_1$ 1:1 superlattice is studied. In the low-temperature phase, a spontaneous polarization appears due to trilinear coupling of structural and antiferroelectric (ferrroelectric) modes. In chapter 6, results of first-principles calculations to investigate and analyze properties of (001) thin films made of the most complex perovskite system, namely $NaNbO_3$, are presented.

Ferroelectric, antiferroelectric and antiferrodistortive properties of this thin film are reported and discussed, as a function of misfit strain.

Acknowledgements

I am very grateful to my advisor, Professor Laurent Bellaiche. He led me to an exciting and promising research area, and motivated and encouraged me through this journey. I learned from him not only problem-solving skills in research but also diligent and attentive working ethics. He worked very hard to maintain a highly talented and friendly research group (CCMP group at the University of Arkansas) and showed genuine care for each member of the group. He is always a supportive and very understanding person. Without his advice, this dissertation would not be possible.

I would like to express my sincere appreciation to Dr. Sergey Prosandeev who is knowledgeable and provides me continued support, all necessary training needed to start and continue the research, and a plenty of help during my Ph.D. I appreciate Dr. Bin Xu who always supported me with Molecular Dynamics and phonon calculations. Apart from these studies, he is very supportive for any research problem.

I must also mention the help and contribution of all my collaborators, Sergey Prosendeev, University of Arkansas; Bin Xu, Soochow University; Jorge Iniquez, Luxembourg Institute of Science and Technology; Yurong Yang, Nanjing University; Changsong Xu, University of Arkansas. Their advice and feedback guided me through my research. A special thanks to Dr. Charles Paillard for helping me to understand the K-point parallelism for phonon calculation.

I would like to show my appreciation to all committee members of my dissertation, Professors Sergey Prosandeev, Hauxiang Fu, and Peter Pulay, for supporting my endeavors and taking the time to review this dissertation. I am also grateful to the faculty and staff of the Physics Department at the University of Arkansas, who always help me.

I am infinitely thankful to my husband and son, Yogeshbhai Patel and Taksh Patel. My husband

always encourages me in my work. He was the first one to suggest pursuing my doctorate. Both of them always support me no matter what the future holds. For this, I am forever grateful to them.

I am grateful to all my family in India and all my friends who always supported me with their love and prayers.

I am thankful to my spiritual guru, brahmaswarup shri Pramukh Swami Maharaj and pragat brahmaswarup Mahant Swami Maharaj for their constant blessing in my life.

Contents

List of tables

List of figures

Chapter 1

INTRODUCTION AND OUTLINE OF THE THESIS

1.1 Introduction

My dissertation is devoted to the study of static and dynamical properties of antiferroelectric (AFE) and improper ferroelectric (IFE) materials having the perovskite crystal structure. Several works based on density-functional calculations have devoted to study static properties of AFE and IFE [1–13], but their dynamical properties remain mostly unknown. In this chapter, important background information will be introduced, including perovskite structure, ferroelectricity, improper ferroelectricity, hybrid improper ferroelectricity, and antiferroelectricity.

Perovskite materials from an important class of functional materials. Oxides with a perovskite structure generally possess the ABO_3 formula. The simple ideal perovskite lattice is cubic, has 5 atoms per unit cell and adopts the space group $Pm\bar{3}m$ (221). The Russian mineralogist Lev Perovski discovered this crystal structure for the first time in the mineral $CaTiO_3$. A typical perovskite structure is shown in Fig.1.1. Most of the perovskite compounds adopts this cubic phase at high temperature and are thus paraelectric. When the temperature decreases, they undergo a structural phase transition with a different type of polar (electric dipoles are aligned parallel to each other) or anti-polar (electric dipoles are aligned opposite to each other) structure or even more complex structure.

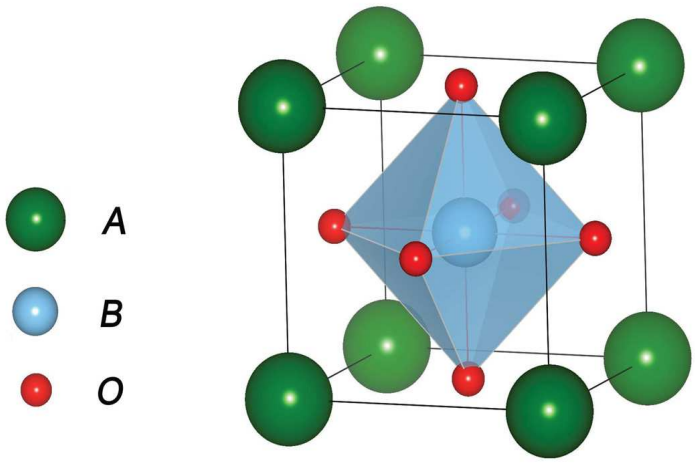

Figure 1.1: The structure of ABO_3 perovskite compounds

Perovskite materials played a critical role in the development of theory of ferroelectricity. Moreover, these materials have become most useful commercially due to their large polarization and good piezoelectric properties. The first ferroelectric perovskite discovered was Barium Titanate ($BaTiO_3$). This discovery was done by Wul and Goldman in 1945[14]. It has a paraelectric cubic perovskite structure ($Pm\bar{3}m$) at high temperature. However, as the temperature is lowered, there are successive phase transitions to three different ferroelectric phases, each involving small distortions from the cubic symmetry. The first phase transition at 393K is from paraelectric phase ($Pm\bar{3}m$) to tetragonal phase (P4mm). The tetragonal phase remains stable until 278K and then there is a second phase transition to orthorhombic ferroelectric phase (Amm2). At 183K, it again undergoes to a third phase transition which is ferroelectric having rhomboherdral symmetry (R3m). Each of these phase transitions (distortion from cubic symmetry) is due to the elongation of the cubic unit cell along [001] direction for the tetragonal phase, along [011] direction for the orthorhombic ferroelectric phase, and along [111] direction for the rhombohedral phase. The elongation of the cubic unit cell along these distortions results in a net displacement of the cation with respect to the oxygen octahedra. The displacements of ions (atoms) are along different directions for above

mentioned phase transition sequence, which results in dipole moment in different directions. The total dipole moments per unit volume is defined as polarization and is quantifies as follows:

$$P = \frac{\sum \mu}{V} \tag{1.1}$$

where μ is the dipole moment and V is the volume. Then, $BaTiO_3$ was subject to broad research that has given rise of our basic knowledge about ferroelectrics in general.

1.2 Perovskite structure components

Any distortion from the ideal perovskite structure typically consists of one of the following three components:

1. Displacements of the cation; when displacements are parallel to each other, it is identified as ferroelectric displacement (FE), and when antiparallel, it is identified as antiferroelectric displacement (AFE).

2. Distortion of the octahedra; Such distortion mechanism is due to the electronic instability of the octahedral metal ion. The Jahn-Teller distortion in $KCuF_3$ (Okazaki & Suemune, 1961) is an example of electronic instability leading to octahedral distortions.

3. Tilting of the anion octahedra; this distortion mechanism in octahedral tilting can be realized by tilting rigid BO_6 octahedra while maintaining their corner-sharing connectivity. Usually , this type of distortion is observed when the A cation is too small for the cubic BO_6 corner-sharing octahedral network.

The change in overall crystal symmetry when material undergoes a phase transition can depend on the how the octahedron is tilted. The most common distortion of the cubic Pm3m structure is octahedral tilting. There are numbers of ways in which the octahedral can be tilted. In 1972,

A.M. Glazer [15] gave rational explanation for octahedral tilting and created a notation to classify the different octahedral tilting patterns. This classification is only based on the octahedral tilting around each axis. It is as follows: when each successive octahedron of oxygen rotates in the same direction along one axis, it is known as in-phase tilting and is denoted by the "+" sign, while when each successive octahedron of oxygen rotates in opposite directions, it is know as out-of-plane tilting or anti-phase tilting and denoted by the "-" sign. When there is no rotation of the oxygen octahedral, it is denoted by the "0" symbol. The letters "a", "b", and "c" are used to represent the three possible directions of the rotations along x, y, or z axes, respectively. The Glazer notation for the in-phase and anti-phase tiltings of the oxygen octahedral around the z-axis are, for instance, $a^0a^0c^+$ and $a^0a^0c^-$, respectively.

The displacement of the cation and octahedron tilt are often coupled to each other. The tilting of the anion octahedra, if present in the perovskite structure, will help to identify the space-group symmetry of the structure. The soft mode is a collective excitation (as the collective excitations includes phonons which are the vibrations of the atoms in solid) whose frequency decreases enormously near a transition point. Such soft mode causes a lattice instability of the crystal, critically resulting in a structural phase transition, which can be of the first or second order.

1.3 Types of perovskite oxides

1.3.1 Ferroelectrics

Perovskite oxides form the most well known and most studied class of ferroelectrics. Ferroelectrics (FE) are materials that have a spontaneous polarization of two or more orientational states in the absence of an electric field and these states can be shifted from one to another by applying an electric field. Most of the ferroelectric materials exhibit a phase transition to a non-centrosymmetric phase

at some temperature when the material is cooled from high to low temperatures. The temperature at which the phase transition occurs is known as Curie temperature (T_c) and the non-symmetric phase is ferroelectric and exhibits hysteretic phenomena. At high temperature, the phase of ferroelectric materials has been called a "paraelectric" phase. This phase is centrosymmetric. When there are more than one ferroelectric phase, the temperature at which the crystal transitions from one ferroelectric phase to another is called the transition temperature. These are structural phase transitions, accompanied by structural changes and, most often, by symmetry. Dielectric, thermal, optical and elastic properties show anomalous behavior around the Curie temperature. The temperature dependence of the dielectric constant in ferroelectric crystals is usually determined by the Curie-Weiss law:

$$\varepsilon - \varepsilon_0 = \frac{C}{T - T_c} \quad for\ T > T_c \tag{1.2}$$

Where ε and ε_0 are the permittivity of the material and vacuum respectively, C is the Curie constant and T_c is the Curie temperature.

With increase in temperature, the dielectric constant increases and reaches a maximum value at T_c, with further increase in temperature the dielectric constant decreases following the Curie-Weiss law. The spontaneous polarization (P_s) for most of the ferroelectric crystals will be maximum at low temperature below T_c and at T_c it decreases to zero. If the spontaneous polarization disappears suddenly then the phase transition is classified as first order and if it decreases continuously at T_c then the phase transition is classified as second order as shown in figure 1.2.

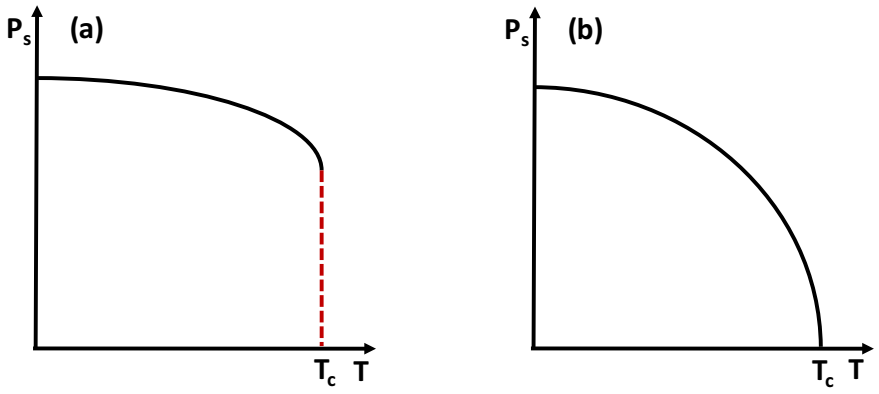

Figure 1.2: The spontaneous polarization as a function of temperature for (a) first order and (b) second order phase transition.

In 1937, the thermodynamical approach for the first and second order phase transitions was first given by Landau[16, 17]. Landau theory served as a theory of phenomenology with arguments based on symmetry for macroscopic entities. In 1949, Devonshire applied the Landau theory to $BaTiO_3$[18].

In Landau theory, the phase transition is explained in terms of order parameter contained in the thermodynamics potential[19, 20, 21, 22, 23, 24]. The order parameter associated in the phase transition determines the symmetry involved in the phase transition. Based on the order parameter, ferroelectric materials can be classified as proper, improper and hybrid ferroelectric materials according to the phenomenological description in terms of Landau theory. The proper, improper, and hybrid improper ferroelectrics are distinguished with respect to the order parameter.

1.3.2 Proper ferroelectrics

In proper ferroelectrics, the structure changes (phase transition) at the Curie temperature can be directly associated to the electric polarization P. Let us begin with the Landau theory in terms of single order parameter. The free energy of a proper ferroelectric system based on the Landau theory

is as follows:

$$f(T) = f_0(T) + \alpha(T - T_c)\mathcal{P}^2 + \frac{1}{4}\beta\mathcal{P}^4 + \frac{1}{6}\gamma\mathcal{P}^6 + O(\mathcal{P}^8) \tag{1.3}$$

where f_0 is the energy of the undistorted paraelectric phase and α, β, and γ are coefficients, $\mathcal{P}$ is the polar lattice distortion which is the primary order parameter and is directly proportional to the amplitude of the electric polarization in proper ferroelectrics. When $\alpha > 0$, $\beta < 0$, and $\gamma > 0$ the system undergoes a first-order phase transition i.e. the first derivative of free energy with respect to the primary order parameter at T_c is not continuous. When $\beta > 0$, the P^6 and higher order terms may be neglected, resulting in a transition to the second order phase i.e. the primary order at T_c is continuous. The free energy as a function of the order parameter $\mathcal{P}$ for $T < T_c$ and $T > T_c$ is shown in Figure 1.3. When the temperature (T) is above the Curie temperature (T_c), zero polarization minimizes the energy corresponding to paraelectricity. The Landau free energy has a dual-well shape when the temperature (T) is below T_c, which allows for finite non-zero polarization in the ground state which is one characteristic of proper ferroelectrics.

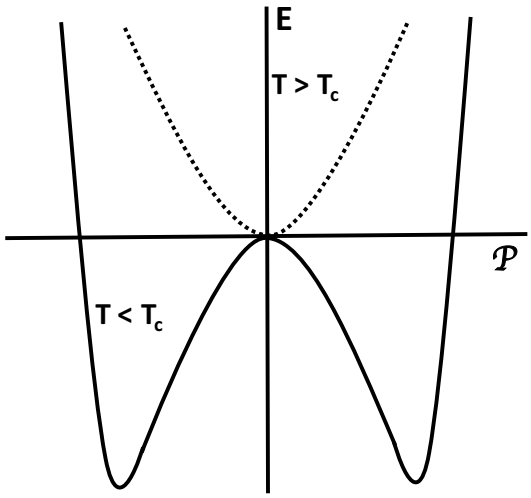

Figure 1.3: Energy behavior of polarization with the temperature (T), for T above and below the Curie temperature (Tc) of the primary order parameter for a proper ferroelectric transition.

1.3.3 Improper ferroelectrics

Unlike proper ferroelectrics where the polar lattice distortion is the major driving force for a transition, polarization is only part of a more complex lattice distortion in improper ferroelectrics or appears as a by-product of some other order parameter [25, 26]. The Landau free energy for improper ferroelectrics system is expressed as[26]:

$$f(T) = f_0(T) + \alpha\mathcal{P}^2 + \beta\mathcal{P}^4 + f(Q^2, Q^4) + \delta Q^n\mathcal{P} + O(\mathcal{P}^6) \tag{1.4}$$

where $\mathcal{P}$ indicates polar lattice distortion, Q is the primary distortion (i.e. the primary order parameter), and n is the exponent of the coupling and is termed as faintness index[27]. In order to minimize free energy, polarization appears below T_c only when Q is not zero, as shown in Figure 1.4. This means that the polar lattice distortion $\mathcal{P}$ is a by-product of the primary lattice distortion Q.

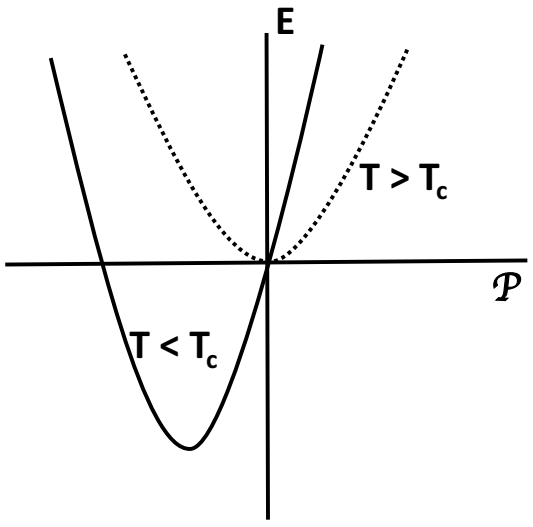

Figure 1.4: Energy behavior of the polarization with the temperature (T), for T above and below the Curie temperature (Tc) of the primary order parameter for a improper ferroelectric transition.

In the case of improper ferroelectrics $YMnO_3$[28, 29], n=3 in the Landau free energy equation

(4). The single unstable mode at q = ($\frac{1}{3}$, $\frac{1}{3}$, 0) which is composed of a rotation of the MnO_5 polyhedra and a buckling of the Y-O planes, is the primary distortion which is responsible for transition to the ferroelectric ground state. This primary distortion contributes to a tripling of the unit cell volume due to the coupling between $\mathcal{P}$ which is linear and Q (last second term in equation 4). Physically, the coupling term (odd in $\mathcal{P}$ and Q) means that the primary order parameter, in addition to polarization, changes direction when the electrical field is applied to an improper ferroelectric.

1.3.4 Hybrid improper ferroelectricity

Hybrid improper ferroelectrics (HIF) undergo a ferroelectric transition, i.e. transition to a polar structure, through a trilinear coupling contained in the free energy term [1]. The Landau free energy for hybrid improper ferroelectrics system is expressed as:

$$f(T) = f_0(T) + (T - T_c)a[Q_1^2 + Q_2^2] + \alpha\mathcal{P}^2 - \gamma Q_1 Q_2 \mathcal{P} + 4th\ order\ terms \tag{1.5}$$

Here temperature T_c is related to the primary order parameters Q_1 and Q_2 and a, α, and γ are coefficients, $\mathcal{P}$ is the polar distortion. The order parameters Q_1 and Q_2 are the two oxygen octahedral tiltings. More precisely, the ferroelectricity in HIF materials arises from a trilinear coupling of the form $\gamma\mathcal{P}Q_1Q_2$ between the ferroelectric mode $\mathcal{P}$ and two oxygen octahedral rotational mode (Q_1 and Q_2) [7]. In hybrid improper ferroelectric systems, the electric polarization is usually induced by the inversion symmetry breaking through $\bar{a}\bar{a}c^+$ (Glazer Notation [15]) octahedral rotation. In the Glazer Notation system, three components with superscripts imply rotations along three different Cartesian directions. The lower case letters represent the rotation amplitude, "+" implies in-phase and "-" implies out-of-phase rotation along a specific axis. In chapter 5, we will see in detail that the trilinear energetic couplings between two octahedral rotational mode with different symmetry

lead to the appearance of the spontaneous polarization, which is consistent with the existence of HIF in a superlattice.

1.3.5 Antiferroelectrics

Another class of materials known as antiferroelectrics (AFE) possesses zero polarization because adjacent dipoles are arranged in such a way that they cancel out each other. Like in ferroelectrics, the properties of antiferroelectrics also depend on temperature. Above a certain temperature, the antiferroelectricity vanishes and the systems are centrosymmetric. The temperature at which the antiferroelectricity disappears is known as the antiferroelectric Curie temperature [30]. Due to a variety of attractive functionalities offered by these materials, there is an increased interest in their use in technological applications which include high-density energy storage [12, 31, 32, 33, 34].

The energy storage application in antiferroelectric materials comes from the double hysteresis loop shown in Figure (1.5).

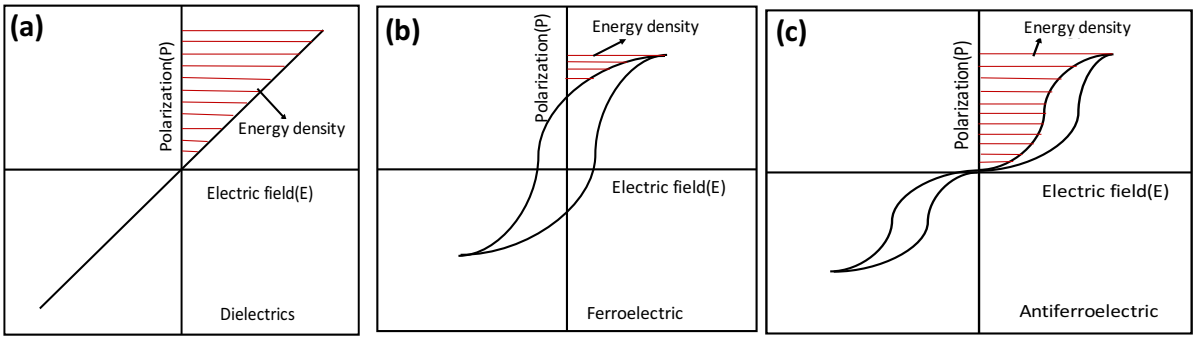

Figure 1.5: Relationship between polarization and electricity in the (a) dielectric, (b) ferroelectric, and (c) antiferroelectric materials and the electric energy density in these materials under electric field. The dashed area is proportional to this energy.

More precisely, Figure (1.5) shows the polarization - electric field (P-E) loop for typical dielectric, ferroelectric, and antiferroelectric materials. The shaded areas enclosed by the polarization

and electric field represent the discharging energy. As seen from Figure (1.5), for the ferroelectric materials, the shaded area is small, compared to the dielectric and antiferroelectric materials. So, the antiferroelectric materials have superior discharging ability. This can be seen from as the area enclosed under the P-E loop for antiferroelectrics.

1.4 Materials studied

I studied different complex antiferroelectric materials to reveal and investigate the effect of the bilinear and trilinear energetic coupling between the antiferroelectric displacement of the cation and two oxygen octahedral tiltings. In particular, the *bilinear coupling* explains the improper (due to softening of the rotational degrees of freedom) emergence, at some conditions, of soft antipolar phonons characterizing prototypical antiferroelectric $PbZrO_3$. It also provides us with a unified description of the complex antipolar structures of a variety of perovskites, including possible occurrence of incommensurate phases. The *trilinear coupling* involving in-phase and anti-phase oxygen octahedral tilting along with the antiferroelectric displacement helps us to understands the dynamics of $BiFeO_3$ under hydrostatic pressure. Trilinear energetic couplings can also give rise to the formation of electrical polarization in the so-called hybrid improper ferroelectrics (HIF) which can be realized by creating superlattices (SLs) made of two perovskite compounds, each adopting the Pnma space group. Here we study the effect of finite temperature-dependence of dynamical properties of ($BiFeO_3$)/($NdFeO_3$) 1:1 superlattice. Since the physical properties of epitaxial thin films substantially differ from those in bulk and layered materials, the compressive or tensile stress may change the phase-transition sequence in thin films with respect to the bulk material and, apart from a shift in the temperature of the ferroelectric transition, changes the entire phase diagram, creating new phases that are not present in bulk crystals. We thus also studied here the phase

transitions of the antiferroelectric $NaNbO_3$ system under epitaxial strain.

1.4.1 Lead Zirconate

The first AFE material discovered is lead zirconate $PbZrO_3$ (PZO), and the ground state is having Pbam symmetry below ~505K [35, 36, 37]. There are two strongly stable soft phonon modes in the PZO ground state with Pbam symmetry [38, 39, 40, 41, 42, 43]. The first mode is called as R_4^+ by its symmetry and is associated with the zone boundary $\frac{2\pi}{a_{lat}}(\frac{1}{2}, \frac{1}{2}, \frac{1}{2})$ k-point of the cubic Brillouin zone, where a_{lat} is the lattice constant of the five-atom cubic perovskite cell. This mode is typically an anti-phase tilting of the oxygen octahedral in the perovskite lattice. The second mode is known as Σ_2 mode and is associated with the $\frac{2\pi}{a_{lat}}(\frac{1}{4}, \frac{1}{4}, 0)$ k-point. The Σ_2 mode consists of the lead ion antipolar displacement (antipolar displacement) and oxygen displacement. There is also a third soft mode which is very weak with S_4 symmetry and this mode is associated with the $\frac{2\pi}{a_{lat}}(\frac{1}{4}, \frac{1}{4}, \frac{1}{2})$ k-point [30]. Some recent works [38, 39, 40] suggested that the trilinear coupling between R_4^+, Σ_2, and weaker S_4 modes plays an important role to stabilize the Pbam ground state of PZO. However, this trilinear energy only amounts to 27 meV per formula unit (f.u.) out of the 392 meV/fu gain of the ground state with respect to the cubic paraelectric phase, according to first-principles calculations[38], and does not explain why the unusual Σ_2 and S_4 modes are strongly unstable by themselves in PZO. One may, therefore, wonder if another energy plays a crucial role in PZO, and what is the analytical form of such energy in terms of elemental interatomic couplings (if any). One can also ask if such hypothetical energy can further describe other complex antipolar states, that many materials are known to exhibit, and may also be of relevance to the formation of incommensurate phases in perovskites. In chapter 3, we report the discovery of a novel atomistic energy (analytically derived) that bi-linearly couples the A-cation displacements

and oxygen octahedral tilting in ABO_3 perovskites and which provides an unified description of many antiferroelectric and incommensurate perovskites. In particular, this new coupling explains the improper (due to softening of the rotational degrees of freedom) emergence, at some conditions, of soft antipolar phonons characterizing prototypical antiferroelectric $PbZrO_3$. It also provides us with a unified description of the complex antipolar structures of a variety of perovskites, including possible occurrence of incommensurate phases. The results of this study have been published in Ref. [44].

1.4.2 Bismuth ferrite.

$BiFeO_3$ (BFO) is the most studied perovskite oxide because of it special properties and potential applications. The bulk BFO crystal has a rhombohedral ground state with R3c phase and it remains stable till ferroelectric transition temperature T_C=1100 K. BFO is known to adopt Pnma symmetry at high pressure [45, 46, 47]. The Pnma structure consists of two oxygen octahedral tilting patterns $a^-a^-c^0$ and $a^0a^0c^+$. The tilt $a^-a^-c^0$ pattern corresponds to R_4^+ phonon mode while the tilt $a^0a^0c^+$ pattern corresponds to M_3^+ phonon mode. Along with these modes, the Pnma symmetry is also stabilized by the antiferroelectric displacement of cation in BFO. Here these two oxygen octahedral tiltings are coupled with the antiferroelectric displacement of the Bi cation and this coupling is known as a trilinear energetic coupling. Interestingly, several works on trilinear energetic couplings have been done to understand the static properties but the effect of trilinear coupling on dynamics have not been studied so far.

In chapter 4, we report the results of the study of the dynamics of antiferroelectric distortion $BiFeO_3$ bulk under hydrostatic pressure using atomistic simulations. Under high hydrostatic pressure, BFO is antiferroelectric. The problem we wanted to resolve is if BFO has an antiferroelectric

soft mode. This is a fundamental problem. Actually, we found that the antiferroelectric mode does not soften itself on cooling, but rather the phase transition is improper, due to coupling of this mode to two other soft structural (tilting) modes. The following phase transition sequence is found on cooling from high temperature: the cubic paraelectric Pm3m state at high temperature and is followed by an intermediate phase possessing long-range-ordered in-phase oxygen octahedral tilting, and then the Pnma phase. The Pnma phase is known to possess antipolar cation displacements in addition to in-phase and antiphase oxygen octahedral tilting. In the paraelectric phase, the antipolar cation modes are found to have high phonon frequencies that are independent of temperature. On the other hand, some phonons possessing oxygen octahedral behavior are rather soft in the intermediate phase and Pnma states. Analysis of the data combined with an analytical model reveals that such features originate from a dynamical mixing between pure antipolar cation phonons and fluctuations of oxygen octahedral tilting, as a result of a specific trilinear energy coupling involving in-phase and anti-phase oxygen octahedral tilting. The model developed can be easily applied to predict the dynamics of antipolar cation motions for other possible structural paths bridging Pm3m and Pnma states. The results of this study have been published in Ref. [48].

1.4.3 Layered perovskites: ($BiFeO_3$)/($NdFeO_3$) 1:1 superlattice.

Superlattice is a periodic structure of layers of two or more materials. In fact, HIF systems can be realized by creating superlattices (SLs) made of two perovskite compounds, where each compound adopts the Pnma symmetry, which possesses in-phase and antiphase oxygen octahedral tiltings as well as antipolar motions. It is understood that, in such HIF stacking, ferroelectricity originates from a trilinear coupling between polarization and these two octahedral tilting modes of oxygen. Several works based on density-functional calculations have been done to understand and characterize HIF

materials [1, 2, 4, 5, 49] and an atomistic theory has even been proposed to further understand them [7, 8]. Interestingly, all of these works have focused on static HIF properties , especially at 0 K. Finite-temperature dynamic properties of HIFs therefore remain mostly unexplored.

Chapter 5 reports results of our study of polar, antipolar, and antiferrodistortive phonons at finite temperatures in a hybrid improper ferroelectric (HIF). The prototypical HIF ($BiFeO_3$)/($NdFeO_3$) [abbreviated as $(BFO)_1/(NFO)_1$] 1:1 superlattice is studied using an atomistic effective Hamiltonian approach along with a developed analytical model. This system possesses a tetragonal paraelectric P4/mmm state at high temperatures and polar $Pmc2_1$ phase at low temperature. The later phase has hybrid improper ferroelectricity (HIF) character. In the high-temperature paraelectric phase, the polar and antipolar phonons modes exist due to a bilinear coupling between different cations displacements. The frequencies of these phonons (both polar and antipolar) are nearly independent of temperature in the paraelectric phase. At the same time, in the same phase, the in-phase and and anti-phase tiltings of the oxygen octahedron are soft in this high-temperature phase. Below some critical temperature, these tilting modes condense and result in the emergence of the low-temperature phase. On the other hand, the polar and antipolar modes abruptly condense at this temperature too in the low-temperature $Pmc2_1$ phase near the ferroelectric-to-paraelectric transition. As we will show, this happens because of very specific trilinear energetic couplings between polar and antipolar distortions with the soft oxygen octahedral tilting modes. Such mixing increases the number of peaks of polar and antipolar phonons in the corresponding correlators, which we have calculated. And each possesses not only polar and antipolar but also antiferrodistortive characters in the dielectric responses corresponding to these modes when passing through the phase transition from the P4/mmm to $Pmc2_1$ phase. The different temperature behaviors of polar modes at high versus low temperatures emphasize the uniqueness of hybrid improper ferroelectrics. The results

of this study have been published in Ref. [50].

1.4.4 $NaNbO_3$ thin film.

It is found that the ferroelectric properties of thin films typically differ from those of the bulk materials and provide a route for property tuning. Many factors contribute to these differences. The perovskite thin film properties have been strongly influenced by the magnitude of the epitaxial strain. The strain due to lattice mis-matching of the film to the substrate is known as epitaxial strain or misfit strain. In thin films, due to the misfit strain, one can control the piezoelectric and ferroelectric properties. Experimental study by Haeni et. al [51] used epitaxial strain to have a ferroelectric phase at room temperature in normally-paraelectric $SrTiO_3$. The use of biaxial compressive strain was also stated by Cheo et. al [52] to greatly improve the ferroelectric properties of $BaTiO_3$. At present, $NaNbO_3$ (NNO) bulks is known to have seven phase transitions sequence at different temperatures: U (Cubic Pm3m) $\rightarrow$ 913K$\rightarrow$ T2 phase (Tetragonal P4/mbm) $\rightarrow$ 848K $\rightarrow$ T1 phase (Orthorhombic Cmcm) $\rightarrow$ 793K $\rightarrow$ S phase (Orthorhombic Pmmm) $\rightarrow$ 753K $\rightarrow$ R phase (Orthorhombic Pmmn) $\rightarrow$ 633K $\rightarrow$ P phase (Orthorhombic Pbcm) $\rightarrow$ 173K $\rightarrow$ N phase (Rhombohedral R3c). In some NNO samples an additional room temperature Q phase of $Pmc2_1$ symmetry coexists with the P phase [53, 54, 55]. The Q phase was not found in ceramics [54, 56], powders [56], and some crystals [54] as this phase is triggered by a small electric field. The temperature-*versus*-strain phase diagram of NNO films is not known to the best of our knowledge. In this work, I will study the influence of epitaxial strain on ferroelectric, antiferroelectric or antiferrodistortive properties within a given phase as a function of strain on NNO film using density functional theory. Our results will help to understand the phase transitions sequence with the change in the misfit strain.

1.5 Structure of this dissertation is as follows

This dissertation has six other parts in addition to the introduction :

(1) Effective Hamiltonian Method and First-Principles Methods (Chapter 2),

(2) Atomistic mechanism leading to complex antiferroelectric and incommensurate phases (Chapter 3),

(3) Dynamics of antipolar distortions of $BiFeO_3$ (Chapter 4),

(4) Temperature dependence of polar modes in hybrid improper ferroelectrics for $(BiFeO_3)/(NdFeO_3)$ 1:1 superlattice (Chapter 5),

(5) Properties of (001) $NaNbO_3$ films under epitaxial strain: A first-principles study (Chapter 6),

(6) Conclusion (Chapter 7).

Chapter 2

BACKGROUND

2.1 Introduction

To investigate the properties of materials, it is important to fully understand the methodology and techniques employed for theoretical and experimental studies of these properties. In this dissertation I use the computational methods described below.

The computational methods can be divided into two main categories: (1) classical and (2) quantum mechanical approaches. The key difference between these two methods is whether the algorithm used is based on classical or quantum mechanical laws. The effective Hamiltonian method applied in the present work is based on first-principles approaches and can handle large systems as well as finite-temperature calculations. Density Functional Theory (DFT) is a quantum mechanical approach. The DFT method solves time-independent Scrödinger equation for multi-body systems. The Effective Hamiltonian Method can be implemented on the basis of whether Monte Carlo (MC) or Molecular Dynamics (MD) algorithms. MC approach is based on random walk algorithm, whereas MD approach employs Newtonian-type dynamical equations applied to all degrees of freedom of the selected Hamiltonian and are based on the classical theories of Newtonian and statistical mechanics.

2.1.1 Density Functional Theory

DFT is a computational quantum mechanical method used for determining the ground state (0 Kelvin) properties of atoms, molecules, and condensed phases of matter. This method determines properties of multi-electron systems by the use of a Kohn-Sham functional of the electron density n(r) [59]. Specific form of this functional has now several approximations. Below, I will give more

details about DFT.

2.1.2 Schrödinger Equation

Many-body Schrödinger equation can be written as:

$$\hat{H}\Psi = E\Psi \tag{2.1}$$

where $\hat{H}$ is the Hamiltonian operator; Ψ and $\mathbf{E}$ are the many-body wave function and energy of the system. Hamiltonian $\hat{H}$ depends on the electronic and nuclear coordinates and on spin variables. The so-called Born-Oppenheimer (BO) approximation is used to separate the nuclear and electronics degrees of freedom when the electronic mass is much smaller than that of the nuclei. One has to consider the nuclei at rest when considering electronic degrees of freedom. Then the electronic Hamiltonian is written in the following form:

$$\hat{H}_e = \hat{T}_e + \hat{V}_{ee} + \hat{V}_{en} \tag{2.2}$$

where $\hat{H}_e$ is the Hamiltonian of the electrons, $\hat{T}_e$ is the kinetic energy of the electrons, $\hat{V}_{en}$ is the external potential that electrons feel due to the nuclei, and $\hat{V}_{ee}$ is the electron-electron interaction energy. These three operators are defined as follows:

$$\hat{T}_e = -\frac{1}{2}\sum_{n}^{N_E}\nabla^2 \tag{2.3}$$

$$\hat{V}_{ee} = \frac{1}{2}\sum_{n<m}\frac{1}{|r_n - r_m|} \tag{2.4}$$

$$\hat{V}_{en} = \sum_{n=1}^{N_E}\sum_{i=1}^{N_N}\frac{Z_i}{|r_n - R_i|} \tag{2.5}$$

where N_E and N_N are the numbers of the electrons and nuclei, r_n is the position of the n^{th} electron and R_i and Z_i are the position and charge of the i^{th} nucleus, respectively, and ∇^2 is the Laplacian

operator. Solving equation (2) is highly difficult due to two reasons: (1) operators are represented by a 3N × 3N matrix, where N ~ 10^{23} for materials, (ii) the ground state wave function cannot be broken into individual electron's wave functions due to the electron electron interaction energy. The solution to this problem was provided by Hohenberg and Kohn [60]. The Hohenberg-Kohn theorems are the foundation of DFT. I will review these theorems below. By using DFT, one can use electron density n(**r**) as a basis which reduces the number of variables from 3N to 3 variables.

2.1.3 Hohenberg-Kohn theorem

The Hohenberg-Kohn (HK) theorems state that:

Theorem I: the ground state property of the system can be determined in terms of the ground state electron density $n_0(\mathbf{r})$ by considering $n_0(\mathbf{r})$ as basic variable. The external potential $\hat{V}_{en}$ is written as a functional of $n_0(\mathbf{r})$ [61]. It proves one-to-one mapping between the external potential and the ground state densities in many electron systems.

Theorem II: It is possible to describe the energy functional E[n] in such a way that minimizing E[n] with respect to variations of n(**r**) gives the ground state density $n_0(\mathbf{r})$. This energy functional can be written as

$$E[n] = F[n(\mathbf{r})] + \int \hat{V}_{en} \cdot n(\mathbf{r}) dr \tag{2.6}$$

where F[n(**r**)] is the universal functional of the ground-state electronic density. The universal functional contains the individual contributions of kinetic energy, classical Coulomb interaction, and the non-classical self-interaction correction.

2.1.4 The Kohn-Sham theorem

In 1965, Kohn and Sham proved that the many-body Schrödinger wave function is separable into a product of individual electronic wave functions [62]. The Kohn-Sham (KS) theory suggests that there exists a set of wave-functions which corresponds to the ground-state density of interacting electrons,

$$n_0(\mathbf{r}) = \sum_{i=1}^{N} |\psi_i(\mathbf{r})|^2 \tag{2.7}$$

The total KS wave function is not equal to the true wave function of the Hamiltonian. The KS system is auxiliary to the true system, but can describe the ground state properties because of the first HK theorem. The loss of the true wave functions is compensated for benefit of a simplified type of HK-energy functionality. One can rewrite the energy functional using the KS approach as:

$$E[n] = T_{KE}[n] + E_{Hartree}[n] + \int \hat{V}_{en} n(\mathbf{r}) dr + E_{XC}[n] \tag{2.8}$$

where $E_{Hartree}[n]$ is the classical Hartree energy, $E_{XC}[n]$ is the exchange-correlation energy, and $T_{KE}[n]$ is the total kinetic energy of the non-interacting auxiliary system and is defined as follows:

$$T_{KE}[n] = \frac{1}{2} \sum_{i} |\nabla \psi_i(\mathbf{r})|^2 \tag{2.9}$$

The classical Hartree energy is as follows:

$$E_{Hartree}[n] = \frac{1}{2} \int \frac{n(\mathbf{r}) n(\mathbf{r}')}{\mathbf{r} - \mathbf{r}'} dr \tag{2.10}$$

If an $E_{XC}[n]$ is known explicitly then $E[n]$ can be minimized and one can determine the full many body Hamitonian's ground state density, and hence all ground state properties.

The goal is to obtain the ground state electron density, $n_0(\mathbf{r})$, which minimizes the KS energy

functional given in Equation (8). In practice, a self-consistency loop strategy is used. The self-consistent minimization method is as follows: write Equation (8) in a simple form by setting the functional derivative of $E[n]$ with respect to the KS wave functions to vanish,

$$(-\frac{1}{2}\nabla^2 + V_{en} + \frac{\delta E_{Hartree}}{\delta n} + \frac{\delta E_{XC}}{\delta n} - \epsilon_i)\psi_i = 0 \tag{2.11}$$

Here, Hartree potential is defined as:

$$\frac{\delta E_{Hartree}}{\delta n} = \int \frac{n(\mathbf{r}')}{|\mathbf{r} - \mathbf{r}'|} \tag{2.12}$$

ψ_i is the KS eigenfunctions and ϵ_i are their's eigenvalues. Equation (11) is a nonlinear Schrödinger equation. These nonlinear equations are solved by the following steps:

(1) provide an initial guess for the electron density $n(\mathbf{r})$

(2) compute $\frac{\delta E_{Hartree}}{\delta n}$ and $\frac{\delta E_{XC}}{\delta n}$

(3) solve Equation (11) for KS wave function and eigenvalues

(4) use the result of step (3) to obtain the new ground state density

(5) compare initial $n(\mathbf{r})$ and $n(\mathbf{r})_{new}$, if $n(\mathbf{r})$=$n(\mathbf{r})_{new}$, then calculate the total ground state energy $E[n]$. Normally we have some deviation which is smaller a given number.

(6) otherwise set $n(\mathbf{r})_{new}$ as an input for $n(\mathbf{r})$ and repeat steps (2) through (5).

2.1.5 Local Density Approximation and Generalized Gradient Approximation

The exact form of the exchange-correlation energy ($E_{XC}[n]$) is not known and therefore its functional derivatives are unknown. Approximate versions of this interface are used in realistic calculations. The exchange-correlation energy is a linear combination of exchange and correlation energy terms

and is given as follows:

$$E_{XC} = E_X + E_C \tag{2.13}$$

Local Density Approximation (LDA) assumes that the exchange-correlation energy per electron at point r in the electron gas is simply what it would be in a homogeneous electron gas of the same density at r [63].

$$E_{XC}^{LDA}[n] = \int n(\mathbf{r})\epsilon_{XC}^{LDA} d\mathbf{r} \tag{2.14}$$

where ϵ_{XC}^{LDA} is the exchange-correlation energy of a homogeneous electron gas per electron.

Another method uses gradient of electron density along with the local density at that point in order to include more physical information. This method is termed the generalized gradient approximation (GGA).

$$E_{XC}^{GGA}[n] = \int n(\mathbf{r})\epsilon_{XC}^{GGA}(n(\mathbf{r}), \nabla n(\mathbf{r}))d\mathbf{r} \tag{2.15}$$

The most commonly used Generalized Gradient Approximation (GGA) functionals, include Becke's 1988 exchange functional combined with the correlation functional of Lee, Yang, and Parr (BLYP) [64, 65] and Perdew–Burke-Ernzerhof (PBE) [66, 67]. PBE functional belongs to the GGA functional for exchange correlation energy while BLYP approach belongs to the hybrid approximation for the exchange-hybrid correlation functional.

2.1.6 Pseudopotential Method

One can obtain numerical solutions of the KS equations by expanding the KS orbitals with respect to the appropriate basis sets. KS orbitals that satisfy the Bloch theorem can be expanded in plane waves. The Bloch theorem states that the wave function in a crystal can be expressed as a product

of the plane wave and a lattice periodic function:

$$\psi_{\vec{k}}(\vec{r}) = e^{i\vec{k}r} u_{\vec{k}}(\vec{r}) \tag{2.16}$$

where $\psi_{\vec{k}}$ is the bloch wave, $u_{\vec{k}}(\vec{r})$=$u_{\vec{k}}(\vec{r} + a)$ is the lattice periodic function, and $e^{i\vec{k}r}$ is the plane wave. According to the Bloch theorem, the KS orbitals, i.e. single body wave function $\Psi_{n,k}$, can be expanded in the plane wave basis [68].

$$\Psi_n = \sum_G C_n(k, \vec{G}) e^{i(\vec{G}+\vec{k}).\vec{r}} \tag{2.17}$$

where k is a k-vector in the first Brillouin zone of the unit cell or supercell used in the calculation, n is a band index, G is the reciprocal lattice vector, and $C_{n,\vec{G}}$ is a coefficient. Here the summation over $\vec{G}$ is truncated at $G = G_{cut}$, where G_{cut} is the largest value satisfying the following condition: $\frac{1}{2}|\mathbf{k} + \mathbf{G}|^2 < E_{cut}$. E_{cut} is the cut-off energy. The KS orbitals expansion using plane waves can give slow convergence if the core electrons are included in the basis set because $\Psi_n(r)$ is rapidly varying near atomic nuclei. To overcome this slow convergence, it is often smart to use a pseudo potential in combination with the plane waves. Below, I will describe the main pseudo-potentials in use now.

Different types of pseudo-potentials have been developed. The effect of core electrons on the properties of solids is ignored in pseudo-potential theory as the core electrons are chemically inert and independent of the chemical environment surrounding them. Pseudopotential approximation substitutes the ionic ion potential with a hypothetical potential. This approximation helps to obtain a much smoother potential as valence electrons are screened by the core electrons.

The work reported in Chapter (5) uses Perdew-Burke-Ernzerhof-PBEsol (PS) functional. These functional are intended for the solid state and surface systems. They are based on a gradient

expansion of the exchange energy. The technical details of PBEsol are given in references [66, 67]. The PBEsol functional [69] is a modified version of PBE [66]. The PBEsol lattice constants are more accurate and lower than PBE by about 1%-2%, but the drawback with PBEsol is that it is less accurate for cohesive energies than PBE [70, 71, 72, 73, 74].

2.2 Structural and electronic properties

DFT allows calculations of different physical quantities. In this section, we will see how DFT helps us to calculate the polarization.

Structural phase transition from a reference to distorted structure can be determined by identifying unstable phonon modes in the reference structure. The phonon modes can be obtained in the harmonic approximation. Within the theory of lattice dynamics, a crystal's potential energy is a function of the atomic positions. The potential energy of a crystal can be expanded in by Taylor's series with respect to the atomic displacements:

$$\Phi = \Phi_0 + \sum_{i\alpha} \Phi_{i\alpha} u_{i\alpha} + \sum_{i\alpha,j\beta} \Phi_{i\alpha,j\beta} u_{j\beta} + ... \tag{2.18}$$

Here, Φ_0 is the potential energy at equilibrium (when all atoms are at equilibrium positions), $u_{i\alpha}$ is the displacement of the ith atom in α direction. The coefficients $\Phi_{i\alpha}$, $\Phi_{i\alpha,j\beta}$, ...etc are derivatives of the potential energy with respect to the atomic displacements. At equilibrium, the first order derivative of the $\Phi_{i\alpha}$ is zero with respect to displacements, as the forces on all atoms at equilibrium are zeros. The second derivatives $\Phi_{i\alpha,j\beta}$ is a symmetric matrix and is called Hessian matrix. When the eigenvalues of the Hessian matrix are positive or zero indicating that the system has stable minimum it constitute the force constant matrix. The phonon modes are determined from this

force-constant matrix as follows:

$$\Phi_{i\alpha,j\beta} = \frac{\partial^2 E}{\partial u_{i\alpha} \partial u_{j\beta}} \tag{2.19}$$

Within harmonic approximation, the equations of motion for the lattice ions can be obtained as follows:

$$F_\alpha = m_i \ddot{u}_{i\alpha} = -\sum_{i\alpha,j\beta} \Phi_{i\alpha,j\beta} u_{j\beta} \tag{2.20}$$

We look for the solutions in a form of the following product:

$$u_\alpha = \frac{1}{\sqrt{m_i}} e_\alpha exp[i(\vec{q} \cdot \vec{x} - \omega t)] \tag{2.21}$$

where m_i is the mass of the ith atom, e_α are the eigenvectors which determines the relative motion of the ith atom in a phonon at wave vector $\vec{q}$, and ω is the frequency. Plugging Eqn. (2.21) into Eqn. (2.20), one gets

$$\omega^2 e_\alpha(\vec{q};\alpha) = \sum_{i\alpha,j\beta} D_{i\alpha,j\beta} e_\beta(\vec{q};j\beta) \tag{2.22}$$

Here,

$$D_{i\alpha,j\beta} = \frac{1}{\sqrt{m_i m_j}} \sum_{j\beta} \Phi_{i\alpha,j\beta} exp[-i\vec{q} \cdot \vec{x}j] \tag{2.23}$$

$D_{i\alpha,j\beta}$ is known as dynamical matrix and, by diagonalizing equation (2.23), one will obtain eigenvectors and eigenvalues. The eigenvalues of the above equation are the phonon mode frequencies. If the mode frequency is real then the mode is stable with respect to the atomic displacements while if the mode's frequency is imaginary, the mode is unstable and, as a result, a symmetry breaking and a low-symmetry distorted structure will stabilize the phonons. For the distorted structure, the

atomic charges are the Born dynamical charges. The Born effective charge matrix is defined as:

$$Z_{i,\alpha\beta} = \frac{\Omega}{e}\frac{\partial P_\alpha}{\partial u_{i\beta}} \tag{2.24}$$

where Ω is the volume of the unit cell, P_α is the polarization in α direction, e is the electric charge

The total polarization of the material is a combination of the ionic polarization P_{ion} and electronic polarization P_{ele} contribution [75]:

$$P = P_{ion} + P_{ele} \tag{2.25}$$

The ionic part of polarization is defined as:

$$P_{ion} = \frac{e}{\Omega}\sum_i Z_i^{ion} r_i \tag{2.26}$$

where eZ_i^{ion} is the positive point charge located at the atomic position r_i. The electronic part of the polarization is obtained as [75]:

$$P_{ele} = \frac{2|e|i}{(2\pi)^3}\int_A dk_\perp \sum_{n=1}^{M}\int_0^{G\|}\left\langle u_{k,n}|\frac{\partial}{\partial k_\|}|u_{k,n}\right\rangle dk_\| \tag{2.27}$$

where the sum runs over the occupied bands, the $k_\|$ wave vectors are parallel to the direction of polarization, and $G_\|$ is a reciprocal lattice vector in the same direction. The states $|u_{k,n}\rangle$ are the cell periodic parts of the Bloch functions. The last integral is known as the Berry phase.

In Chapter 5, I report a study of the effect of epitaxial strain on a thin film in terms of phase diagram and polarization. Let us now understand the concept of epitaxial strain. The epitaxial strain plays an important role in the determination of the ferroelectric properties of thin films and superlattices. The epitaxial strain can be realized by lattice mismatch between the sample and substrate. If the in-plane cell dimensions are fixed to match that of substrate while the out-of-plane

dimensions are allowed to relax, then an epitaxial growth occurs.

In the first principles calculations, the epitaxial strain is determined by imposing that in-plane lattice vectors are fixed while out-of-plane lattice vectors are allowed to relax. Experimental and theoretical studies have shown that epitaxial strain plays an important role in stabilization of the ferroelectricity in thin films [76]. The effect of epitaxial strain on NNO film will be the subject of Chapter 5.

2.3 Effective Hamiltonian Method

The study of ferroelectrics and associated perovskite oxides has been a subject of a variety of atomic-scale theoretical and numerical studies for at least twenty seven years [77, 78]. Ab initio simulations have been well developed and employed to get values of parameters of microscopic models used to explain and forecast thermodynamics of phase transitions in perovskite oxides, which can be very complicated [77, 78].

In 1994, Zhong, Vanderbilt and Rabe suggested a new paradigm how to perform calculations of temperature-dependent properties of ferroelectrics by using MC or MD methods. This method was named the Effective Hamiltonian is viewed in terms of the potential energy surface containing specific degrees of freedom, such as local modes, the inhomogeneous strain tensor, and the homogenous strain tensor. The Effective Hamiltonian parameters are determined from first principles DFT calculations. Once we have these parameters, one can perform MC or MD simulations to predict various physical quantities which are obtained as statistical averages at given condition (temperature, pressure, or stress tensor).

We use this Effective Hamiltonian approach in MD simulation to study the dynamics of $BiFeO_3$ under pressure (Chapter 4) and $(BiFeO_3)_1/(NdFeO_3)_1$ 1:1 superlattice (Chapter 5).

2.3.1 Theoretical Background of the Effective Hamiltonian

The Effective Hamiltonian, H_{eff}, approach used here serves the following advantages: (1) It offers a broad picture from microscopic views of the properties of investigated ferroelectric systems by the decomposition of the energetic contributions of such Hamiltonian; (2) It models finite-temperature-dependent static or dynamic properties of ferroelectric systems by combining this efficient Hamiltonian with Monte Carlo algorithms or molecular dynamics simulations; (3) It is able to simulate large supercells by significantly decreasing the degrees of freedom, which is very important in the analysis of complex systems and complicated phenomena. This makes it feasible to study the finite-temperature properties of large complex perovskite systems. In the case of perovskite ABO_3 compounds, the highest symmetry is obtained by centering the local mode either on A or B atoms. If a lattice contains n atoms per basis, there will be 3n phonon modes for each reciprocal k-point: three acoustic and 3(n-1) optical phonon modes. But only the lowest transverse optical (TO) mode-soft phonon and the strain variables (long-wavelength acoustic phonons) contribute to the low energy distortion structure. In the case of perovskite with 5 atoms per primitive unit cell, there are 15 normal-modes, (3 acoustics and 12 optical) per k-point [79]. The main idea of the Effective Hamiltonian method is to reduce the number of the degrees of freedom.

Degrees of Freedom

The Effective Hamiltonian method reduces the number of the degrees of freedom to:

(i) the local mode $\mathbf{u_i}$, which is a polar displacement of the atoms in the i^{th} unit cell. This polar displacement induces electric dipole in each unit cell.

(ii) the inhomogenous displacement mode, which describes the local inhomogeneous strain in unit

cell i and is associated with long-wavelength acoustic modes. One can find inhomogenous ($\eta_l^I(i)$) strain tensor from this displacement.

(iii) the homogeneous strain tensor η_l^H is a six-component local strain tensor in Voigt notation

The total strain in unit cell is defined as $\eta_l(i) = \eta_l^H + \eta_l^I(i)$, here η_l^H is the homogeneous strain tensor and η_l^I is the inhomogeneous strain tensor.

(iv) the pseudo-vector ω_i, which is centered on B ions and characterizes oxygen octahedral tiltings [80] (also known as antiferrodistortive (AFD) distortions) in unit cell i. For instance, $\omega_i = 0.1\mathbf{z}$, where $\mathbf{z}$ is the unit vector along the z-axis, indicates that the oxygen octahedron centered around the B site i tilts by 0.1 radians about the z-axis.

(v) the magnetic dipole moment m_i. In case of $BiFeO_3$, it will be Fe-centered and its magnitude is equal to 4μB, as consistent with first principles [81] and measurements [82].

Effective Hamiltonian

Considering only local modes and strain, the Effective Hamiltonian consists of five parts: a local mode self energy, a long range dipole-dipole interaction, a short-range interaction between soft modes, an elastic energy, and an interaction between the local modes and local strain [78]. The total energy of the Effective Hamiltonian is as follows:

$$E_{tot} = E^{self} + E^{dipole} + E^{short} + E^{elastic} + E^{int} \tag{2.28}$$

(1) Local Mode Self Energy:

This is the first contribution to the Effective Hamiltonian energy associated with the local modes in the unit cell. The local self energy terms is defines as:

$$E^{self} = \sum_i (\kappa_2 u_i^2 + \alpha u_i^4 + \gamma(u_{ix}^2 u_{iy}^2 + u_{ix}^2 u_{iz}^2 + u_{iy}^2 u_{iz}^2)) \tag{2.29}$$

where i is the unit cell index, u_i is the local soft-mode amplitude vector in the unit cell i, κ, α, and γ are coefficients that are determined from first principles methods. In order to describe the ferroelectric (FE) process, E^{self} must contain both anharmonic and harmonic contributions. Here only terms containing even powers survives as the reference structure is cubic.

(2) Dipole-Dipole Interaction:

This contribution to the energy comes from the long range interactions between the local modes at different sites. The dipole-dipole interaction energy is computed as follows:

$$E^{dpl} = \frac{1}{2}\sum_{ij,\alpha\beta}^{N} Q_{ij,\alpha\beta}u_{i\alpha}u_{i\beta} \tag{2.30}$$

where i and j run over the cell's numbers, α and β denote Cartesian components. The matrix $Q_{ij,\alpha\beta}$ is given by the following equation:

$$Q_{ij,\alpha\beta} = \frac{4Z^{*^2}}{\varepsilon_\infty}[\frac{\pi}{\Omega_c}\sum_{G\neq 0} exp(-\frac{|G|^2}{4\lambda^2})cos(G\cdot(R_i - R_j))G_\alpha G_\beta - \frac{\lambda^3}{3\sqrt{(\pi)}}\delta_{\alpha\beta}\delta_{ij}] \tag{2.31}$$

Here Ω_c is the unit cell volume, G are reciprocal lattice vectors, α and β are Cartesian components, ϵ_∞ is the optical dielectric constant. Since this dipole-dipole interaction is a long-range interaction, it takes a very long time to calculate it. To reduce computational time, the simple hunch is to fix the position of vectors R_i, R_j, and G. The Z^* is the Born effective charge for the soft mode, and is obtained as follows:

$$Z^* = \zeta_A Z_A^* + \zeta_B Z_B^* + \zeta_{O1} Z_{O1}^* + \zeta_{O2} Z_{O2}^* + \zeta_{O3} Z_{O3}^* \tag{2.32}$$

where ζ are the soft mode eigenvectors.

(3) Short-range energy:

The short-range energy is due to the interaction between the neighbouring local modes up to the

third nearest neighbours. The short-range energy is given as:

$$E^{short} = \frac{1}{2}\sum_{ij,\alpha\beta} J_{ij,\alpha\beta} u_{i\alpha} u_{j\beta} \tag{2.33}$$

The i and j are the unit cell indices and $i \neq j$; α and β are Cartesian components. Here $J_{ij,\alpha\beta}$ is the interaction matrix. Only seven distinct $J_{ij,\alpha\beta}$ parameters are possible as the reference structure has cubic symmetry. The interaction matrix for the cubic reference structure is to be determined from first principles calculation [78] as follows:

$$\begin{aligned} First\ \ nearest\ \ neighbors\ \ (NN) : J_{ij,\alpha\beta} &= (j_1 + (j_2 - j_1)|\hat{R}_{ij\alpha\beta}|)\delta_{\alpha\beta} \\ Second\ \ NN : J_{ij,\alpha\beta} &= (j_4 + 2(j_3 - j_4)|\hat{R}_{ij\alpha\beta}|)\delta_{\alpha\beta} \\ Third\ \ NN : J_{ij,\alpha\beta} &= j_6\delta_{\alpha\beta} + 3j_7\hat{R}_{ij\alpha}\hat{R}_{ij\beta}(1 - \delta_{\alpha\beta}) \end{aligned} \tag{2.34}$$

Where $R_{ij,\alpha}$ is a α component of $\frac{R_{ij}}{|R_{ij}|}$.

(4) Elastic Energy:

The elastic energy is a linear combination of two different energy terms corresponding to two different strains: (1) homogenous and (2) inhomogenous strain [78].

$$E^{elastic} = E_H^{elastic} + E_I^{elastic} \tag{2.35}$$

Here, $E_H^{elastic}$ and $E_I^{elastic}$ are the homogenous and inhomogeneous elastic energies and these energy are associated with strain tensors η_{il}, l=1,...,6 in Voight notations. The homogenous strain energy is given by

$$\begin{aligned} E_H^{elastic} = \frac{N}{2}B_{11}(\eta_{H,1}^2 + \eta_{H,2}^2 + \eta_{H,3}^2) + NB_{12}(\eta_{H,1}\eta_{H,2} + \eta_{H,2}\eta_{H,3} + \eta_{H,3}\eta_{H,1}) \\ + \frac{N}{2}B_{44}(\eta_{H,4}^2 + \eta_{H,5}^2 + \eta_{H,6}^2) \end{aligned} \tag{2.36}$$

Where B_{11}, B_{12}, and B_{44} are elastic constants expressed in energy units and N is the number of

primitive cells in the supercell. The inhomogeneous energy is given by:

$$E_I^{elastic} = \sum_i \{\frac{B_{11}}{4}[v_x(R_i - v_x(R_i \pm v_x)]^2 + \frac{B_{12}}{8}[v_x(R_i) - v_x(R_i \pm x)][v_y(R_i) - (R_i \pm y)] + \frac{B_{44}}{8}[v_x(R_i) - v_x(R_i \pm y) + v_y(R_i) - v_y(R_i \pm x)]^2 + cyclicpermutation\} \quad (2.37)$$

where $v(R_i)$ is the dimensionless local acoustic displacement which is related to the inhomogeneous strain.

(5) Elastic soft mode energy:

The on-site interaction is used to describe the relation between elastic deformations and local modes and is given as

$$E^{int} = \frac{1}{2}\sum_{i,l\alpha\beta} B_{l\alpha\beta}\eta_l(R_i)u_\alpha(R_i)u_\beta(R_i) \quad (2.38)$$

Where $\eta_{l\alpha\beta}(R_i)$ is the total strain variable and it contains both homogenous and inhomogenous parts of the unit cell i. $B_{l\alpha\beta}$ are parameters which are determined from first principles calcualtions. For cubic symmtery, only three coupling parameters are obtained: They are as follows:

$$B_{1xx} = B_{2yy} = B_{3zz}$$
$$B_{1yy} = B_{1zz} = B_{2xx} = B_{2zz} = B_{3yxx} = B_{3yy} \quad (2.39)$$
$$B_{4yz} = B_{4zy} = B_{5xz} = B_{5zx} = B_{6xy} = B_{6yx}$$

The inhomogeneous strain is given by

$$\eta_{I,1}(R_i) = \frac{1}{4}\sum_{d=0,y,z,y+z} [v_x(\mathbf{R}_i - d - \mathbf{x} - v_x(\mathbf{R}_i - d)] \quad (2.40)$$

$$\eta_{I,4}(R_i) = \frac{1}{4}\sum_{d=0,y,z,y+z} [v_x(\mathbf{R}_i - d - \mathbf{x} - v_x(\mathbf{R}_i - d) + v_y(\mathbf{R}_i - d - \mathbf{x} - v_y(\mathbf{R}_i - d)] \quad (2.41)$$

Here, $v(\mathbf{R}_i)$ is associated with position $\mathbf{R}_i+(\frac{a}{2}, \frac{a}{2}, \frac{a}{2})$.

All above discussions of effective Hamiltonian are intended for pure structures using the local soft mode in unit cell i, the homogeneous and inhomogeneous strain tensors as degree of freedoms. Additionally, we use pseudo-vector ω_i and magnetic dipole moment m_i degrees of freedoms to study pure $BiFeO_3$ (BFO) under pressure (Chapter 4) and $(BiFeO_3)_1/(NdFeO_3)_1$ ($(BFO)_1/(NFO_1)$) 1:1 superlattice (Chapter 5).

The effective Hamiltonian approach of Refs. [26-29] is used to investigate properties of BFO at finite temperature and under hydrostatic pressure, with the total energy being the sum of the following three terms:

$$E_{BFO} = E^{FE}(\{u_i\}, \{\eta\}) + E^{AFD}(\{u_i\}, \{\eta_l\}, \{\omega_i\}) + E^{MAG}(\{\mu_i\}, \{u_i\}, \{\eta_l\}, \{\omega_i\}) \quad (2.42)$$

E^{FE} represents the energy associated with the local modes, elastic strain interactions, and couplings between the local modes and strain; E^{AFD} ensembles the energies correlated with local mode, elastic deformations and AFD motions degrees of freedom and their couplings with the local modes, strains and AFD distortions; and E^{MAG} describes the energetics involving the magnetic and AFD interactions degrees of freedom and their couplings with the local modes and strains. Here $\{\eta_l\}$ is the total strain. The term E^{FE} contains the five terms described in Eq. (22). The second term

E^{AFD} in Eq. (2.42) is expressed as follows:

$$
\begin{aligned}
E^{\mathrm{AFD}} = & \sum_{i}[\kappa_A\omega_i^2 + \alpha_A\omega_i^4 + \gamma_A(\omega_{ix}^2\omega_{iy}^2 + \omega_{iy}^2\omega_{iz}^2 + \omega_{ix}^2\omega_{iz}^2)] \\
& + \sum_{ij}\sum_{\alpha\beta} D_{ij\alpha\beta}\omega_{i\alpha}\omega_{j\beta} + \sum_{i}\sum_{\alpha} D'\omega_{i,\alpha}^3(\omega_{i+\alpha,\alpha} + \omega_{i-\alpha,\alpha}) \\
& + \sum_{i}\sum_{\alpha\beta} C_{l\alpha\beta}\eta_l(i)\omega_{i\alpha}\omega_{i\beta} + \sum_{ij}\sum_{\alpha\beta} K_{ij,\alpha\beta}u_{j,\alpha}\omega_{i,\alpha}\omega_{i,\beta} \\
& + \sum_{i}\sum_{\alpha\beta\gamma\delta} E_{\alpha\beta\gamma\delta}\omega_{i\alpha}\omega_{i\beta}u_{i\gamma}u_{i\delta}
\end{aligned}
\tag{2.43}
$$

Here the sum over i is for all the Fe sites, and α, β, γ, and δ are Cartesian components along the pseudo-cubic [100], [010] and [001] directions, respectively. The first term of E^{AFD} represents the onsite contributions associated with the oxygen octahedral tilting. The second and third terms are associated with the short-range interactions between AFD motions, and sum over j for the Fe ions being first nearest neighbors of the Fe site i. The $\omega_{i+\alpha,\alpha}$ in the third term is the $\alpha-$ component of the AFD mode at the site shifted from the Fe site i to its nearest Fe neighbors along the α-axis. The fourth term represents the coupling between strain and AFD motions. The fifth and sixth terms of Equation (2.43) characterize couplings between AFD distortions and local modes via trilinear and biquadratic energetic contributions, respectively.

The term E^{MAG} in Eq. (2.42) is as follows[83]:

$$
\begin{aligned}
E^{\mathrm{MAG}} = & \sum_{ij\alpha\gamma} Q_{ij\alpha\gamma} m_{i\alpha} m_{j\gamma} + \sum_{ij\alpha\gamma} S_{ij\alpha\gamma} m_{i\alpha} m_{j\gamma} \\
& + \sum_{ij,\alpha\gamma\nu\delta} E_{ij,\alpha\gamma\nu\delta} m_{i\alpha} m_{j\gamma} u_{i\nu} u_{i\delta} \\
& + \sum_{ij,\alpha\gamma\nu\delta} F_{ij,\alpha\gamma\nu\delta} m_{i\alpha} m_{j\gamma} \omega_{i\nu} \omega_{i\delta} \\
& + \sum_{ijl,\alpha\gamma} G_{ijl,\alpha\gamma} \eta_l(i) m_{i\alpha} m_{j\gamma} \\
& + \sum_{ij} L_{ij} (\boldsymbol{\omega}_i - \boldsymbol{\omega}_j) \cdot (\boldsymbol{m}_i \times \boldsymbol{m}_j)
\end{aligned} \tag{2.44}
$$

Here α, γ, ν, δ denote the Cartesian components, and the indices i and j runs over all the Fe sites. The first term is the dipolar interactions between the magnetic moments, the second term is the short-range exchange coupling, the third, fourth, and fifth terms are the coupling between the magnetic moments with local modes, AFD motions and strains, and sixth term is a Dzyaloshinskii-Moriya (DM) interaction involving oxygen octahedral tiltings.

The effective Hamiltonian used to study the dynamics of the polar and antipolar modes in $(BFO)_1/(NFO_3)_1$ 1:1 superlattice is as follows:

$$
E_{BFO/NFO} = E_{BFO}(\{u_i\}, \{\eta_H\}, \{\eta_I\}, \{\omega_i\}, \{\, m_i\}) + E_{alloy}(\{u_i\}, \{\omega_i\}, \{m_i\}, \{\eta_{loc}\}) \tag{2.45}
$$

where E_{BFO} represents the effective Hamiltonian of pure BFO and is given in above subsection, while E_{alloy} characterizes the effect of substituting Bi ions by Nd ions and is associated with the local modes, strain, magnetic moment m_i, and pseudovector ω_i. The local quantity η_{loc} is also defined which is centered on Fe-site i as $\eta_{loc}(i) = \frac{\delta R_{ionic}}{8} \sum_j \sigma_j$, where the over j runs over the eight A nearest neighbors of eight Fe-site i and δR_{ionic} is the relative difference of ionic radius between

Nd and Bi ions. The analytical expression for E_{BFO} is defined above and for E_{alloy} is expressed as follows:

$$E_{alloy} = \sum_{i} \eta_{loc}(i) \left\{ \Delta\kappa_u \sum_{j} u_j^2 + \sum_{j,\alpha,\beta} K_{ij,\alpha\beta}^{Nd} \omega_{i,\alpha} \omega_{i,\beta} u_{j,\alpha} \right\} \tag{2.46}$$

Here the sum over i runs over all the Fe-sites and the sums over j and k run over the eight Bi (or Nd) ions nearest neighbors and over the six Fe nearest neighbors of the Fe-site i, respectively. α and β denotes Cartesian components, with the x-, y-, and z-axis being along the pseudo-cubic [100], [010], and [001] directions, respectively. The quantity $\Delta\kappa_u$ quantifies how the Nd-induced chemical pressure affects the harmonic energy of the local modes while $K_{ij,\alpha\beta}^{Nd}$ quantifies the trilinear coupling induced by the existence of Nd ions on the A-sublattice.

The details regarding the effective hamiltonian parameters used in this dissertation are available in Appendix A.

Chapter 3

UNIVERSAL ATOMISTIC MECHANISM LEADING TO COMPLEX ANTIFERROELECTRIC AND INCOMMENSURATE STRUCTURAL PATTERNS IN PEROVSKITES

The goal of this study is to reveal and investigate a novel elemental interatomic coupling in perovskite materials that bilinearly couples the antiferroelectric (AFE, see Chapter 1 for definition) displacement patterns of cations with the rotations of the oxygen octahedra. In particular, this new coupling explains a very complex crystal structure of prototypical antiferroelectric $PbZrO_3$ (PZO). It also provides a unified description of the complex antipolar structures of a variety of other perovskites, including the possible occurrence in them of incommensurate phases. Incommensurate phases are found in aperiodic crystals in which the periodic crystal structure is incommensurate with the displacement pattern.

3.1 Background

PZO's ground state displays the *Pbam* symmetry and is characterized by three significant phonon modes [38, 39, 40, 41, 43]. The first of these modes is labeled R_4^+ according to its symmetry and is rather simple in the sense that it corresponds to typical antiphase tilting. This mode is associated with the zone boundary $\frac{2\pi}{a_{\text{lat}}}(\frac{1}{2},\frac{1}{2},\frac{1}{2})$ k-point of the cubic first-Brillouin zone, where a_{lat} is the lattice constant of the five atom cubic perovskite unit cell. The other two modes are much more complex and are Σ_2 and S_4 modes. These modes are associated with the $\frac{2\pi}{a_{\text{lat}}}(\frac{1}{4},\frac{1}{4},0)$ and $\frac{2\pi}{a_{\text{lat}}}$ $(\frac{1}{4},\frac{1}{4},\frac{1}{2})$ wave vectors, respectively. Some recent works [38, 39, 40] suggested that a trilinear coupling between R_4^+, Σ_2, and weaker S_4 modes plays an important role to stabilize the Pbam ground state

of PZO. However, this trilinear energy only amounts to 27 meV per formula unit (f.u.) out of the 392 meV/fu gain of the ground state with respect to the cubic paraelectric phase, according to first-principles calculations [40], and does not explain why the unusual Σ_2 and S_4 modes are strongly unstable in PZO. One may, therefore, wonder if another energy plays a crucial role in the stability of the complex structural modes in PZO. One can also ask if such hypothetical energy can further describe other complex antipolar states that many materials are known to exhibit and may also be of relevance to the formation of incommensurate phases in perovskites. Here, we report the discovery of a novel atomistic energy that bi-linearly couples the A-cation displacements and oxygen octahedral tilting in ABO_3 perovskites and which provides a unified description of many antiferroelectric and incommensurate structures of perovskites.

3.2 Microscopic description of the new interaction

Let us start with the convention that B-cations of the perovskite system are at the corners (i.e. at $(\frac{1}{2}, \frac{1}{2}, \frac{1}{2})$ coordinate) of the reference five-atom cell and the A-cations are at the cell center (i.e. at (0,0,0) coordinate). Let $\mathbf{u_i}$ be the off-center displacement of A-site cation at cell i. $\omega_\mathbf{i}$ is the pseudovector that characterizes the tilting of the oxygen octahedron centered on the B-site at unit cell i. The direction of the $\omega_\mathbf{i}$ gives the axis about which the oxygen octahedral rotates and its magnitude is the rotation angle [80]. Different types of coupling between $\{\mathbf{u}_i\}$ and $\{\boldsymbol{\omega}_i\}$ have been reported in literature as follows:

(1) bi-quadratic couplings which are quadratic in both $\mathbf{u}$ and ω explains the repulsion between polar

and O_6-rotational distortions [80].

(2) coupling between **u** and ω when **u** is linear and ω is quadratic or cubic in ω has been shown to achieve collaborative effects involving both types of variables [8], as in the case of the so-called hybrid improper ferroelectrics [2, 7, 84].

(3) when the coupling is of the form $u^2\omega$, it is shown to have the origin of inhomogeneous states and novel magneto-electric effects [85].

I found that above mentioned interaction terms cannot explain the occurrence of PZO's Σ_2 mode. Then I decided to investigate the possibility that the polar and rotational variables *linearly* couple, a question that, as far as I know, has never been discussed in literature.

The simplest atomistic bilinear energy that we found has the (analytical) form:

$$\Delta E = \mathcal{K} \sum_{i} \sum_{l,m,n=0,1} \sum_{\alpha,\beta,\gamma=x,y,z} \epsilon_{\alpha\beta\gamma} u_{i,\alpha}\, \omega_{ilmn,\beta} (-1)^{(l\mathbf{x}+m\mathbf{y}+n\mathbf{z})_\gamma} \tag{3.1}$$

where $\mathcal{K}$ is a material-dependent constant that characterizes the strength of this coupling. The sum over i runs over all the five-atom cells of the perovskite structure, and α=x, y,z subscripts denote the Cartesian components of the $\mathbf{u}_i$ vectors and $\boldsymbol{\omega}_i$ pseudo-vectors – with the x, y and z-axes being chosen along the pseudo-cubic [100], [010] and [001] directions, respectively. $\boldsymbol{\omega}_{ilmn}$ (with l,m,n = 0 or 1) represents the $i-th$ component of the tilting pseudo-vector located at lattice vector $\mathbf{R}_{lmn} = a_{\mathrm{lat}}(l\mathbf{x} + m\mathbf{y} + n\mathbf{z})$. Moreover, $(l\mathbf{x} + m\mathbf{y} + n\mathbf{z})_\gamma$ is the γ component of the vector in parenthesis. $\epsilon_{\alpha\beta\gamma}$ is the Levi-Civita symbol, it is equal to 1 when the ordered triad $\alpha\beta\gamma$ forms a right-handed system, -1 when left-handed, and 0 when there are repeated indexes. The energy

of Eqn. (3.1) is scalar as it should be, and, physically, it couples rotations of the tilting modes with the displacements of cations. Such coupling has not been considered yet and may have a strong potential for the description of the ground state of ferroelectrics having a complex structure. We will show below that this coupling can also explain incommensurate phases of ferroelectrics. Such coupling also implies that the atomic displacements in antiferroelectrics are not independent of the tiltings. There is an intimate connection between the oxygen octahedra tiltings and atomic displacements. For example, Eqn. (3.1) implies that a very complex pattern of the shift of lead ions in PZO can be triggered by the antiferrodistortive phase transition related to the condensation of the oxygen octahedral tilting below some temperature. In this case, the bilinear coupling of Eqn. (3.1) plays the role of an external conjugate field on the lead ions, due to the appearance of a finite average $\langle \omega_i \rangle$. To show the dependence of this energy on the wave vector k let us now consider distortions given by:

$$\begin{aligned} u_{i,\alpha} &= A_\alpha \{\exp[i(\mathbf{k}_\alpha \cdot \mathbf{R}_i + \phi_\alpha)] + \text{c.c.}\}, \\ \omega_{i,\alpha} &= A'_\alpha \{\exp[i(\mathbf{k}'_\alpha \cdot \mathbf{R}_i + \phi'_\alpha)] + \text{c.c.}\}, \end{aligned} \tag{3.2}$$

where $\mathbf{R}_i$ is the lattice vector corresponding to cell i and $\alpha = x, y, z$. The $\mathbf{k}_\alpha$ wave vectors characterize the spatial modulation of each of the components of the $\mathbf{u}_i$ vectors. Similarly, the $\mathbf{k}'_\alpha$ vectors define, in direction and length, the modulated distortions of the Cartesian components of the $\boldsymbol{\omega}_i$ pseudo-vectors. The A_α and A'_α scalars quantify the magnitude of u and ω distortions, respectively. The ϕ_α and ϕ'_α angles are phases characterizing specific u and ω patterns, respectively. By inserting Eqn. (3.2) into Eqn. (3.1), we can identify which combinations of $\mathbf{k}_\alpha$ and $\mathbf{k}'_\alpha$ wave

vectors result in the interaction via this new coupling. So, if we know the modes in a material, we can check if they give a finite contribution to the novel energy term. Figure 3.1 schematizes coupling terms inherent to Eqn. (3.1). Equation (3.1) for the energy can be rewritten as now:

$$\frac{\Delta E}{\mathcal{K}} = \sum_{\alpha,\beta=x,y,z} A_\alpha A'_\beta \sum_{\mathbf{G}} [f_{\alpha\beta}\delta(\mathbf{G} - \mathbf{k}_\alpha - \mathbf{k}'_\beta) + f^*_{\alpha\beta}\delta(\mathbf{G} + \mathbf{k}_\alpha + \mathbf{k}'_\beta) + g_{\alpha\beta}\delta(\mathbf{G} + \mathbf{k}_\alpha - \mathbf{k}'_\beta) + g^*_{\alpha\beta}\delta(\mathbf{G} - \mathbf{k}_\alpha + \mathbf{k}'_\beta)] \tag{3.3}$$

where δ is the Dirac delta function and $\mathbf{G}$ runs over the reciprocal lattice vectors corresponding to the 5-atom cubic perovskite structure. The $f_{\alpha\beta}$ and $g_{\alpha\beta}$ coefficients are given by

$$f_{\alpha\beta} = \exp[i(\phi_\alpha + \phi'_\beta)]a_{\alpha\beta} \tag{3.4}$$

and

$$g_{\alpha\beta} = \exp[i(-\phi_\alpha + \phi'_\beta)]a_{\alpha\beta}, \tag{3.5}$$

where

$$a_{\alpha\beta} = \sum_{\eta=x,y,z} \epsilon_{\alpha\beta\eta} \prod_{\gamma=x,y,z} [1 + (-1)^{\delta_{\gamma\eta}} \exp(ik'_{\beta,\gamma}a_{\text{lat}})] \tag{3.6}$$

with $\delta_{\gamma\eta}$ being the delta function and $k'_{\beta,\gamma}$ the γ-component of the $\mathbf{k}'_\beta$ vector.

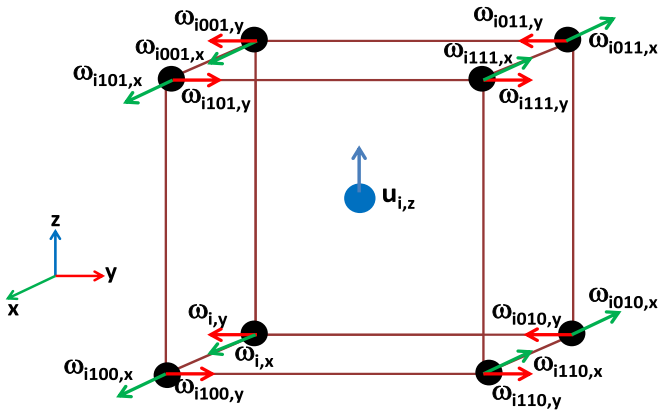

Figure 3.1: Schematic representation of coupling terms in ΔE of Eqn. (1). Only the couplings involving $u_{i,z}$ are shown here. The blue arrow on the central A cation stands for the $u_{i,z}$ displacement. The green and Red arrows on the corner B cations represent the x and y components, respectively of the ω pseudovectors.

In the next section, we will see how the investigated atomic interaction helps us to understands the complex displacement patterns caused by this bilinear coupling in some perovskites.

3.3 Applications of the Model

We investigated several complex distortion patterns for possible occurrence of AFE and other complex instabilities in perovskite lattices.

3.3.1 Σ_2 antiferroelectric mode

Σ_2 is a frozen structural mode in PZO ground state and it possesses antipolar Pb motions (which are also referred as AFE displacements) along with oxygen octahedral rotations. The k-point associated with the Σ_2 AFE mode is the $\frac{2\pi}{a_{\text{lat}}}(\frac{1}{4},\frac{1}{4},0)$ k-point. Let us start with the $\mathbf{k}_x = \mathbf{k}_y = \frac{\pi}{2a_{\text{lat}}}(\mathbf{x}+\mathbf{y})$ wave vectors. For these k-vectors, the Dirac functions of the type $\delta(\mathbf{G} - \mathbf{k}_\alpha - \mathbf{k}'_\beta)$ in Eqn. (3.3) imply

that for $\mathbf{k}'_\beta = -\mathbf{k}_x = -\mathbf{k}_y$, we have a finite interaction contributing to $\Delta E/\mathcal{K}$. For this choice of the wave vectors, one can see from Eqn. (3.6) that $a_{xy} = a_{yx} = 0$. When $\mathbf{k}'_z = -\mathbf{k}_x = -\mathbf{k}_y$, a_{xz} and a_{yz} in Eq. (3.6) are finite and Eq. (3.3) becomes:

$$\frac{\Delta E(\Sigma_2)}{\mathcal{K}} = -8A_xA'_z\cos(\phi_x + \phi'_z) + 8A_yA'_z\cos(\phi_y + \phi'_z) \tag{3.7}$$

Here we discuss two different cases when this interaction is maximum.

Case (I):

The interaction is maximum when $\phi_x + \phi'_z = \phi_y + \phi'_z = \pi n$, with $n \in \mathbb{Z}$, provided that A_x and A_y have opposite signs. For instance, when $\phi_x = \phi_y = -\frac{3\pi}{4}$ and $\phi'_z = -\frac{\pi}{4}$, the coupling is maximum. Since $\phi'_z - \phi_x = \frac{\pi}{2}$, the A-cation displacements are out-of-phase with respect to the AFD distortions by 90° and the resulting patterns are shown in Figure 3.2(a) and 3.2(b), respectively. The pattern of Pb displacements, i.e u_i vectors, are either parallel or antiparallel to pseudocubic $[\bar{1}10]$ direction. The u_i's in the Σ_2 phonon mode follows a "++- -" sequence, when lead ions move along [100] or [010] pseudocubic direction in (001) planes. Pseudovector ω_i characterizes the oxygen octahedron tilting at B site in unit cell i. Figure 3.2(c) displays the oxygen motions associated with the tilting of the oxygen octahedra in the Σ_2 phonon mode. One can see that out of the four in-plane oxygen ions surrounding any B cation, only two move. Such distortion arises when the individual $\omega_{i,z}$ rotation about z axis displays a "++- -" modulation pattern along in-plane [100] or [001] directions. These AFD modes are qualitatively different from the Glazer rotational patterns [15] which always involve "+-+-" (zone-boundary) modulations in the plane perpendicular to the rotation axis. Both AFE and AFD modes interact at harmonic level and such bilinear coupling can be explained by the

investigated atomic interaction. Therefore, the coupling in Eq.(3.1) naturally explains the exotic character of the AFE order in PZO and other materials that share similar features (e.g., $PbHfO_3$, which is denoted below as PHO[43, 86]).

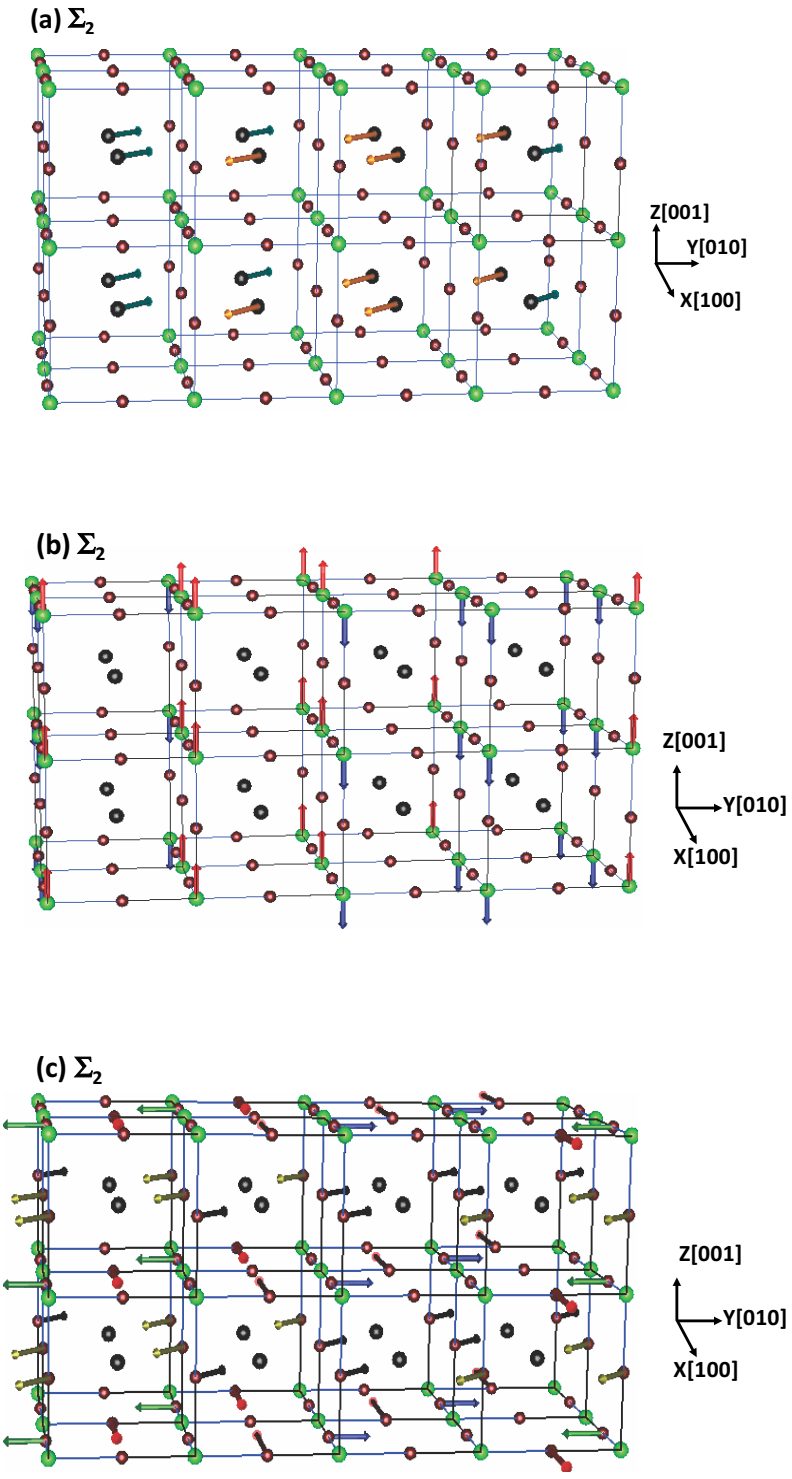

Figure 3.2: (a) *A*-cation distortion (*ui*) patterns, (b) *B*-centered oxygen octahedra rotation pseudovectors ω_i, and (c) Oxygen displacements. The A, B, and O ions are shown in black, green, and red spheres respectively. The different colors used for the arrows in each panel emphasize different directions of the corresponding vectors.

Case II:

Let us consider the case of interaction (Eqn. (3.7)) that can also lead to solutions that are not associated with the PZO's AFE patterns. For example, if we choose $\phi_x = \phi_y = \phi_z^{'} = -\frac{\pi}{2}$, we get:

$$\frac{\Delta E(\Sigma_2)}{\mathcal{K}} = (8A_xA_z' - 8A_yA_z') \tag{3.8}$$

This leads to a different pattern for the A-cation displacements and oxygen octahedral tiltings. Specifically, Eqn. (3.2) gives "0+0-" modulations.

Both cases discussed above give perfectly degenerate patterns at harmonic level. PZO and PHO adopt the former case due to anharmonic coupling between local dipoles and tiltings. The energies associated with anharmonic coupling for pattern "0+0-" are higher than in pattern "++- -" due to the fact that "+" and "-" displacements in "0+0-" modulations are larger by the factor of $\sqrt{2}$ in magnitude than in "++- -".

3.3.2 S_4 symmetry antiferroelectric mode

S_4 is another structural mode in the antiferroelectric Pbam phase of PZO. The modes which contribute to Pbam ground state of PZO and PHO. The k-point associated with S_4 mode is $\frac{2\pi}{a_{\text{lat}}}$ $(\frac{1}{4},\frac{1}{4},\frac{1}{2})$. The investigated bilinear coupling gives u_i(AFE) and O_6 (AFD) patterns as shown in Figures 3.3(a), 3.3(b), and 3.3(c) for the following case:

Let us choose $\mathbf{k}_x = \mathbf{k}_y = \frac{\pi}{2a_{\text{lat}}}(\mathbf{x}+\mathbf{y}) + \frac{\pi}{a_{\text{lat}}}\mathbf{z}$ in Eqn. (3.2). For $\mathbf{k'}_x = \mathbf{k'}_y = -\mathbf{k}_x = -\mathbf{k}_y$, we have non vanishing interactions terms in Eqn. (3.3) via the $\delta(\mathbf{G} - \mathbf{k}_\alpha - \mathbf{k'}_\beta)$ term. One can find that only a_{xy}

and a_{yx} terms are finite and resulting Eqn. (3.1) for S_4 mode becomes:

$$\frac{\Delta E(S_4)}{\mathcal{K}} = 8A_xA'_y \sin(\phi_x + \phi'_y) - 8A_yA'_x \sin(\phi_y + \phi'_x) \tag{3.9}$$

The interaction of S_4 mode will be maximized when $\phi_x + \phi'_y = \phi_y + \phi'_x = \frac{\pi}{2} + \pi n$, where $n \in \mathbb{Z}$, provided that $A_xA'_y$ and $A_yA'_x$ have opposite signs. Let $\phi_x = \phi_y = -\frac{\pi}{4}$ and $\phi'_x = \phi'_y = \frac{3\pi}{4}$, then the interaction in Eqn. (3.9) yields patterns for A-cation displacements and tiltings shown in Figs. 3.3(a) and 3.3(c), respectively. Thus S_4 mode is also stabilized by interaction Eqn. (3.1). Hence, the investigated atomic interaction explains all complex patterns of atomic distortions associated with the *Pbam* ground state of PZO and PHO.

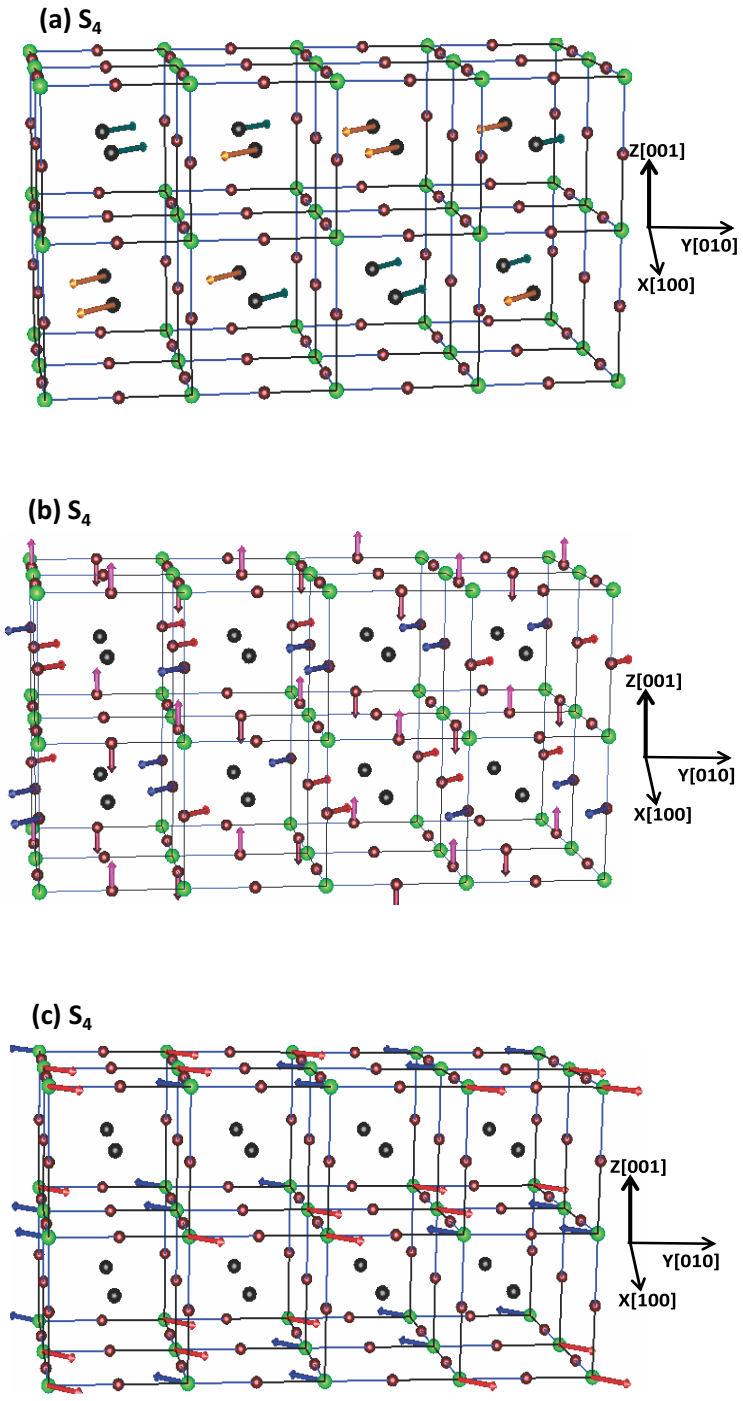

Figure 3.3: (a) *A*-cation distortion (*ui*) patterns, (b) *B*-centered oxygen octahedra displacements, and (c) *B*-centered oxygen rotation pseudovectors ω_i for S_4. The A, B, and O ions are shown in black, green, and red spheres respectively. The different colors used for the arrows in each panel emphasize different directions of the corresponding vectors.

3.3.3 Λ_3 antiferroelectric mode

In $BiFeO_3$ and $BiFe_{1/2}Sc_{1/2}O_3$ complex atomic patterns which contribute to antipolar Pnma structure [87, 88] can be also explained by the bi-linear coupling of Eq. (3.1). The Λ_3 mode is associated with $2\pi/a_{\rm lat}$ (1/4,1/4,1/4) k-points. Let the x and y components of the A-cation displacements be described by $u_{i,x} = u_{i,y} = A\cos(\{\mathbf{k_1}_x \cdot \mathbf{R}_i + \phi_x\}) + A\cos(\{\mathbf{k_2}_x \cdot \mathbf{R}_i + \phi_x\})$, where $\phi_x = \frac{\pi}{4}$, $\mathbf{k_1 x} = \frac{\pi}{2a_{lat}}(\mathbf{x}+\mathbf{y}+\mathbf{z})$ and $\mathbf{k_2 x} = \frac{\pi}{2a_{lat}}(\mathbf{x}+\mathbf{y}-\mathbf{z})$ are the different k-vectors associated with the Λ_3 mode as shown in Figure 3.4(a). Figure 3.4(a) shows that $u_{i,z} = C\cos(\{\mathbf{k_1}_x \cdot \mathbf{R}_i + \phi_z\}) - C\cos(\{\mathbf{k_2}_x \cdot \mathbf{R}_i + \phi_z\})$, with $\phi_z = -\frac{3\pi}{4}$. The x and y components of the tilting ω's are active in this mode while the z-components is null; thus we have $\omega_{i,x} = -\omega_{i,y} = A'\cos(\{-\mathbf{k_1}_x \cdot \mathbf{R}_i + \phi'_{1x}\}) + A'\cos(\{-\mathbf{k_2}_x \cdot \mathbf{R}_i + \phi'_{2x}\})$, with $\phi'_{1x} = 0$ and $\phi'_{2x} = \frac{\pi}{2}$ (see Figure 3.4(c)). We obtain ΔE by inserting two different k-vectors in Eq. (3.1).

$$\begin{aligned}\frac{\Delta E(\Lambda_3)}{\mathcal{K}} &= 8CA'[\cos(\phi_z + \phi'_{1x}) + \sin(\phi_z + \phi'_{1x}) - \cos(\phi_z + \phi'_{2x}) + \sin(\phi_z + \phi'_{2x})] \\ &\quad - 8AA'[\cos(\phi_x + \phi'_{1x}) + \sin(\phi_x + \phi'_{1x}) - \cos(\phi_x + \phi'_{2x}) + \sin(\phi_x + \phi'_{2x})] \\ &= -16\sqrt{2}(CA' + AA')\end{aligned} \tag{3.10}$$

This contribution is finite. Thus, our discovered bi-linear coupling of Eq. (3.1) can also explain the occurrence of the atomic patterns displayed in Figure (3.4).

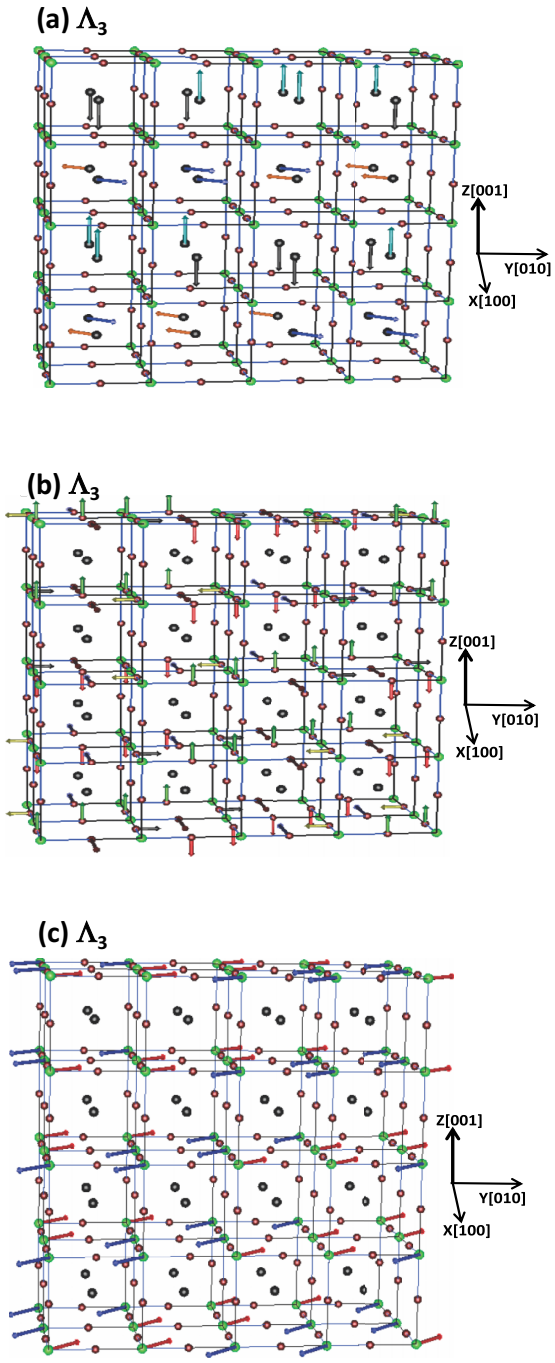

Figure 3.4: (a) *A*-cation distortion (*ui*) patterns, (b) oxygen displacements, and (b) *B*-centered oxygen octahedra rotation pseudovectors ω_i for Λ_3 mode. The A, B, and O ions are shown in black, green, and red spheres respectively. The different colors used for the arrows in each panel emphasize different directions of the corresponding vectors.

3.3.4 Modes along the Σ line

The Σ line is the line joining the center and boundary M-point of the Brillouin zone. Let us start with the wave vectors, which correspond to the center, i.e Γ point, and M-point, which is given by $(\frac{\pi}{a_{\text{lat}}})(\hat{\mathbf{x}} + \hat{\mathbf{y}})$ point in the reciprocal space. We thus have $\mathbf{k}_x = \mathbf{k}_y = (\frac{\lambda\pi}{a_{\text{lat}}})(\hat{\mathbf{x}} + \hat{\mathbf{y}})$, where λ is a real number between 0 and 1. Inserting these k-vectors in Eq. (3.1) via Eq. (3.2), we get

$$\frac{\Delta E(\Sigma)}{\mathcal{K}} = 8\sin(\lambda\pi)[A_x A'_z \sin(\phi_x + \phi'_z - \lambda\pi) - A_y A'_z \sin(\phi_y + \phi'_z - \lambda\pi)]. \tag{3.11}$$

Several important conclusions can be drawn from this result:

(1) when $\lambda = 0$ or $\lambda = 1$, $\sin(\pi\lambda)$=0, which implies that the effect of the discovered coupling is null at the center i.e Γ ($\lambda = 0$) and M ($\lambda = 1$) points. In contrast, the intermediate k points along the Σ line are affected by the new coupling. For example, such coupling explains modulations of the O_6 rotations when material has A-cation displacements in Li-doped $NdTiO_3$ [89].

(2) for any selected k point in the Σ line, the magnitude of the coupling is maximum when $\phi_x + \phi'_z$ and $\phi_x + \phi'_z$ take values of the form $\pi/2 + \lambda\pi + \pi n$, where $n \in \mathbb{Z}$. The magnitude of the coupling is maximum for any k-point provided that A_x and A_y have opposite signs.

(3) For *non-rational* values of λ, we get the finite coupling energy. This indicates that our new interaction can be responsible for the formation of *incommensurate* perovskite phases.

3.3.5 Phonon spectra and incommensurability

The proposed coupling energy also explains the phonon bands of some perovskite materials. As a matter of fact, taking the second derivative of the energy with respect to the modulated polar

distortions and octahedral rotations gives:

$$
\begin{aligned}
E''_u(\lambda) &= \frac{\partial^2 E}{\partial u(\lambda)^2} = F_u + G_u cos(\lambda\pi) \\
E''_\omega(\lambda) &= \frac{\partial^2 E}{\partial \omega(\lambda)^2} = F_\omega + G_\omega cos(\lambda\pi) \\
E''_{u\omega}(\lambda) &= \frac{\partial^2 E}{\partial u(\lambda)\partial \omega(\lambda)} = H_{u\omega} sin(\lambda\pi),
\end{aligned}
\tag{3.12}
$$

The F and G parameters characterize energetics of the **u** and ω variables. The $H_{u\omega}$ is a coupling parameter which is derived from Eqn.(3.11) by taking $sin(\phi_x + \phi'_z - \lambda\pi) = sin(\phi_y + \phi'_z - \lambda\pi) = 1$. The diagonal terms of this k-dependent Hessian matrix along the Σ line represent typical energetics of polar and AFD bands. Eigenvalues of this two-state Hamiltonian can be obtained analytically:

$$
\begin{aligned}
\kappa_-(\lambda) &= \frac{E''_u(\lambda) + E''_\omega(\lambda)}{2} - \frac{\sqrt{(E''_u(\lambda) + E''_\omega(\lambda))^2 - 4(E''_u(\lambda)\, E''_\omega(\lambda) - H^2_{u\omega} \sin^2(\lambda\pi))}}{2} \\
\kappa_+(\lambda) &= \frac{E''_u(\lambda) + E''_\omega(\lambda)}{2} + \frac{\sqrt{(E''_u(\lambda) + E''_\omega(\lambda))^2 - 4(E''_u(\lambda)\, E''_\omega(\lambda) - H^2_{u\omega} \sin^2(\lambda\pi))}}{2},
\end{aligned}
\tag{3.13}
$$

Note that, whenever we have negative eigenvalues κ_- or κ_+, the corresponding k-points constitute an instability of the cubic perovskite structure.

Let us consider two choices of the parameters of this model and discuss the phenomenology that our simple model can yield:

case I:

Let us consider three different increasing values for the $H_{u\omega}$ coupling parameters: 31.6, 54.8, and 316.2. Figures 3.5(a), 3.5(b) and 3.5(c) display the results of $E''_u(\lambda) = -75 - 75cos(\pi\lambda)$ and $E''_\omega(\lambda) = -75 + 125cos(\pi\lambda)$ along with $\kappa_\pm(\lambda)$.

(a) $\underline{H_{u\omega}}$=31.6

Figure 3.5(a) displays that $E''_u(\lambda)$ is the lowest at Γ and rapidly increases with λ. This is the indication of strong ferroelectric instability of displacive character. One should note that small value of coupling parameter $H_{u\omega}$ results in a small gap between the $\kappa_-(\lambda)$ and $\kappa_+(\lambda)$ bands and the associated eigenvectors change character as a function of λ. Thus, for example, the distortion mode associated with the smaller eigenvalue κ_- is strongly polar close to Γ (with $\kappa_-(\lambda \approx 0) \sim E''_u(\lambda \approx 0)$), but it is rotational-like close to M (with $\kappa_-(\lambda \approx 1) \sim E''_\omega(\lambda \approx 1)$). Such features are typical of an avoided crossing (anticrosssing) between bands, as we have in this case.

(b) $\underline{H_{u\omega}}$=54.8

Figure 3.5(b) shows that $E''_u(\lambda)$ increases with λ: it is minimum for $\lambda = 0$ and maximum at $\lambda = 1$. $E''_\omega(\lambda)$ is minimal at the M-point indicating that there is strong AFD instability and rapidly increases for decreasing λ. As $H_{u\omega}$ grows (Fig. 3.5(b)), the $\kappa_-(\lambda)$ is rather insensitive to λ for a wide interval around $\lambda = 1/2$.

(c) $\underline{H_{u\omega}}$=316.2

Figure 3.5(c) demonstrate that the minimum of $E''_\omega(\lambda)$ is lower than the minimum of $E''_u(\lambda)$ which indicates that the AFD instability is stronger than the ferroelectric one. For $H_{u\omega}$ above a critical value (Fig. 3.5(c)), the minimal value of κ_- is obtained at $\lambda = 1/2$, i.e., the unstable mode has a hybrid $u - \omega$ character in that case.

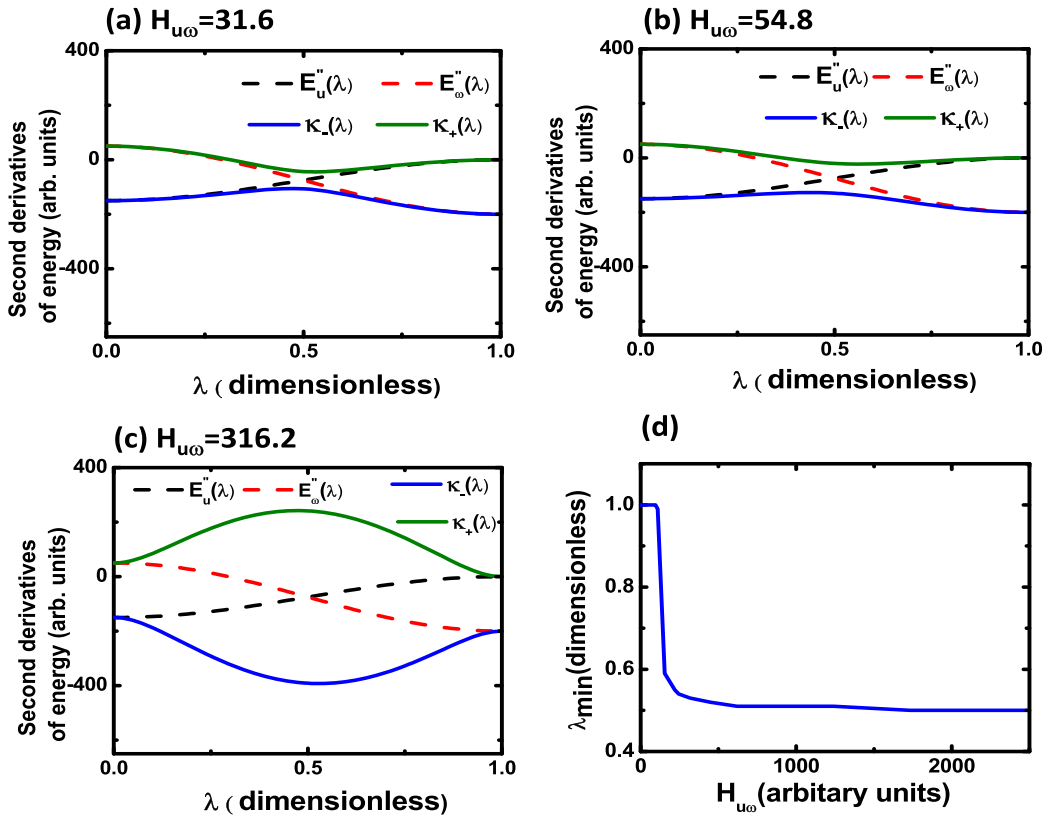

Figure 3.5: Dependencies of $E''_u(\lambda)$, $E''_\omega(\lambda)$, $\kappa_-(\lambda)$ and $\kappa_+(\lambda)$ along the Σ line for three different cases, in arbitrary units: (a) $H_{u\omega} = 31.6$, (b) $H_{u\omega} = 54.8$, (c) $H_{u\omega} = 316.2$, and (d) display the $\lambda_m in$ value of λ at which $\kappa_-(\lambda)$ is minimum, as a function of $H_{u\omega}$.

The phonons along the Σ line in cubic PZO computed from first principles [90] seem to correspond to the case in Fig. 3.5(b). The soft Σ mode of PZO has hybrid character and displays a very flat branch of AFE-like phonons connecting the M and R k-points [38], where $\mathbf{k}_R = \frac{\pi}{a_{\text{lat}}}(\mathbf{x} + \mathbf{y} + \mathbf{z})$. The dominant instability of the cubic phase is the AFD one at the boundary of the Brillouin zone. Cubic PZO has AFD-type instability at the boundary of the Brillouin zone. Hence, at the harmonic level, PZO has a regular AFD-type ground state, as opposed to the AFE one it actually displays. The work of Ref. [38] demonstrates that the PZO's AFE phase is further

stabilized by a trilinear coupling between R_4^+, Σ_2, and S_4 structural modes.

Case II:

This case corresponds to three different increasing values of $H_{u\omega}$ coupling parameters: 31.6, 54.8, and 438.2 for the diagonal elements given by the following formulas $E_u''(\lambda) = -192.5 - 2.5cos(\pi\lambda)$ and $E_\omega''(\lambda) = -75 + 125cos(\pi\lambda)$ along with coupled $\kappa_\pm(\lambda)$ eigenvalues.

(a) $H_{u\omega}$=31.6

Figure 3.6(a) displays that $E_u''(\lambda)$ is still the lowest at $\lambda = 0$ but its dependence on λ is relatively weak compared to $E_\omega''(\lambda)$. This minimum of $E_u''(\lambda)$ is only slightly higher than the M-point minimum of $E_\omega''(\lambda)$.

(b) $H_{u\omega}$=54.8

Figure 3.6(b) demonstrates that with increase of $H_{u\omega}$, the minimum of $\kappa_-(\lambda)$= $\kappa_-(\lambda_{min})$ is displaced in the direction from M point towards $\lambda = \frac{1}{2}$. $E_u''(\lambda)$ and $E_\omega''(\lambda)$ have the same trend at $H_{u\omega}$=31.6:λ_{min} equals 0.69.

(c) $H_{u\omega}$=438.2

From Figure 3.6(c), one can see that the minimum of $\kappa_-(\lambda)$ corresponds to the minimum of $E_\omega''(\lambda)$ at $\lambda = 1$. The cross-coupling $E_{u\omega}''(\lambda)$ in Eqn.(3.12) favors the minimum at $\lambda = \frac{1}{2}$ for any large value of $H_{u\omega}$. Hence, λ_{min} possesses different values depending on the strength of $H_{u\omega}$ and this value can be arbitrary.

Figure 3.6(d) shows that $\lambda_{\min}$ is a *continuous* function of $H_{u\omega}$, which implies that the dominant instability of our model may correspond to arbitrary long-range, even incommensurate, distortions

of the perovskite lattice. Incommensurate solutions with $0 < \lambda_{\min} < \frac{1}{2}$ can be obtained for other choices of the model parameters. Moreover, here we chose to focus on the Σ line, but it would be straightforward to extend our analysis to other lines joining the center and other boundary points of the Brillouin zone. This might permit an explanation of incommensurate phases reported in literature, as e.g. those in Ref. [91]. Let us stress that the incommensurate distortion involves both the *A*-cation displacements and AFD motions, since the eigenvector corresponding to $\kappa_{-}(\lambda)$ combines both features. The results of this analysis are thus reminiscent of the Neutron Rietveld refinement of the incommensurate phase of the $Pb(Co,W)O_3$ compound, revealing mixing of significant shifts of the Pb atoms and rather complex tilts of oxygen octahedra [92].

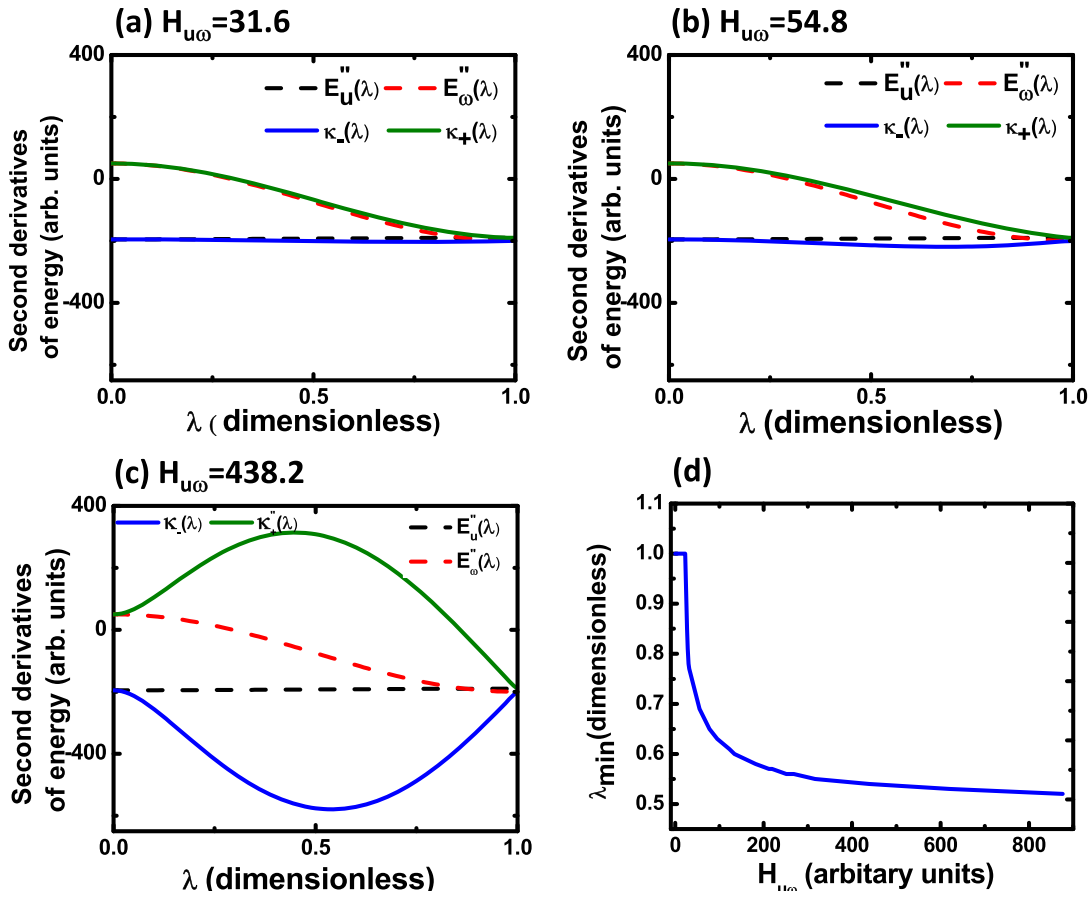

Figure 3.6: Dependencies of $E''_u(\lambda)$, $E''_\omega(\lambda)$, $\kappa_-(\lambda)$ and $\kappa_+(\lambda)$ along the Σ line for three different cases, in arbitrary units: (a) $H_{u\omega} = 31.6$, (b) $H_{u\omega} = 54.8$, (c) $H_{u\omega} = 438.2$, and (d) display the $\lambda_m in$ value of λ at which $\kappa_-(\lambda)$ is minimum, as a function of $H_{u\omega}$.

3.4 Discussion

Our prediction that non-periodic structures can arise from investigated bilinear (microscopic) coupling between polar and rotational variables bears a strong resemblance with the (phenomenological) theory proposed by Heine and McConnell (HM) [93], which is based on the coupling between two different structural modes. These two different modes were denoted as ψ and φ and

were coupled by the interaction energy as follows:

$$\Delta E_{int}^{\mathrm{HM}} = h(\varphi\nabla\psi - \psi\nabla\varphi), \tag{3.14}$$

where h is a constant and ∇ is the gradient operator in one dimension. The right-hand side of Eqn. (3.14) represent the Lifshitz invariant [94] and has been used in many phenomenological descriptions of incommensurate crystals [95].

In Eqn. (3.1), certain $\mathbf{u}_i$ is coupled to the spatial derivatives of $\boldsymbol{\omega}_i$ and, in continuum limit, Eqn. (3.1) can be rewritten as $\sim \mathbf{u} \cdot (\nabla \times \boldsymbol{\omega})$. Alternatively, the microscopic Eq. (3.1) can equally be rewritten by choosing a specific $\boldsymbol{\omega}_i$ at a given B-site i and considering its coupling with the spatial derivatives of the u-displacements. The continuum limit is $\sim \boldsymbol{\omega} \cdot (\nabla \times \mathbf{u})$. The combined formula for the continuum variant of Eqn. (3.1) is therefore:

$$\Delta E_{cont} = \frac{\mathcal{K}}{2}\{\mathbf{u} \cdot (\nabla \times \boldsymbol{\omega}) + \boldsymbol{\omega} \cdot (\nabla \times \mathbf{u})\} \tag{3.15}$$

Here, Eqn. (3.15) contains a term of the form $(u_x \frac{\partial \omega_z}{\partial y} - \omega_z \frac{\partial u_x}{\partial y})$, which is similar to Eq. (3.14) when choosing $\varphi = u_x$, $\psi = \omega_z$ and taking the gradient to be the partial derivative with respect to y. However, Equation (3.15) is more general than the interaction proposed by Heine and McConnell, since it contains five other, symmetry-equivalent terms, namely $(-u_y \frac{\partial \omega_z}{\partial x} + \omega_z \frac{\partial u_y}{\partial x})$, $(-u_x \frac{\partial \omega_y}{\partial z} + \omega_y \frac{\partial u_x}{\partial z})$, $(u_y \frac{\partial \omega_x}{\partial z} - \omega_x \frac{\partial u_y}{\partial z})$, $(u_z \frac{\partial \omega_y}{\partial x} - \omega_y \frac{\partial u_z}{\partial x})$, and $(-u_z \frac{\partial \omega_x}{\partial y} + \omega_x \frac{\partial u_z}{\partial y})$. In fact, the general form of Equation (3.15), that involves the sum of (i) a dot product between a first vector, which is

polar, and curl of the second vector, which is axial, and (ii) another dot product that is now between the second vector and the curl of the first vector, constitutes an energy invariant that has never been previously proposed to the best of our knowledge while being perfectly valid on symmetry and physical considerations.

Furthermore, the $\mathcal{K}$ coefficient of two different materials, namely $PbZrO_3$ and $CaTiO_3$ was calculated using first-principles calculations. Both materials possesses a similar tolerance factor introduced by Goldschmidt [96]. For that, we calculated the change of the forces on atoms A emerging as a result of the change of the amplitudes of oxygen octahedra tiltings illustrated in Figure 3.2(b). These configurations are associated with the $\frac{2\pi}{a_{lat}}(\frac{1}{4}, \frac{1}{4}, 0)$ k point. Equation (3.1) tells us that this force depends linearly on the change of the amplitude of tilting, with the resultant slope being directly proportional to the K coefficient. Our first-principles calculations confirm such linearity and yield values for K in $PbZrO_3$ and $CaTiO_3$ equal to 0.013 and 0.011 in atomic units, respectively. The value of $\mathcal{K}$ coefficient is similar, but $CaTiO_3$ does not adopt the the PZO tilting pattern. This can be understood from first-principles as follows: the computed energy decreases in $PbZrO_3$ with the increase of the amplitudes of the oxygen octahedral tiltings, but after some point it starts increasing. This is consistent with the stability of the "bare" tilting mode with k=$(\frac{1}{4}, \frac{1}{4}, 0)$ in PZO. In contrast to this, in $CaTiO_3$, this mode is unstable in favor of tilting with different k-vectors. To depict such features, Figure 3.7 display the $\kappa_-(\lambda)$ and $\kappa_+(\lambda)$ eigenvalues of Eqn. (3.13) for $H_{u\omega}$=54.8, and $E''_u(\lambda) = -192.5 - 2.5cos(\pi\lambda)$ and $E''_\omega(\lambda) = +100 + 300cos(\pi\lambda)$ along the Σ line. One can see that the resulting κ_- at $\lambda = \frac{1}{2}$ is away from the minimum of κ_- at $\lambda = \frac{1}{2}$ as compared

to Figure 3.5(b), which can be thought as representing the situation of $PbZrO_3$. As a results, one can say based on the investigated atomistic interactions that there is no realistic trilinear coupling between R_4^+, Σ_2, and S_4 which can make Pbam the ground state of $CaTiO_3$.

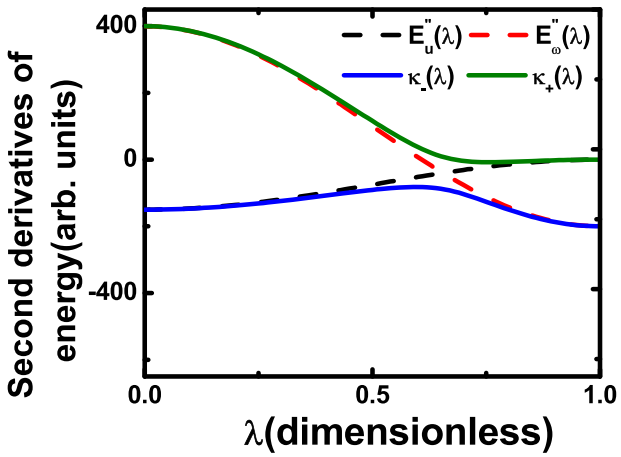

Figure 3.7: Dependencies of $E_u''(\lambda)$, $E_\omega''(\lambda)$, $\kappa_-(\lambda)$ and $\kappa_+(\lambda)$ along the Σ line for $H_{u\omega}$ = 54.8.

3.5 Conclusions

In summary, an elemental atomistic energy is investigated which naturally explains a variety of structurally complex phenomena in ABO_3 perovskites. This energy linearly couples polar distortions driven by A-site cations in collaborative way with O_6-rotational modes. Analytical derivations from this atomistic energy can be used to explain the existence and (in)stability in the first Brillouin zone of complex long-wave phonons. The investigated atomistic energy plays a crucial role in stabilizing antiferroelectric phases of $PbZrO_3$, $PbHfO_3$, $BiFeO_3$, (Bi,Nd)FeO_3, $NaNdO_3$ and $BiFe_{1/2}Sc_{1/2}O_3$. The newly-proposed couplings is applicable to perovskites in which the off-center shift of cations

and oxygen-octahedral rotational instabilities are present. It is possible to explain by the theory proposed the unusual tilting pattern recently discovered in $Nd_{1-x}Li_xTiO_3$ [89] as well as the large variety of antiferroelectric structures that are known to exist in Pb-based compounds (see, e.g., Ref. [97]). A structural determination of the *A*-site distortions and O_3-tiltings would be required, at the experimental level to confirm such a connection. The proposed theory can also naturally explain the occurrence of incommensurate phases in perovskites. A unified overview given in the present work brings together diversity of the mixed ferroelectric, antiferroelectric, antiferrodistortive (O_6-rotational) and incommensurate structures arising as a result of coupling of the corresponding structural modes. The development of the Landau type theory by presenting atomistic interactions in continuum limit seems to be also an important achievement.

The proposed mechanism drives structural instabilities that are hybrid in nature, in the sense that they combine (anti)polar and octahedra-rotational characteristics. In addition, this coupling tends to favor long-period distortions for wave vectors away from the center or boundary of the first Brillouin zone. In such cases, O_6 rotations is not perfect and the oxygen octahedra deform. Therefore in perovskites with relatively soft O_6 groups, the newly suggested coupling is most likely important. The examples discussed in this chapter indicate that the presence of relatively large *B*-cations in the perovskite structure favors this condition.

It is also noteworthy that the investigated interatomic couplings should be incorporated with the help of atomistic methods, for example with the help of the so-called effective Hamiltonian method [98, 99] (with, e.g., the $\mathcal{K}$ coefficient of Eqn. (3.1) being extracted from first-principles calculations)

to study, properties of antiferroelectrics and incommensurate systems, as a function of temperature, applied electric fields, epitaxial strains, etc. Furthermore, it is simple to derive a continuum (original) version of our coupling energy, as needed for the development of phenomenological Landau-Lifshitz theories. The results obtained here are published in Ref. [100].

Chapter 4

DYNAMICS OF ANTIFERROELECTRIC STRUCTURES

This section reports the results and analyses of atomistic simulations revealing and explaining the dynamics of antiferroelectric distortions in $BiFeO_3$ (BFO) bulk under hydrostatic pressure. Under high hydrostatic pressure, BFO is antiferroelectric [87]. The problem I want to resolve here is if BFO has an antiferroelectric soft mode or not. This is a fundamental problem. Actually, I found that the antiferroelectric mode does not soften itself on cooling, but rather it is improper, due to coupling with two other soft structural (tilting) modes. The following phase transition sequence is found on cooling from high temperature: the cubic paraelectric $Pm\bar{3}m$ state at high temperature, followed by an intermediate phase possessing long-range-ordered in-phase oxygen octahedral tiltings, and then the *Pnma* state that is known to possess antipolar cation displacement in addition to the in-phase and antiphase oxygen octahedral tiltings. In the paraelectric phase, I found the antipolar cation modes to have high frequency phonons that are independent of temperature. On the other hand, some phonons corresponding to oxygen octahedral tiltings are soft and decrease their frequency on cooling. Analyses of my data combined with an analytical model, which I will show below, reveal that the antiferroelectric mode in BFO under pressure originates from a dynamical mixing between pure antipolar cation phonons and fluctuations of oxygen octahedral tiltings, as a result of a specific trilinear energy in $P4/mbm$ and *Pnma* phases. The model developed and described below in detail can be easily applied to predict dynamics of antipolar cation motions for other possible structural paths bridging $Pm\bar{3}m$ and *Pnma* structural phases.

4.1 Background

This research aims to study the dynamics of antipolar distortions in ABO_3 perovskite resulting from the trilinear energetic couplings that have been recently discovered and intensively investigated [1, 2, 3, 4, 5, 6, 7]. Some of the trilinear energetic couplings result in the formation of an electrical polarization P, because of coupling with a rotation pattern that is a combination of two non polar lattice modes having different symmetries [1, 2, 3, 4, 5, 6, 7]. Trilinear energetic couplings can also arise in compounds possessing antipolar cation distortions via their coupling with in-phase and antiphase oxygen octahedral tiltings [85]. Antipolar systems are important compounds on their own. For instance, the *Pnma* state in ABO_3 perovskites is known to possess antipolar motion of its A cations, and recent studies found that it may adopt the double polarization vs electric field hysteresis loop in some materials [101, 102], which characterize antiferroelectrics [103], suggesting that *Pnma* states in some perovskites can hold promise towards the design of energy storage devices with high energy densities and efficiencies [104, 105, 106, 107, 108, 109, 110]. Interestingly, all the above-mentioned works on the trilinear energetic coupling have investigated static properties and very little is known about dynamical properties of perovskites exhibiting the trilinear energetic couplings. For instance, one may wonder how the antipolar phonon frequencies behave with temperature when the material exhibits phase transitions leading to an antipolar states having antiphase and in-phase oxygen octahedral tiltings. Are they soft in any phase, including the one(s) for which the antipolar cation motions have not adopted yet a long-range order? Can they mix with phonons associated with fluctuations of oxygen octahedral tiltings in any of these phases because of this trilinear energetic coupling, or rather does this hypothetical mixing only occur when in-phase and/or antiphase tiltings have condensed? The answers to all above aforementioned

questions are provided in this work by focusing on a specific material, namely (BFO) under pressure since this system is known to adopt a *Pnma* structure at high enough pressure, that possesses a trilinear coupling between antiferroelectricity and two oxygen tilts [45, 46, 47].

4.2 Methods

The effective Hamiltonian approach as mentioned in chapter 2 ([111, 112, 113, 114]) is used to investigate properties of BFO at finite temperatures and under hydrostatic pressure. The degrees of freedoms of this Hamiltonian are:

(i) the local soft mode $\mathbf{u_i}$ centered on the Bi sites (such centering allows, e.g., to reproduce the Bi-driven antiferroelectricity (AFE) associated with the *Pnma* phase of BFO [114]); (ii) η is the homogenous strain tensor; (iii) the pseudo-vector $\omega_\mathbf{i}$, which is centered on Fe ions and characterizes oxygen octahedral tiltings (also known as antiferrodistortive (AFD) distortions) in unit cell i [80]; (iv) the magnetic dipole moment m_i, which is Fe-centered too and whose magnitude is equal to $4\mu_B$, as consistent with first principles [81] and measurements [82]; and (v) the inhomogeneous strain characterized by dimensionless variable v_i [115]. The total energy is the sum of the following three terms:

$$E_{total} = E_1(\{u_i\},\{\eta\},\{v_i\}) + E_2(\{m_i\},\{u_i\},\{\eta\},\{v_i\},\{\omega_i\}) + E_3(\{u_i\},\{\eta\},\{v_i\},\{\omega_i\}) \quad , \quad (4.1)$$

E_1 represents the energy associated with the local modes, elastic strain interactions, and coupling between the local modes and strain; E_2 ensembles the energies correlated with the magnetic degrees of freedom and their couplings with the local modes, strains, and AFD distortions; and E_3 describes the energetics involving the AFD interactions and their couplings with the local modes and strains. Analytical expressions for E_1 and E_2 are provided in Ref. [115] and Ref. [111], respectively. Note

that the last term of E_3 is precisely the trilinear energy coupling between the local mode u centered on Bi sites and two AFD modes centered on Fe sites. The analytical expression for E_3 is given in Ref. [114] and is as follows:

$$\begin{aligned} E_3(\{u_i\},\{\eta\},\{v_i\},\{\omega_i\}) = & \sum_i [\kappa_A \omega_i^2 + \alpha_A \omega_i^4 + \gamma_A(\omega_{ix}^2\omega_{iy}^2 + \omega_{iy}^2\omega_{iz}^2 + \omega_{ix}^2\omega_{iz}^2)] \\ & + \sum_{ij}\sum_{\alpha\beta} K_{ij\alpha\beta}\omega_{i\alpha}\omega_{j\beta} + \sum_i \sum_\alpha K'\omega_{i,\alpha}^3\,(\omega_{i+\alpha,\alpha} + \omega_{i-\alpha,\alpha}) \\ & + \sum_i \sum_{\alpha\beta} C_{l\alpha\beta}\eta_l(i)\omega_{i\alpha}\omega_{i\beta} \\ & + \sum_{i,j}\sum_{\alpha,\beta} \mathrm{D}_{ij,\alpha\beta}u_{j,\alpha}\omega_{i,\alpha}\omega_{i,\beta} + \sum_{i,j}\sum_{\alpha\beta\gamma\delta} E_{\alpha\beta\gamma\delta}\omega_{i\alpha}\omega_{j\beta}u_{j\gamma}u_{i\delta} \end{aligned} \tag{4.2}$$

where the sum over i runs over all Fe-sites, and α and β are Cartesian components along the x-, y-, and z-axes coinciding with the pseudocubic [100], [010], and [001] directions respectively. Moreover, $\eta_l\,(i)$ is the l-th component of the total strain (in Voigt notation), including the homogeneous and inhomogeneous strain, at site i. The first three energies of Eq. (4.2) were proposed and/or used in Refs.[111, 112, 113, 114] and characterize the onsite interactions of the AFD distortions. The fourth and fifth energies represent AFD short-range interactions and were provided in Ref. [112] and Ref. [114], respectively. Note that, in this fifth energy, $\omega_{i+\alpha,\alpha}$ is the α-component of the AFD mode at the site shifted from the Fe site i to its nearest Fe neighbor along the axis α. The sixth energy describes the coupling between oxygen octahedral tiltings and strains. The seventh energy was introduced in Ref.[114] and represents an anharmonic (trilinear) interaction energy between the local mode u centered on a Bi site and two AFD distortions centered on Fe sites. Finally, the eight energy term of Eqn. (4.2) characterizes bi-quadratic interactions between oxygen octahedral tiltings and local modes, as given in Ref. [112].

We first employ this effective Hamiltonian to perform Monte-Carlo (MC) simulations, as in Ref. [114], in order to compute finite-temperature properties of BFO bulk under a simulated hydrostatic pressure of about 8.2GPa in 12 x 12 x 12 supercells using 40,000 MC sweeps [116]. We then perform Molecular dynamics (MD) calculations by using 4 x 10^5 MD steps with a time step of 0.5fs as similar to what was done in Ref. [117], except that the effective Hamiltonian used here has local modes that are centered on Bi ions (and not on Fe ions like in Ref. [117]). As a result, the fifth and seventh terms of Equation (4.2) are presently incorporated into the dynamics of BFO. During these latter MD calculations, we computed different frequency-dependent responses related to different order parameters, as described by using the general formula [118, 119, 120]

$$\chi^{AA}_{\alpha\beta}(\nu) = \frac{1}{Vk_BT}\left[< A_\alpha(t)A_\beta(t) > +i2\pi\nu \int_0^\infty dt\ e^{i2\pi\nu t} < A_\alpha(t)A_\beta(0) >\right] \tag{4.3}$$

where ν is the frequency, α and β define Cartesian components and V is the volume of the chosen supercell. *A(t)* is an order parameter at time t, and " <..>" indicates thermal average.

We focused on the following physical quantities: (i) The order parameter will be chosen to be $\mathbf{u_X}$ vector characterizing the X_5^+ antiferroelectric Bi displacements at the X-point of the Brillouin zone, and is given by $\mathbf{u_X} = \frac{1}{N}\sum_i u_i\,(-1)^{n_z(i)}$, where N is the number of the Fe ions in the supercell and where $n_z\,(i)$ is an integer locating the cell i along the z-axis[80], (ii) the M_3^+ mode that characterizes in-phase oxygen octahedral tilting around Fe sites, and is quantifies by $\omega_\mathbf{M} = \frac{1}{N}\sum_i \omega_i\,(-1)^{n_x(i)+n_y(i)}$, and (iii) the R_4^+ mode representing antiphase tilting of the oxygen octahedral and for which the corresponding order parameter is $\omega_\mathbf{R} = \frac{1}{N}\sum_i \omega_i\,(-1)^{n_x(i)+n_y(i)+n_z(i)}$, where the sum run over the N site and $n_x\,(i)$, $n_y\,(i)$, and $n_z\,(i)$ are integers locating the cell i[80]. Here ω_i is an Fe-centered pseudo-vector that characterizes the oxygen octahedral tilting in unit cell i. We decided to study

these three particular modes because their order parameters are all coupled via a trilinear energy of the form [8]:

$$E_{trilinear} = D(u_{X,x}\omega_{R,x}\omega_{M,z} + u_{X,y}\omega_{R,y}\omega_{M,z}) \tag{4.4}$$

where D is a coefficient characterizing the strength of the interaction and the second subscript indicated the physical quantities involved refers backs to the corresponding Cartesian component of $\mathbf{u_X}$, $\omega_\mathbf{R}$ and $\omega_\mathbf{M}$.

Interestingly, $\chi^{AA}_{\alpha\beta}(\nu)$ can be considered to be a complex "susceptibility" related to order parameter A, as the response of A is related to its conjugate field. Such "susceptibility" is not measurable (unlike the dielectric susceptibility) when A is chosen to be $\mathbf{u_X}$, $\omega_\mathbf{R}$ or $\omega_\mathbf{M}$ (because their conjugate fields are staggered fields). However, the peaks of the imaginary part of the susceptibilities associated with $\mathbf{u_X}$, $\omega_\mathbf{R}$, and $\omega_\mathbf{M}$, respectively, occur at the natural frequencies of phonons associated with antipolar motions, antiphase tiltings, and in-phase tiltings, respectively. Hence computing the $\chi^{AA}_{\alpha\beta}(\nu)$ responses will give the natural phonon frequencies which may be experimentally obtained by hyper Raman scattering techniques [121].

The computed responses of $\chi^{AA}_{\alpha\beta}(\nu)$ susceptibilities are fitted to *sum* of Damped Harmonic Oscillators (DHO), given by the formula:

$$\chi = \frac{S(2\pi\nu)^2}{(2\pi\nu_r)^2 - (2\pi\nu)^2 - 2i\pi\nu\gamma} \tag{4.5}$$

where ν_r , γ, and S are the resonant frequency, damping constant, and oscillator strength, correspondingly. Note that the number of DHOs involved in this summation precisely corresponds to the number of the peaks found in the MD simulations of $\chi^{AA}_{\alpha\beta}(\nu)$.

4.3 Results

Figure 4.1 displays the temperature dependency of $\mathbf{u_X}$, $\omega_\mathbf{R}$, and $\omega_\mathbf{M}$, when BFO is cooled under hydrostatic pressure from 1600K to 900K through steps of 20K. The $\mathbf{u_X}$, $\omega_\mathbf{R}$, and $\omega_\mathbf{M}$ all vanishing above 1280K, which is representative of the cubic paraelectric $Pm\bar{3}m$ phase. From 1280K to 1240K, the z-component of $\omega_\mathbf{M}$ becomes finite, while $\mathbf{u_X}$ and $\omega_\mathbf{R}$ remain null, and BFO is predicted to adopt the $P4/mbm$ ground state for this temperature range. On further cooling, the x- and y-components of $\mathbf{u_X}$ and $\omega_\mathbf{R}$ becoming finite, while the z-component of $\omega_\mathbf{M}$ continues to be non-null and enhanced when the temperature is reduced below 1240K which characterized the $Pnma$ phase, for which $\mathbf{u_X}$, $\omega_\mathbf{R}$ or $\omega_\mathbf{M}$ exist and lie along the pseudo-cubic [110], [110] and [001] directions respectively, below this latter critical temperature. Let us now see the effect of the phase transitions on the dynamics of order parameters $\mathbf{u_X}$, $\omega_\mathbf{R}$, and $\omega_\mathbf{M}$.

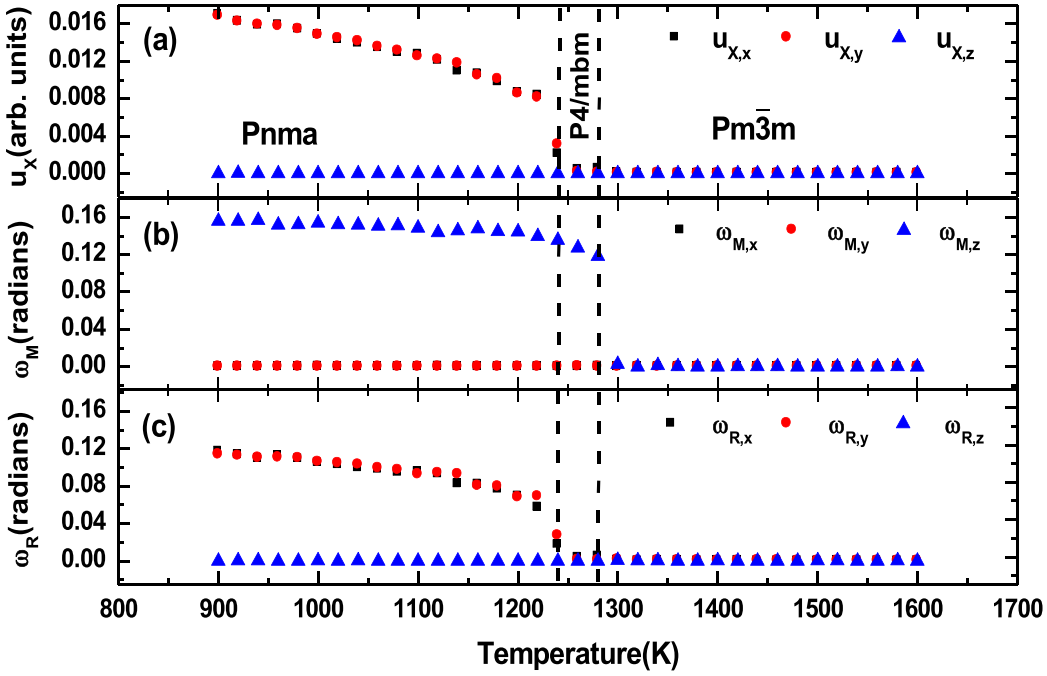

Figure 4.1: Predicted temperature dependence of the (a) antipolar $\mathbf{u_X}$ vector, (b) in-phase tilting $\omega_\mathbf{M}$ pseudo vector, and (c) antiphase tilting $\omega_\mathbf{R}$ pseudo-vector in our BFO system subject to hydrostatic pressure. The dashed vertical lines delimit three different structural phases.

Order parameter $\mathbf{u_X}$:

Figure 4.2(a, b, c) display the imaginary part of $\chi_{xx}^{AA}(\nu)$, $\chi_{yy}^{AA}(\nu)$ and $\chi_{zz}^{AA}(\nu)$ respectively, at a temperature of 1560K when $AA = \mathbf{u_X}$. At this temperature, BFO is within the $Pm\bar{3}m$ state. Further, Fig. 4.3(a, b, c) report similar data at 1260K, that is now for the $P4/mbm$ phase and Fig. 4.4(a, b, c) show these susceptibilities of the AFE degree of freedom at 1040K, i.e. inside the *Pnma* state. One can see different narrow peaks at these temperatures for $\mathbf{u_X}$.

At a temperature of $1560K$, one peak occurs at about 105 cm^{-1} in both the xx and yy components of the susceptibility, which is associated with the AFE phonon and they are doubly degenerate and are associated with oscillations of $\mathbf{u_X}$ along the x or y-direction. The frequency of oscillations will be denoted as $\nu_{X_5^+,x,Pm\bar{3}m}$, adopting the convention that the three subscripts refer to the type of mode, the direction of the fluctuations of its order parameter and the macroscopic phase, respectively. The

zz component of the susceptibility shown in Fig. 4.2(c) has also another peak at a frequency that is close to 166 cm^{-1} and that will be coined $\nu_{X_5^+,z,Pm\bar{3}m}$ (since it is associated with oscillations of $\mathbf{u_X}$ along the z axis).

Next, Fig. 4.3(a, b, c) displays the data at a temperature of $\underline{1260K}$, the xx and yy components of the AFE susceptibility possesses two peaks at frequencies of about 15 and 120 cm^{-1} and they are denotes as $\nu_{X_5^+,x,P4/mbm,LF}$ and $\nu_{X_5^+,x,P4/mbm,HF}$ respectively, where "LF" and "HF" stand for low-frequency and high-frequency, respectively. The zz component (see Fig. 4.3(c)) possess a single peak at about 172 cm^{-1}, and the frequency is denoted as $\nu_{X_5^+,z,P4/mbm}$.

At a temperature of $\underline{1040K}$, as shown in Fig. 4.4(a, b, c), the xx and yy components of the AFE susceptibilities shows increase of the number of peaks in the *Pnma* state. The three peaks are centered around 80, 115 and 144 cm^{-1} and are denoted as $\nu_{X_5^+,x,Pnma,LF}$, $\nu_{X_5^+,x,Pnma,MF}$, and $\nu_{X_5^+,x,Pnma,HF}$, respectively. Here "MF" standing for "middle frequency". $\nu_{X_5^+,x,Pnma,LF}$ and $\nu_{X_5^+,x,Pnma,MF}$ when computed in different basis, which is not shown here, corresponds to the oscillations of antipolar motion along the direction of spontaneous long-range-ordered $\mathbf{u_X}$ in the Pnma state, while $\nu_{X_5^+,x,Pnma,HF}$ is associated with the fluctuation of antipolar motions along the in-plane direction i.e perpendicular to this spontaneous $\mathbf{u_X}$. The zz component of this AFE susceptibility (see Fig. 4.4(c)) remains singly peaked at a frequency of about 175 cm^{-1} and is denoted as $\nu_{X_5^+,z,Pnma}$. Here, $\nu_{X_5^+,z,Pnma}$, $\nu_{X_5^+,z,P4/mbm}$, and $\nu_{X_5^+,z,Pm\bar{3}m}$ can be considered to be continuation of each other within the phase transition sequence since they are all associated with fluctuations of antipolar motions along the z-axis.

There is an increase in the number of peaks occurring in the xx and yy susceptibilities associated with the X_5^+ mode when passing phase transitions. It is not straightforward to understand the *microscopic* origin of the increase in the number of peaks. The group theory can predict the

increase of the number of phonon modes when changing structural phases, but it does not provide the microscopic origin of such increase. For instance, one may wonder what atomistic feature is responsible for the occurrence of two peaks of these susceptibilities in the $P4/mbm$ phase (rather than a single one as in $Pm\bar{3}m$) while the AFE vector still does not adopt any long-range ordering there. We will come back to this point later on.

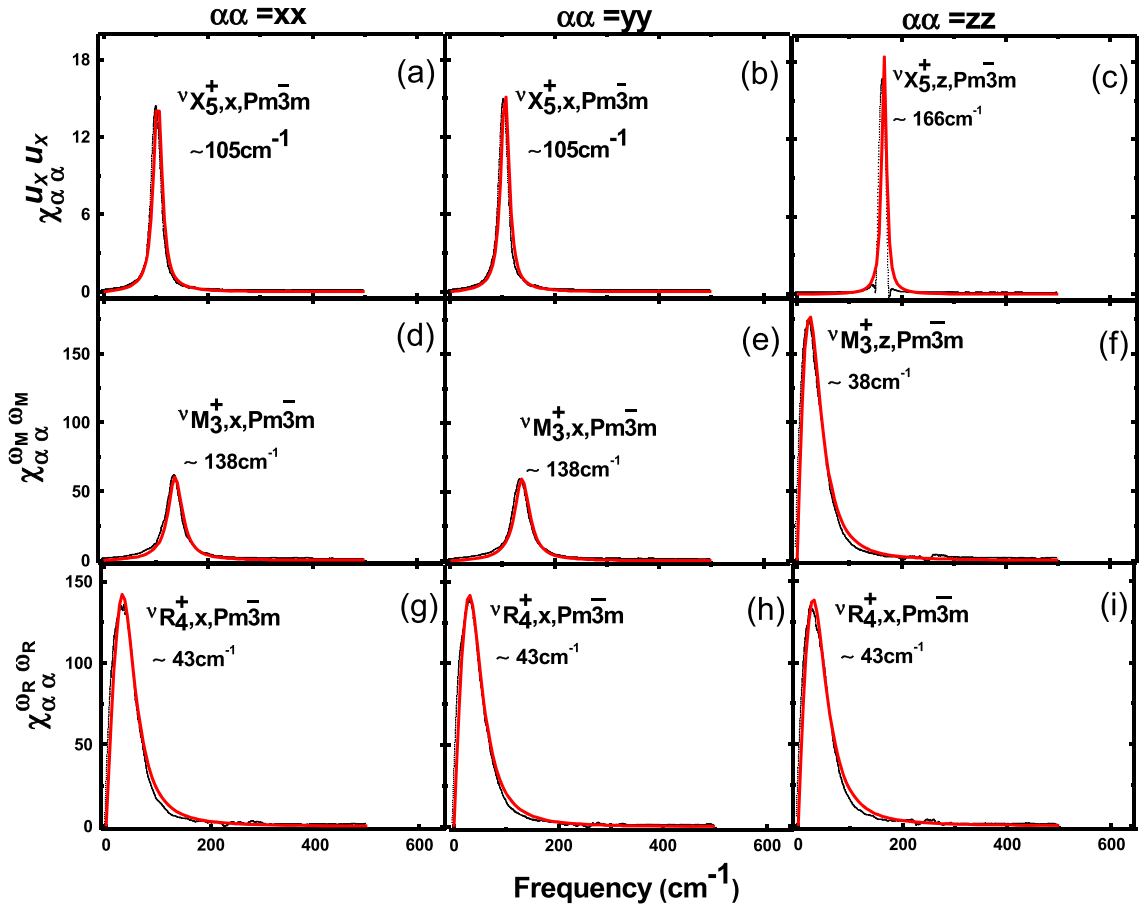

Figure 4.2: Frequency dependence of the imaginary part of the $\chi_{\alpha\alpha}^{AA}(\nu)$ "susceptibilities" in our BFO system subject to hydrostatic pressure (a-c) for A= $\mathbf{u_X}$, (d-f) for $\omega_\mathbf{M}$, and (g-i) for $\omega_\mathbf{R}$ at a temperature of 1560K that is, for the $Pm\bar{3}m$ cubic state. For each physical quantity A, the left, middle and right panels correspond to α=x, y or z coordinate, respectively. The black line displays the MD data while the red line represents their fit by DHOs

Order parameter $\omega_{\mathbf{M}}$:

Figure 4.2(d, e, f) display the imaginary part of $\chi_{xx}^{AA}(\nu)$, $\chi_{yy}^{AA}(\nu)$ and $\chi_{zz}^{AA}(\nu)$ respectively, when A=$\omega_{\mathbf{M}}$ for a temperature of 1560K, i.e. within the cubic Pm$\bar{3}$m state. Fig. 4.3(d, e, f) and Fig. 4.4(d, e,f) provide similar data for the susceptibility associated with the in-phase tiltings at 1260K and 1040K, respectively, that is for $P4/mbm$ and $Pnma$ states.

At a temperature of $1560K$, the xx and yy components of the susceptibilities of the in-phase octahedral tilting M_3^+ mode exhibits a single peak in the cubic state and is about 138 cm^{-1} and is denoted as $\nu_{M_3^+,x,Pm\bar{3}m}$. It is doubly degenerated as the peak appears at the same frequency and is associated with oscillations of $\omega_{\mathbf{M}}$ along the x or y-axes. The zz component of the susceptibility associated with $\omega_{\mathbf{M}}$ has only one peak at around 38 cm^{-1} and which corresponds to fluctuations of $\omega_{\mathbf{M}}$ along the z-axis.

Let us now pay at a temperature of $1260K$ which is $P4/mbm$ state. The xx and yy components of the susceptibilities of the antiphase tiltings have one peak at about 140 cm^{-1} and is denoted as $\nu_{M_3^+,x,Pm\bar{3}m}$ (see Figure 4.3(d,e)) and is associated with oscillations of $\omega_{\mathbf{M}}$ along the x or y-axes and it is doubly degenerated. The zz components of the susceptibility continue to have a single peak in the intermediate $P4/mbm$ state and the frequency is close to 90 cm^{-1} and corresponds to fluctuations of $\omega_{\mathbf{M}}$ along the z-axis. This frequency is denoted as $\nu_{M_3^+,z,Pm\bar{3}m}$. $\nu_{M_3^+,z,Pm\bar{3}m}$ is much higher then $\nu_{M_3^+,x,Pm\bar{3}m}$.

But suddenly there appears three peaks in the $Pnma$ phase at $1040K$ as evidenced in Fig. 4.4(f). Very interestingly, these three peaks have the same resonant frequencies as the aforementioned antipolar $\nu_{X_5^+,x,Pnma,LF}$, $\nu_{X_5^+,x,Pnma,MF}$, and $\nu_{X_5^+,x,Pnma,HF}$ frequencies.

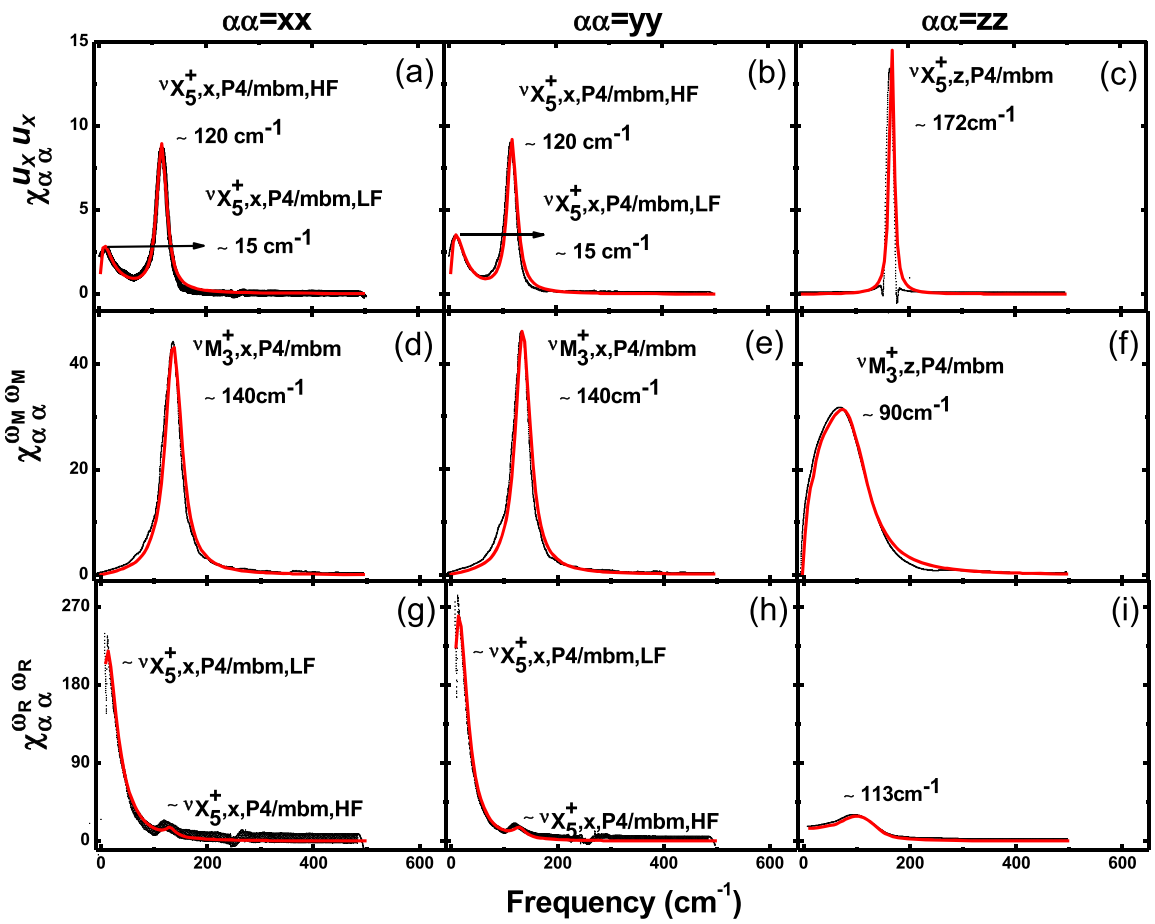

Figure 4.3: Same as Fig. 4.2 but for a temperature of 1260K (which corresponds to the $P4/mbm$ state).

Order parameter $\omega_{\mathbf{R}}$:

Figure 4.2(g, h, i) display the imaginary part of $\chi^{AA}_{xx}(\nu)$, $\chi^{AA}_{yy}(\nu)$ and $\chi^{AA}_{zz}(\nu)$ respectively, when A=$\omega_{\mathbf{R}}$ at a temperature of 1560K that is for $Pnma$. Fig. 4.3(g, h, i) and Fig. 4.4(g,h,i) provide similar data for the susceptibility associated with the antiphase tilting at 1260K and 1040K, respectively, that is for $P4/mbm$ and $Pnma$ states.

At $1560K$ temperature, as shown in Fig. 4.2(g, h, i), the antiphase octahedral tilting R_4^+ mode has a single peak in either the xx, yy, or zz susceptibility with the corresponding natural frequency being identical between the different components of this susceptibility and being coined $\nu_{R_4^+,x,Pm\bar{3}m}$. It is about 43 cm^{-1}, is therefore triply degenerate and corresponds to fluctuations of ω_R along the

x, y, or z axes.

In intermediate $P4/mbm$ state Figure 4.3(g, h, i) display the results of susceptibilities at $\underline{1260K}$. The R_4^+ mode has now two peaks each for the xx and yy susceptibilities in $P4/mbm$, with the corresponding frequencies being close to the aforementioned antipolar frequencies and are denoted as $\nu_{X_5^+,x,P4/mbm,LF}$ and $\nu_{X_5^+,x,P4/mbm,HF}$. Such facts strongly hint towards a very specific *dynamical* coupling between the fluctuations of the x- and y-components of $\mathbf{u_X}$ and $\omega_\mathbf{R}$ within the $P4/mbm$ state. Such hint is reinforced when realizing that $\nu_{X_5^+,x,P4/mbm,LF}$ is the weakest peak of $\chi_{xx}^{AA}(\nu)$ for A=$\mathbf{u_X}$ (see Fig. 4.3(a)) while it is the strongest peak for the xx-component of the susceptibility of $\omega_\mathbf{R}$ (cf Fig. 4.3(g)), while the reverse behavior is seen for $\nu_{X_5^+,x,P4/mbm,HF}$. This mixing also explains why $\nu_{X_5^+,x-y,Pnma,LF}$ is soft within the $P4/mbm$ state, since the antiphase octahedral tilting is already very soft in the cubic state (see the temperature behavior of $\nu_{R_4^+,x,Pm\bar{3}m}$ in Fig. 4.5(b)), and why a phase transition from $P4/mbm$ to $Pnma$ occurs at around 1240K, below which both the AFE and antiphase tiltings adopt long-range order.

At $\underline{1040K}$ temperature, Fig. 4.4(g, h, i) displays the susceptibility associated with the antiphase tiltings for Pnma state. We see three peaks and the resonant frequencies are same as antipolar $\nu_{X_5^+,x,Pnma,LF}$, $\nu_{X_5^+,x,Pnma,MF}$, and $\nu_{X_5^+,x,Pnma,HF}$ frequencies. Such mixings of antipolar and AFD modes in the Pnma state, all involving in-plane fluctuations of both $\mathbf{u_X}$ and $\omega_\mathbf{R}$ and *out-of-plane* oscillations of $\omega_\mathbf{M}$. This mixing is consistent as the magnitude of the peaks is maximum for susceptibilities for A=$\omega_\mathbf{R}$, A=$\omega_\mathbf{M}$, and A=$\mathbf{u_X}$ occurs at three different frequencies namely $\nu_{X_5^+,x,Pnma,LF}$ (see Fig. 4.4(g)), $\nu_{X_5^+,x,Pnma,MF}$ (see Fig. 4.4(f)), and $\nu_{X_5^+,x,Pnma,HF}$ (see Fig. 4.4(a)), respectively. This mixing also explains why $\nu_{X_5^+,x,Pnma,LF}$ soften when approaching the Pnma—to—P4/mbm phase transition since we demonstrated that oxygen octahedral tiltings are very soft above such transition.

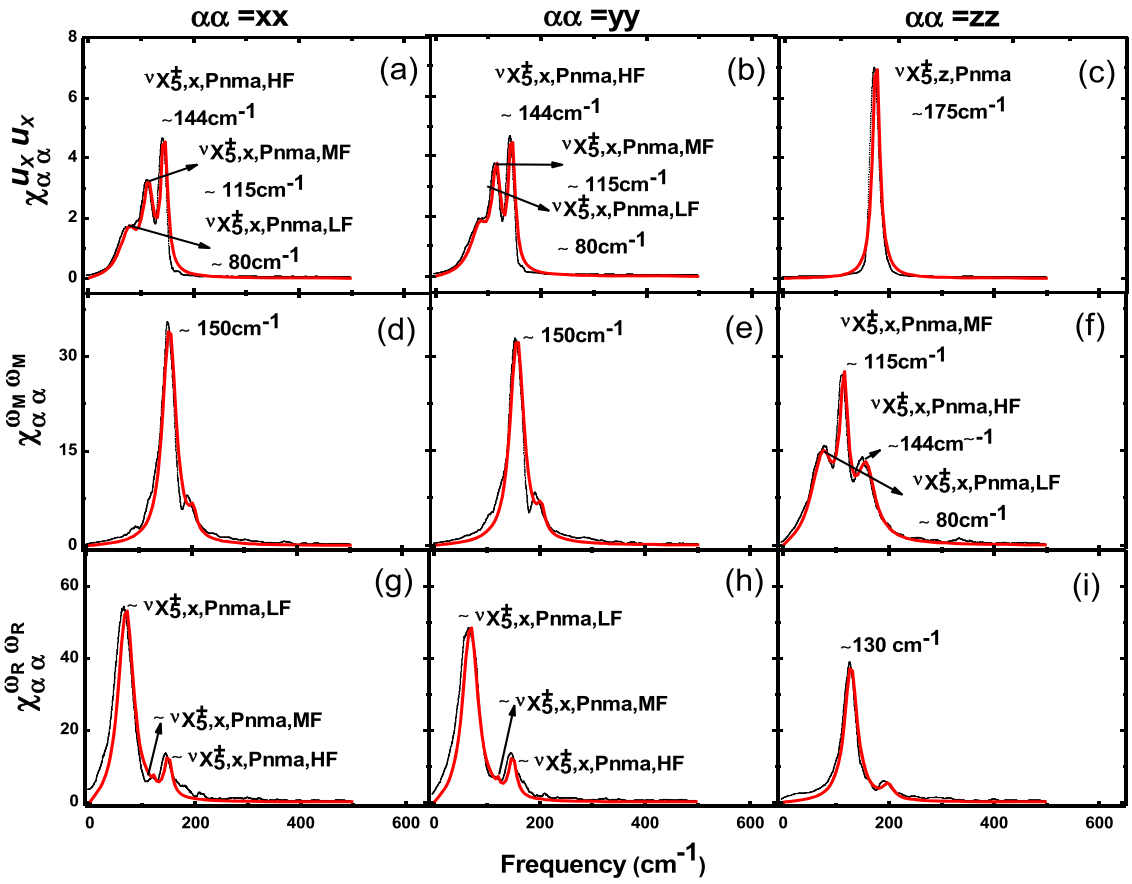

Figure 4.4: Same as Fig. 4.2 but for a temperature of 1040K (which corresponds to the *Pnma* state).

4.3.1 Temperature dependence of resonant natural frequencies

Figure 4.5(a, b) shows the temperature dependencies of all aforementioned resonant frequencies associated with the dynamics of Bi motions within the X_5^+ antipolar mode. Several important results can be inferred from these figures as follows:

(1) Both $\nu_{X_5^+,z,Pm\bar{3}m}$ and $\nu_{X_5^+,x,Pm\bar{3}m}$ are nearly independent on the temperature within the entire stability region of the cubic state. As a result, neither of these two frequencies softens when approaching the $Pm\bar{3}m - to - P4/mbm$ transition from *above*. This implies that this transition is dynamically driven by a physical quantity that has nothing to do with antiferroelectricity – as consistent with the sole condensation of the z-component of $\omega_{\mathbf{M}}$ below 1280K (see Fig. 4.1).

(2) One specific antipolar mode, namely $\nu_{X_5^+,x,P4/mbm,LF}$, is very soft within the entire $P4/mbm$ state.

(3) $\nu_{X_5^+,x,Pnma,LF}$ significantly softens too when heating the system within the $Pnma$ state towards the $Pnma - to - P4/mbm$ transition.

(4) Fig. 4.5(b) reports two frequencies, namely $\nu_{R_4^+,x,Pm\bar{3}m}$ and $\nu_{M_3^+,z,Pm\bar{3}m}$ in the $Pm\bar{3}m$ cubic state. These two frequencies soften when approaching the critical temperature of 1280K. $\nu_{M_3^+,z,Pm\bar{3}m}$ is always smaller than $\nu_{R_4^+,x,Pm\bar{3}m}$ for any temperature in the cubic state. Such features are responsible for the occurrence of long-range-ordered in-phase tilting below 1280K (see Fig. 4.1), and therefore to the transition from $Pm\bar{3}m - to - P4/mbm$.

(5) It is interesting to realize that $\nu_{M_3^+,z,Pm\bar{3}m}$ is different from $\nu_{R_4^+,x,Pm\bar{3}m}$ and $\omega_{\mathbf{M}}$ condenses at a slightly higher temperature than $\omega_{\mathbf{R}}$ (see Fig. 4.1). This implies that phenomenologies having the same harmonic coefficient in front of the in-phase and antiphase tiltings (see Ref(3)) has to be revised and generalized.

(6) The R_4^+ and M_3^+ modes are slightly harder when the temperature is decreased in the $P4/mbm$ state and R_4^+ and X_5^+ become strongly correlated. This correlation results in the emergence of an X_5^+ mode that is associated with the frequency denoted as $\nu_{X_5^+,x,Pnma,LF}$.

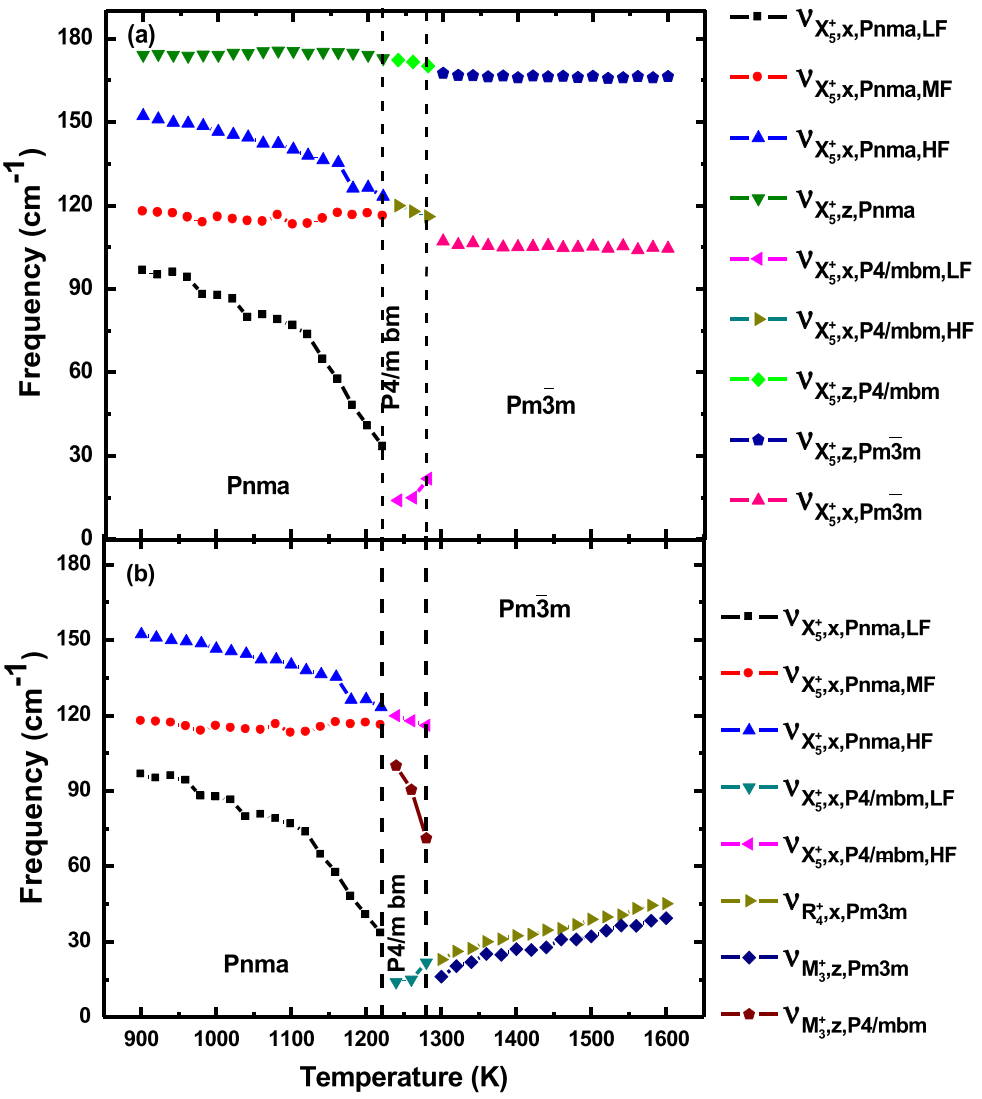

Figure 4.5: Temperature dependence of natural frequencies of some phonon modes (a) that have antipolar character and (b) oxygen octahedral tilting character. The vertical dashed lines delimit the different phases obtained in the calculations for our BFO system subject to hydrostatic pressure.

Let us now try to understand why $\mathbf{u_X}$ and $\omega_\mathbf{R}$ can be dynamically coupled in the $P4/mbm$ state while the fluctuations of $\mathbf{u_X}$, $\omega_\mathbf{R}$ and $\omega_\mathbf{M}$ can all dynamically mix in the *Pnma* state, and that no such dynamical couplings exist in the cubic phase. Let us also explain why only very specific components of these three order parameters dynamically couple to each other in the $P4/mbm$ and *Pnma* phases.

4.4 Discussion

For that, let us first write the equation of motion associated with the x or y component of $\mathbf{u_X}$:

$$m^X \frac{d^2 u_{X,\alpha}}{dt^2} = -\frac{dE_{total}}{du_{X,\alpha}} + \gamma_\alpha^X \frac{du_{X,\alpha}}{dt} \tag{4.6}$$

Where $\alpha = x$ or y; m^X is the mass of this antipolar mode; γ_α^X is the damping constant; E_{total} is the total energy provided our effective Hamiltonian; and t is the time. In the harmonic approximation and using the energies of Eqns (4.1), (4.2) and (4.4), Eqn. (4.6) becomes:

$$\sum_\beta \left[\left(2\pi\nu_\alpha^X\right)^2 - (2\pi\nu)^2 - 2i\Gamma_\alpha^X \pi\nu + B_{X_\alpha M_\beta}\omega_{M,\beta}^2 + B_{X_\alpha R_\beta}\omega_{R,\beta}^2 \right] u_{X,\alpha} = -D\omega_{M,z}\omega_{R,\alpha} \tag{4.7}$$

Here ν_α^X is the natural frequency of the antipolar mode, $\Gamma_\alpha^X = \gamma_\alpha^X / m^X$, D is the *trilinear* coupling strength between $\mathbf{u_X}$, $\omega_\mathbf{R}$ and $\omega_\mathbf{M}$, β runs over the Cartesian components, and B are the parameters involved in the biquadratic coupling between u_X^2 and ω_M^2 and between u_X^2 and ω_R^2.

Neglecting fluctuations of $\omega_{M,\beta}$ and $\omega_{R,\beta}$ with time on the left-hand site of Eqn. (4.7) yields

$$\sum_\beta \left[\left(2\pi\nu_\alpha^X\right)^2 - (2\pi\nu)^2 - 2i\Gamma_\alpha^X \pi\nu + B_{X\alpha M_\beta} \left\langle \omega_{M,\beta}^2 \right\rangle + B_{X_\alpha R_\beta} \left\langle \omega_{R,\beta}^2 \right\rangle \right] u_{X,\alpha} = -D\omega_{M,z}\omega_{R,\alpha} \tag{4.8}$$

where the "$<\ldots>$" symbol refers to spontaneous values. Note that the existence of $<\omega_{M,\beta}^2>$ and $<\omega_{R,\beta}^2>$ on the left-hand side of Eq. (4.8) implies that the resonant frequencies of the AFE modes are naturally *quantitatively* affected by the condensation of oxygen octahedral tiltings because of the aforementioned biquadratic couplings.

Introducing now the time fluctuations of $\omega_{M,z}$ and $\omega_{R,\alpha}$ on the right hand-side of Eqn. (4.8)

gives:

$$\sum_{\beta}\left[\left(2\pi\nu_{\alpha}^{X}\right)^{2}-(2\pi\nu)^{2}-2i\Gamma_{\alpha}^{X}\pi\nu+B_{X_{\alpha}M_{\beta}}\left\langle\omega_{M,\beta}^{2}\right\rangle+B_{X_{\alpha}R_{\beta}}\left\langle\omega_{R,\beta}^{2}\right\rangle\right]u_{X,\alpha}= \\ -D\left\langle\omega_{M,z}\right\rangle\left\langle\omega_{R,\alpha}\right\rangle-D\left\langle\omega_{R,\alpha}\right\rangle\delta\omega_{M,z}-D\left\langle\omega_{M,z}\right\rangle\delta\omega_{R,\alpha} \tag{4.9}$$

for α=x or y, and where $\delta\omega_{M,z}$ and $\delta\omega_{R,\alpha}$ represent the fluctuations of $\omega_{M,z}$ and $\omega_{R,\alpha}$ with respect to their spontaneous $\left\langle\omega_{M,z}\right\rangle$ and $\left\langle\omega_{R,\alpha}\right\rangle$ values.

Interestingly, averaging over time of Eqn. (4.9) will give on the left-hand side a quantity that is directly proportional to $<u_{X,\alpha}>$ and on the right-hand side a quantity that is simply $-D\left\langle\omega_{M,z}\right\rangle\left\langle\omega_{R,\alpha}\right\rangle$ (since $\left\langle\delta\omega_{M,z}\right\rangle=\left\langle\delta\omega_{R,\alpha}\right\rangle=0$, by definition). As a result, the time-integration of Eqn. (4.9) explains why, in our simulations depicted in Fig. 4.1, $<u_{X,x}>$ and $<u_{X,y}>$ becomes finite only after both $\left\langle\omega_{M,z}\right\rangle$ and $\left\langle\omega_{R,\alpha}\right\rangle$ are nonzero.

Equation (4.9) helps us to understand the mechanism of dynamical mixing as follows:
(1) the oscillations of the x and y components of $\mathbf{u_X}$ couple with the fluctuations of the z-component of $\omega_{\mathbf{M}}$ and with the fluctuations of the x and y components of $\omega_{\mathbf{R}}$ in the *Pnma* state, due to the last two terms on its right-hand side. Because of dynamical mixing, there exist three peaks in each of the $\mathbf{u_X}$, $\omega_{\mathbf{M}}$, and $\omega_{\mathbf{R}}$ (see Figs. 4.4(a), 4.4(f), and 4.4(g)). These three peaks originate form the trilinear energy coupling since the D constant is involved in these last two terms.
(2) In the cubic state, there is no dynamical mixing as $<\omega_{R,x}>$, $<\omega_{R,y}>$ and $<\omega_{M,z}>$ are zero.
(3) In $P4/mbm$ state, there are two different kinds of dynamical mixing. (a) the x-component and y components of $\mathbf{u_X}$ dynamically couples to the fluctuations of the z-component of $\omega_{\mathbf{M}}$ as soon as $<\omega_{R,x}>$ and $<\omega_{R,y}>$ are non-zero; and (b) the x and y components of $\mathbf{u_X}$ dynamically couples to the oscillations of the x and y-components of $\omega_{\mathbf{R}}$ when $<\omega_{M,z}>$ adopts a finite spontaneous value. Hence, the last two terms of Eqn. (4.9) explain the mixing between AFE and antiphase

tilting modes in the $P4/mbm$ state, even in absences of the long-range ordered of $\mathbf{u_X}$ and $\omega_\mathbf{R}$. In that case, item (b) is valid, and therefore it explains why only two peaks can be in Fig. 4.3(a) and 4.3(g). In that situation, what was denoted as $\nu_{X_5^+,x,Pm\bar{3}m}$ and $\nu_{R_4^+,x,Pm\bar{3}m}$ in the cubic phase (that are pure AFE and antiphase tilting modes, respectively) now interacts with each other in the $P4/mbm$ phase to give rise to the mixed $\nu_{X_5^+,x,P4/mbm,LF}$ and $\nu_{X_5^+,x,P4/mbm,HF}$ modes.

(4) Eqn. (4.9) as well as our numerical findings as shown in Figs. 4.2, 4.4, and 4.5, can also be used to predict the behavior of the phonon associated with the oscillations of $\mathbf{u_X}$ along the x and y-axes when the antiphase octahedral tiltings condense before the in-phase tilting in the structural path bringing the $Pm\bar{3}m$ to $Pnma$ state.

(5) Eqn. (4.9) and our numerical data implies that the results would be very similar to those seen in Fig. 4.5(a), i.e. (a) $\nu_{X_5^+,x,Pm\bar{3}m}$ hard frequency should exist in the cubic state; (b) If the phase transition sequence $Pm\bar{3}m$ —$Imma$—$Pnma$ exists in addition to $Pm\bar{3}m$ —$P4/mbm$—$Pnma$ when decreasing the temperature, according to ref. [122]. Then there will be one soft phonon (can be denoted as $\nu_{X_5^+,x,Imma,LF}$) and one hard phonon (to be coined $\nu_{X_5^+,x,Imma,HF}$) in the Imma state; (c) for the phase transition sequence $Pm\bar{3}m$ —$P4/mbm$—$Pnma$ there exists, one soft phonon at $\nu_{X_5^+,x,Pnma,LF}$ and two harder phonons at $\nu_{X_5^+,x,Pnma,MF}$ and $\nu_{X_5^+,x,Pnma,HF}$ in the Pnma state. The main difference between these predicted results and those shown in Fig. 4.5(a) is that $\nu_{X_5^+,x,Imma,LF}$ will arise from the mixing of the fluctuation of the x-component of $\mathbf{u_X}$ with the oscillation of the z-component of $\omega_\mathbf{M}$ that is mediated by the condensation of the x-component of $\omega_\mathbf{R}$. And $\nu_{X_5^+,x,P4/mbm,LF}$ of Fig. 4.5(a) involves the dynamical coupling between the x-component of $\mathbf{u_X}$ and the x-component of $\omega_\mathbf{R}$ when the z-component of $\omega_\mathbf{M}$ has adopted a long-range-order. Interestingly, symmetry arguments [122] further indicate that the $Pm\bar{3}m - to - Imma$ phase transition should be of first-order. As a result, we expect that the susceptibilities measured in the temperature interval

for which these two phases can co-exist will have the features of both of these phases.

4.5 Conclusions

Finally, to sum up, $BiFeO_3$ bulk under hydrostatic pressure was studied. We numerically and analytically found that the system is having the paraelectric cubic $Pm\bar{3}m$ state at high temperature while adopting the antipolar $Pnma$ phase at a lower temperature. Our simulations show that for a narrow range of temperature between the temperature stability regions $Pm\bar{3}m$ and $Pnma$, an intermediate state having $P4/mbm$ symmetry can occur and is also compatible with the symmetry analyzes [122]. We also reveal that AFE modes have very high resonant frequencies which are almost independent of the temperature in the $Pm\bar{3}m$ state, whereas in the intermediate state and the $Pnma$ state they can be quite small due to very specific *dynamical* mixings with the octahedral oxygen tiltings. Such mixing increases the number of antipolar phonon modes when the system passes through $Pm\bar{3}m - P4/mbm$ and $P4/mbm - Pnma$ phase transition. Also, a simple model is built to not only clarify all these features but to reveal that they arise due to trilinear energy coupling between an anti-polar motion, in-phase and anti-phase tiltings. In the case of the $Pm\bar{3}m - Imma - Pnma$ transition, this model can also be used for the dynamics of AFE modes.

We hope that this study is important to the scientific community, (i) as $Pnma$ state is the most abundant ground state in perovskites; (ii) for the ability to build high-density storage is of specific importance to antiferroelectrics systems, and (iii) because trilinear energetic couplings can also give rise to the formation of electrical polarization in the so-called hybrid improper ferroelectrics (HIF) (see chapter 1 for definition) [1, 2, 3, 4, 5, 6, 7], implying that the present study is a good starting point to tackle and understand polarization dynamics in HIF systems. The results obtained here are published in Ref. [123].

Chapter 5

ARE THERE SOFT MODES IN HYBRID IMPROPER FERROELECTRICS?

This section reports the results and analyses of atomistic simulations along with an analytical model developed explaining the dynamics of polar, antipolar, and antiferrodistortive distortions in ($BiFeO_3$)/($NdFeO_3$) (abbreviated as $(BFO)_1/(NFO)_1$) 1:1 superlattice (SL). As the main result, I obtained on cooling the paraelectric $P4/mmm$ to ferroelectric $Pmc2_1$ phase transition. As I will show, this phase transition is caused by softening of some antiferrodistortive modes. At the same time, the antiferroelectric modes in the high-temperarture paraelectric phase are hard and do not have tendency to soften. However, in the low-temperature $Pmc2_1$ phase, they are suddenly soft. In the low-temperature phase, in the correlators, which I computed, there appear seven peaks due to a trilinear energetic couplings between two types of octahedral tiltings and Bi and Nd cations motions. I will show that this leads to the appearance of spontaneous polarization, consistent with the nature of hybrid improper ferroelectricity.

In addition to these calculations, I will present a model describing the emergence of the hybrid improper ferroelectricity in our system. The model developed and described below in detail can be easily applied to predict the dynamics of polar, antipolar cation motions, and antiferrodistortive motion of anions in $(BFO)_1/(NFO)_1$ 1:1 SL in $P4/mmm$ and $Pmc2_1$ phases.

5.1 Background

A specific class of materials, namely, the so-called hybrid-improper ferroelectrics (HIF)—are gaining a lot of attention because of new mechanism of the emergence of ferroelectricity [124]. For example, HIF can be realized in materials called Superlattices which can be formed e.g. by a perovskite stack as ABO_3/A'BO_3 where both perovskites have antiferroelectric (AFE) and

antiferrodistortive displacements. The ferroelectricity in HIF materials arises from a trilinear coupling of the form PQ_1Q_2 between the spontaneous polarization known as ferroelectric mode (P) and two oxygen octahedral rotational modes denoted here as Q_1 and Q_2 [1, 2, 4, 6, 7, 125]. Up to now several works based on density functional calculations have been done to understand and characterize HIF [1, 2, 4, 5, 49], and an atomistic theory has been developed to clarify its microscopic energetic origin [8, 7].

Interestingly, all the aforementioned works on HIF have been aimed to understand static properties at 0K but finite-temperature dynamical properties of HIF remain uninvestigated. For instance, one may wonder how the ferroelectric (polar), antiferroelectric (antipolar), and octahedral rotational modes evolve with temperature? Do the polar and antipolar modes soften as in proper ferroelectrics, or are they rather hard at high temperature in the paraelectric phase [126, 127]? Do these phonon modes mix with phonons associated with fluctuations of oxygen octahedral tiltings in any of these phases because of PQ_1Q_2 trilinear energetic coupling, or rather does this hypothetical mixing only occurs when in-phase and/or antiphase tiltings have condensed?

To answer all these questions, I decided to investigate $(BFO)_1/(NFO)_1$ 1:1 superlattice (SL) to study the temperature-driven HIF transition due to the trilinear energetic coupling.

5.2 Method

The effective Hamiltonian (H_{eff}) scheme as mentioned in chapter 2 is employed to investigate finite-temperature properties of $(BFO)_1/(NFO)_1$ SL. The degree of freedoms of H_{eff} in use are the following:

(i) the local soft modes $\{u_i\}$ centered on the A sites (i.e., on Bi or Nd ions), which are directly related to the local electric dipoles on sites i [77, 78]; (2) the homogeneous $\{\eta_H\}$ and inhomogeneous $\{\eta_{I,l}\}$

strain tensors. This strain tensor is located on Fe site [77, 78]; (3) the pseudo vector $\{\omega_i\}$ that characterizes the oxygen octahedral tilting about the Fe site i [80] and (4) the magnetic moment $\{m_i\}$ centered on Fe ions at site i. The total energy of this H_{eff} has two main terms:

$$E_{total} = E_{BFO}(\{u_i\}, \{\eta_H\}, \{\eta_{I,l}\}, \{\omega_i\}, \{m_i\}) + E_{alloy}(\{u_i\}, \{\omega_i\}, \{m_i\}, \{\eta_{loc}\}) \tag{5.1}$$

where E_{BFO} is the effective Hamiltonian of pure BFO while E_{alloy} characterizes the effect of substituting Bi ions by Nd ions. The analytical expression of E_{BFO} is provided in chapters 2 and 3, while that of E_{alloy} is provided in chapter 2. E_{total} contains trilinear couplings between local modes and two octahedral tiltings [8],

$$\Delta E_1 = \sum_i \sum_{l,m,m=0,1} \sum_{\substack{\alpha,\beta=x,y,z \\ \alpha\neq\beta}} K_{1i}(-1)^{(lx+my+nz)_\alpha} \omega_{ilmn,\alpha} u_{i,\beta} \omega_{ilmn,\beta} \tag{5.2}$$

where the summation over i runs over all A sites belonging to 5-atom primitive cell i and the x, y, and z axes are chosen to lie along the pseudocubic [100], [010], and [001] directions, respectively. $\omega_{ilmn,\alpha}$ denotes the octahedral tilting that is centered on the Fe site belonging to the primitive unit cell shifted from cell i by the vector $a_{lat}(l\mathbf{x} + m\mathbf{y} + n\mathbf{z})$ with l,m,n=0 or 1 and where a_{lat} is the 5-atom lattice parameter (note that the Fe site i can be reached from A site i through a shift by $\frac{-a_{lat}}{2}(\mathbf{x} + \mathbf{y} + \mathbf{z})$). As shown in Ref. [3], the net HIF polarization arising in the $(BFO)_1/(NFO)_1$ superlattice below a certain temperature originates from the difference in the K_{1i} coefficient for the sites containing Bi *versus* Nd ions. The difference in the value of K_{1i} coefficient is due to the ionic radius of the Bi and Nd ions.

First I performed Monte-Carlo (MC) simulation to analyze static finite-temperature properties of $(BFO)_1/(NFO)_1$ SL. This SL is constructed by alternate layers of BFO and NFO within a 12x12x12 supercell along the [001] pseudo-cubic direction. I used 20,000 MC sweeps for equilibration

and another 20,000 MC sweeps were employed to calculate thermal averages. Then I performed Molecular Dynamics (MD) simulations on 12x12x12 supercell to investigate *dynamical* properties of $(BFO)_1/(NFO)_1$ SL. For MD simulations, 4×10^5 steps with a time step of 0.5 fs were used. To investigate the behavior of frequencies of different structural, ferroelectric, and antiferroelectric modes, I calculated then the following correlators:

$$\chi_{\alpha\beta}^{AA'}(\nu) = \left\langle A_\alpha(t) A'_\beta(t) \right\rangle + i2\pi\nu \int_0^\infty dt e^{i2\pi\nu t} \left\langle A_\alpha(t) A'_\beta(0) \right\rangle, \tag{5.3}$$

where ν is frequency, α and β denote Cartesian components, $A(t)$ and $A'(t)$ are order parameters at time t, and "$\langle..\rangle$" indicates thermal averages.

I focused on the following physical quantities: (i) the order parameters A were chosen to be $\mathbf{u_{Nd}}$ and $\mathbf{u_{Bi}}$ vectors that define the averaged vectorial sums of the local modes centered on the Nd and Bi sites, respectively; (ii) the $\mathbf{u_\Gamma}$ and $\mathbf{u_X}$ vectors that characterize the overall electrical polarization associated with the Γ point and antiferroelectric (AFE) vector associated with the X point of the 5-atom cubic Brillouin zone, respectively. Note that the $\mathbf{u_\Gamma}$ and $\mathbf{u_X}$ modes are defined as $\frac{1}{2}(\mathbf{u_{Nd}} + \mathbf{u_{Bi}})$ and $\frac{1}{2}(\mathbf{u_{Nd}} - \mathbf{u_{Bi}})$, respectively; and (iii) the angles of the antiphase and inphase rotations of the oxygen octahedral tiltings also known as antiferrodistortive or AFD motions and are quantified by the $\boldsymbol{\omega}_R$ and $\boldsymbol{\omega}_M$ pseudovectors, respectively. These three different quantities are energetically coupled to each other by different local trilinear couplings involved in Eqn. (5.2). For example, the z-component of $\boldsymbol{\omega}_M$ is involved in the term [8, 7]:

$$\begin{aligned} E_{trilinear,\omega_{M,z}} &= C\{\sum_{\alpha=x,y} \kappa_{Nd} u_{Nd,\alpha} \omega_{R,\alpha} \omega_{M,z} + \kappa_{Bi} u_{Bi,\alpha} \omega_{R,\alpha} \omega_{M,z}\} \\ &= C\{\sum_{\alpha=x,y} D_\Gamma u_{\Gamma,\alpha} \omega_{R,\alpha} \omega_{M,z} + D_X u_{X,\alpha} \omega_{R,\alpha} \omega_{M,z}\} \end{aligned} \tag{5.4}$$

where C is a coefficient, α is the x and y Cartesian components. κ_{Nd} and κ_{Bi} are the κ_{1i} parameters

of Eq. (5.2) for primitive unit cells containing Nd and Bi ions, respectively. Here, D_Γ and D_X are defined as $\frac{1}{2}(\boldsymbol{\kappa}_{Nd} + \boldsymbol{\kappa}_{Bi})$ and $\frac{1}{2}(\boldsymbol{\kappa}_{Nd} - \boldsymbol{\kappa}_{Bi})$, correspondingly.

For above mentioned order parameters A, the imaginary part of the complex susceptibilities computed by Eq. (5.3) are fitted by the following formula for the dielectric response of a sum of Damped Harmonic Oscillators (DHO):

$$\chi = \frac{S^2}{\nu_r^2 - \nu^2 - i\nu\gamma} \tag{5.5}$$

where ν_r , γ, and S are the resonant frequency, damping constant, and plasma frequency, respectively.

5.3 Results

The system $(BFO)_1/(NFO)_1$ 1:1 SL was cooled from 1800K to 200K in increments of 50K. Figure 5.1 displays the temperature dependence of different order parameters: panel (a) shows the supercell average of the $\mathbf{u_\Gamma}$ and $\mathbf{u_X}$ vectors; panel (b) represents the temperature dependence of the supercell average of the $\mathbf{u_{Bi}}$ and $\mathbf{u_{Nd}}$ vectors; and panel (c) reports the temperature evolution of the supercell average of the axial vectors quantifying the the oxygen octahedral tilting, $\boldsymbol{\omega}_R$ and $\boldsymbol{\omega}_M$, corresponding to the rotations in antiphase and inphase, respectively. Note that all these quantities were obtained from Monte-Carlo simulations. One can see from Figure 5.1 that above 1520K, all these quantities vanish which is representative of the $P4/mmm$ phase existing at high enough temperatures [3]. On further cooling (below 1520K), the x and y components of $\mathbf{u_\Gamma}$, $\mathbf{u_X}$, and $\omega_\mathbf{R}$ all become finite, also the z-component of $\omega_\mathbf{M}$ becoming non-null and the z-component of $\omega_\mathbf{R}$ is finite but rather small. Thus, below 1520K an electric polarization and an antipolar vector both are enhanced along the pseudo-cubic [110] direction and both are followed by the antiphase titling along [110] direction and by the inphase tiltings in the direction [001]. Hence, below 1520K, $(BFO)_1/(NFO)_1$ 1:1 SL

acquires the space group $Pmc2_1$ [3].

As shown in Figure 5.1(b), below 1520K, the average displacement of Nd ions is positive and, along [110] direction, is larger in magnitude than the displacements of Bi ions moving in opposite i.e. $[\bar{1}\bar{1}0]$ direction. As $\mathbf{u_\Gamma}=\frac{1}{2}(\mathbf{u_{Nd}}+\mathbf{u_{Bi}})$ and $\mathbf{u_X}=\frac{1}{2}(\mathbf{u_{Nd}}-\mathbf{u_{Bi}})$, $\mathbf{u_X}$ is finite and larger compared to $\mathbf{u_\Gamma}$. However, it is important that $\mathbf{u_\Gamma}$ is finite which confirms the fact that $(BFO)_1/(NFO)_1$ SL does be a HIF!

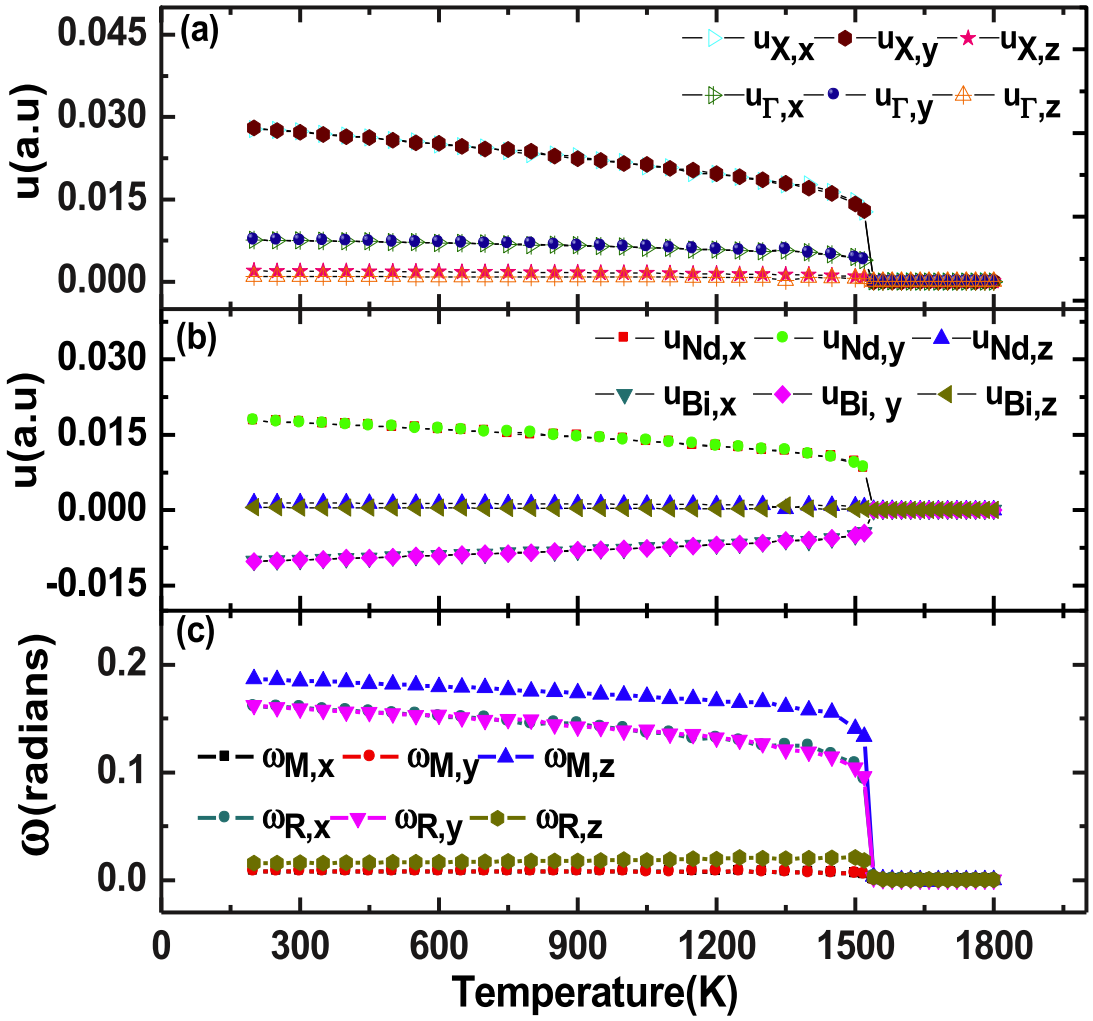

Figure 5.1: $(BFO)_1/(NFO)_1$ SL: temperature dependence of (a) the supercell averaged $\mathbf{u_\Gamma}$ and $\mathbf{u_X}$ vectors characterizing the electrical polarization and antiferroelectric vector, respectively; (b) the local mode centered on Nd and Bi cations ($\mathbf{u_{Nd}}$ and $\mathbf{u_{Bi}}$, respectively), as a function of temperature; (c) $\omega_\mathbf{R}$ and $\omega_\mathbf{M}$ pseudo vectors quantifying the antiphase and in phase tiltings, respectively.

Let us now see the effect of temperature on the susceptibility of the order parameters $\mathbf{u_\Gamma}$, $\mathbf{u_X}$,

$\mathbf{u_{Nd}}$, $\mathbf{u_{Bi}}$, $\omega_{\mathbf{R}}$, and $\omega_{\mathbf{M}}$.

Susceptibility $\chi^{AA'}_{\alpha\alpha}(\nu)$ at high temperature of 1780K i.e. $P4/mmm$ state:

In a high-temperature range i.e. from 1520K to 1800K, the $P4/mmm$ phase contains the ferroelectric (FE), antiferroelectric (AFE), and antiferrodistortive phonon modes. Figure 5.2(b) reveals the imaginary part of the susceptibility $\chi^{AA'}_{\alpha\alpha}(\nu)$ for the order parameter $A = A' = \boldsymbol{u}_X$ and $\alpha\alpha = x'x'$ where x' is along the pseudo-cubic [110] direction at temperature 1780K– that is within the $P4/mmm$ phase. One can clearly see in Figure 5.2(b) two narrow peaks: one peak occurring at $116cm^{-1}$ and the other at $134cm^{-1}$. For the order parameter $A = A' = \mathbf{u_\Gamma}$ and for $\alpha\alpha = x'x'$, two peaks occur at the same frequencies as obtained for $\boldsymbol{u}_X$. Note that the second peak appears in panel (a) as a week shoulder and it is difficult to see it, see the inset Fig. 5.2(a). The fact that two frequencies of the antiferroelectric (AFE) phonon mode (see Fig. 5.2(b)) are identical to those of the ferroelectric (FE) mode (see Fig. 5.2(a)), indicates that the oscillations associated with the $\mathbf{u_X}$ and $\mathbf{u_\Gamma}$ vectors along the x' direction are coupled. Indeed, in the effective Hamiltonian in use, the $\mathbf{u_{Nd}}$ and $\mathbf{u_{Bi}}$ modes on the nearest sites (up to the third-neighbors) are coupled via a short-range interaction of the form $Ju_{Nd,\alpha}u_{Bi,\alpha}$, where J is a coefficient and α=x or y. Let us denote the frequencies of these two peaks as $\nu^{P4/mmm}_{cation,1}$ and $\nu^{P4/mmm}_{cation,2}$. The first subscript, "cation", indicates the cation, Nd or Bi. The second subscripts indicates frequency: "1" for the low-frequency peak and "2" for high-frequency one. The superscript indicates the macroscopic phase.

Now let us look at the modes having antiferrodistortive (AFD) characters at high temperature. Figure 5.2(e) displays the imaginary part of the susceptibility corresponding to the oscillation of the $\boldsymbol{\omega}_R$ order parameter along the x' direction. It possesses a single peak located at $42cm^{-1}$ and is denoted as $\nu^{P4/mmm}_{\boldsymbol{\omega}_R}$. Similarly, Figure 5.2(f) displays the zz component of the imaginary part of the susceptibility corresponding to the oscillation of the $\boldsymbol{\omega}_M$ order parameter. It possesses a single peak

at $37cm^{-1}$ and is denoted as $\nu_{\omega_M}^{P4/mmm}$. These two frequencies are different from each other, and also different from $\nu_{cation,1}^{P4/mmm}$ and $\nu_{cation,2}^{P4/mmm}$. This indicates that ω_R and ω_M are neither dynamically coupled to each other nor dynamically coupled with FE and AFE motions in the high-temperature $P4/mmm$ phase.

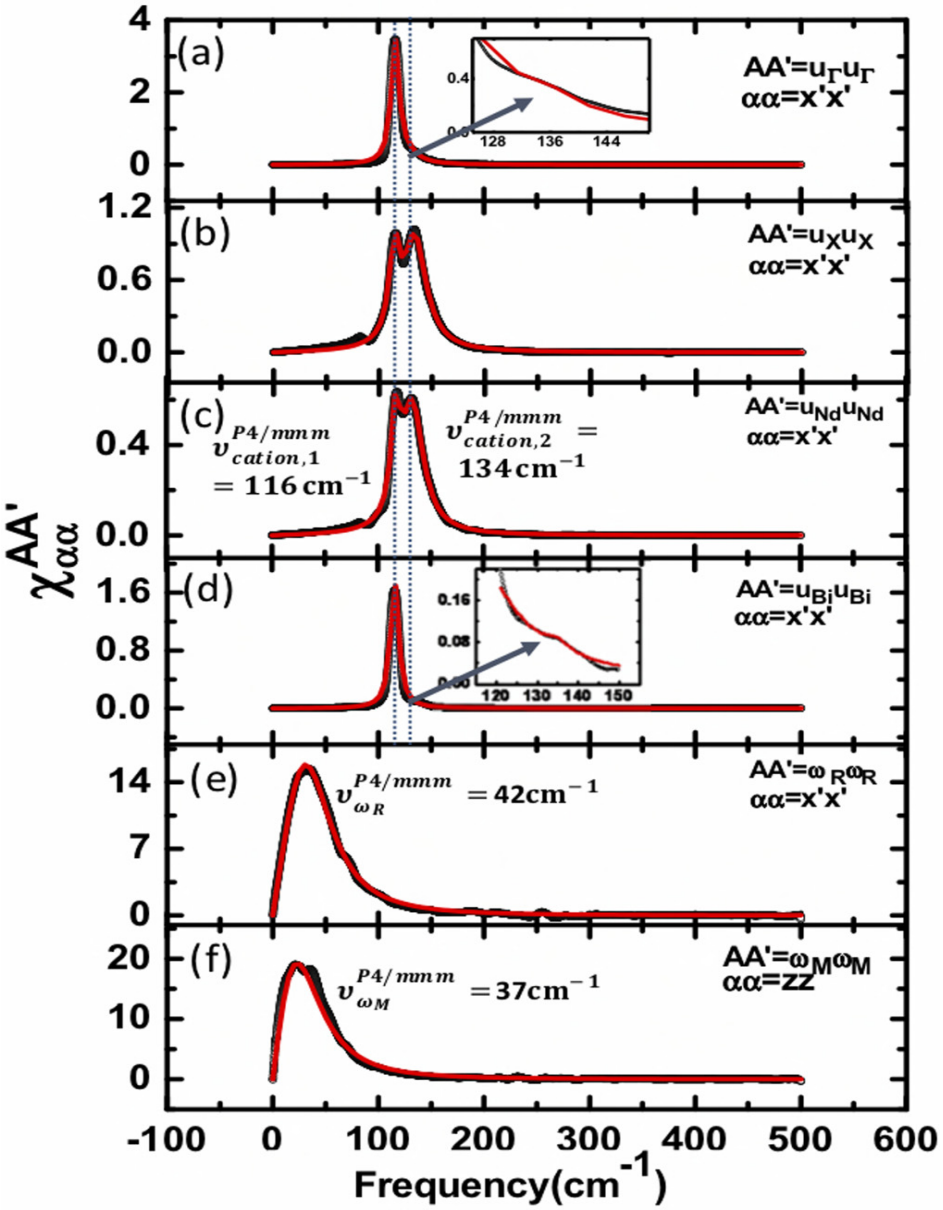

Figure 5.2: $(BFO)_1/(NFO)_1$ SL: frequency dependence of the imaginary part of $\chi_{x'x'}^{AA'}(\nu)$ and where x' is along the pseudo-cubic [110] direction (a) $\mathbf{u_\Gamma}$, (b) $\mathbf{u_X}$, (c) $\mathbf{u_{Nd}}$, (d) $\mathbf{u_{Bi}}$, (e) ω_R, and (f) ω_M. All plots were calculated at 1780K – that is, for the $P4/mmm$ phase. The black line displays the MD data while the red line represents their fit by DHOs. Insets zoom over particular peaks that are difficult to see.

Susceptibility $\chi_{\alpha\alpha}^{AA'}(\nu)$ at 750K i.e. in $Pmc2_1$ phase:

Let us now focus on results at 750K, which is the $Pmc2_1$ phase. Figure 5.3 displays the imaginary part of the susceptibilities of the order parameters $\mathbf{A} = \mathbf{A}^{'} = \mathbf{u_\Gamma}, \mathbf{u_X}, \mathbf{u_{Nd}}, \mathbf{u_{Bi}}$, $\omega_\mathbf{R}$, and $\omega_\mathbf{M}$ for the $\alpha\alpha = x'x'$, where x' is along the pseudo-cubic [110] direction. In each of these susceptibilities there occurs seven peaks around about $83cm^{-1}$, $121cm^{-1}$, $134cm^{-1}$, $162cm^{-1}$, $174cm^{-1}$, $211cm^{-1}$, and $228cm^{-1}$. One can clearly see that when the system undergoes a phase transition from $P4/mmm$– to–$Pca2_1$ there is an increase in the number of peaks, with respect to the high-temperature phase, for all these dynamical responses. The number of the peaks increases in low temperature region due to a specific dynamical coupling mixing cation motions i.e ferroelectric and antipolar motions on the one hand and the in-phase, and antiphase tiltings, on the other hand in the low-temperature $Pmc2_1$ phase. This specific coupling is the trilinear energetic coupling of Eqn. (5.4) between the x and y components of $\mathbf{u_{Nd}}$ and $\mathbf{u_{Bi}}$ (or the FE mode $\mathbf{u_\Gamma}$ and AFE mode $\mathbf{u_X}$), with the x and y components of the antiphase AFD mode, $\boldsymbol{\omega_\mathbf{R}}$, and the z component of the in-phase AFD mode, $\boldsymbol{\omega_\mathbf{M}}$. The resonant phonon frequencies associated with these seven peaks are denoted as $\nu_i^{Pmc2_1}$, with i being an integer ranging between 1 and 7, and are as shown in Figure 5.3 for all studied order parameters (see all panels).

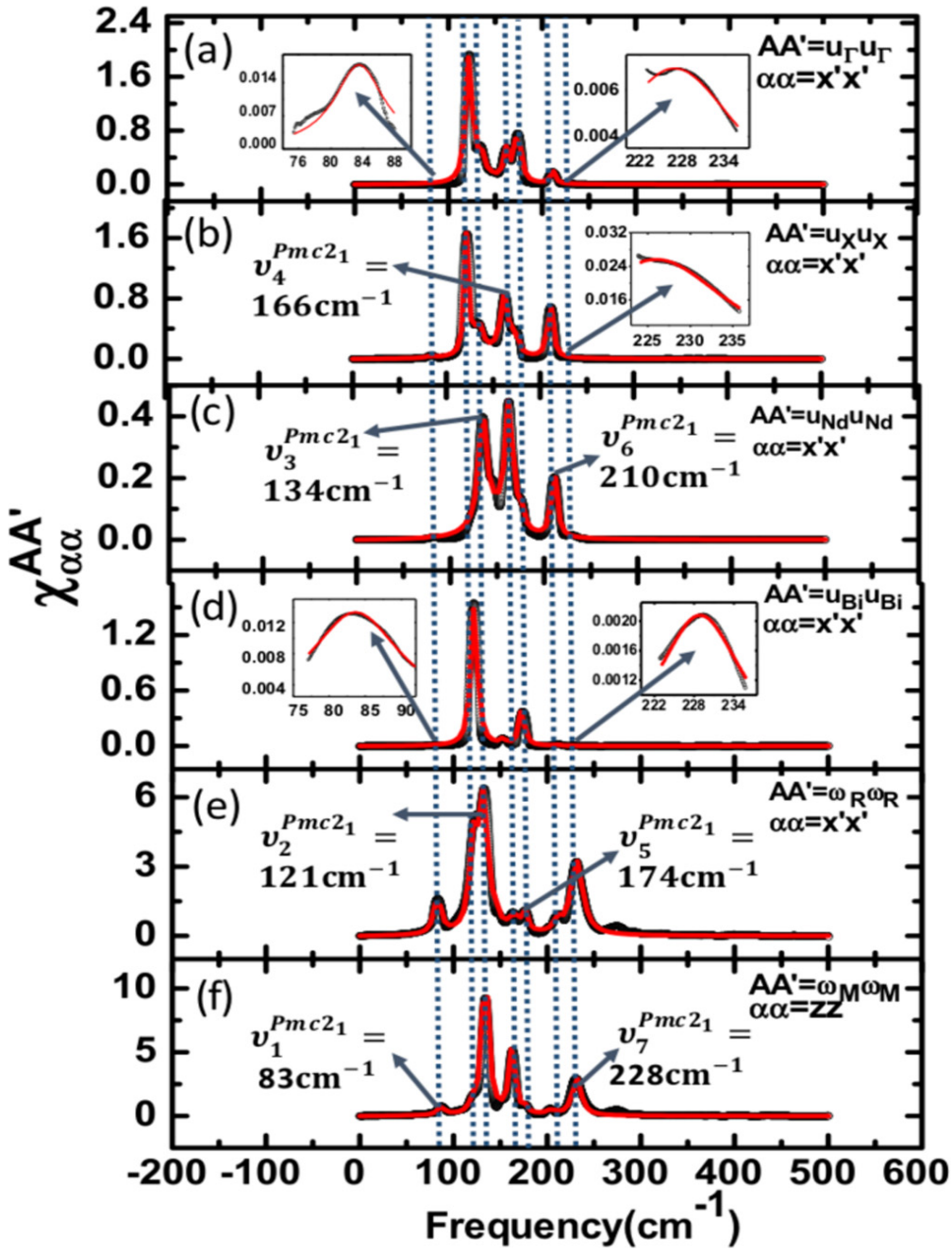

Figure 5.3: Same as Fig. 5.2 but for 750K – that is, for the $Pmc2_1$ phase.

5.3.1 Temperature evolution of the resonant phonon frequencies in $P4/mmm$ and $Pmc2_1$ phases

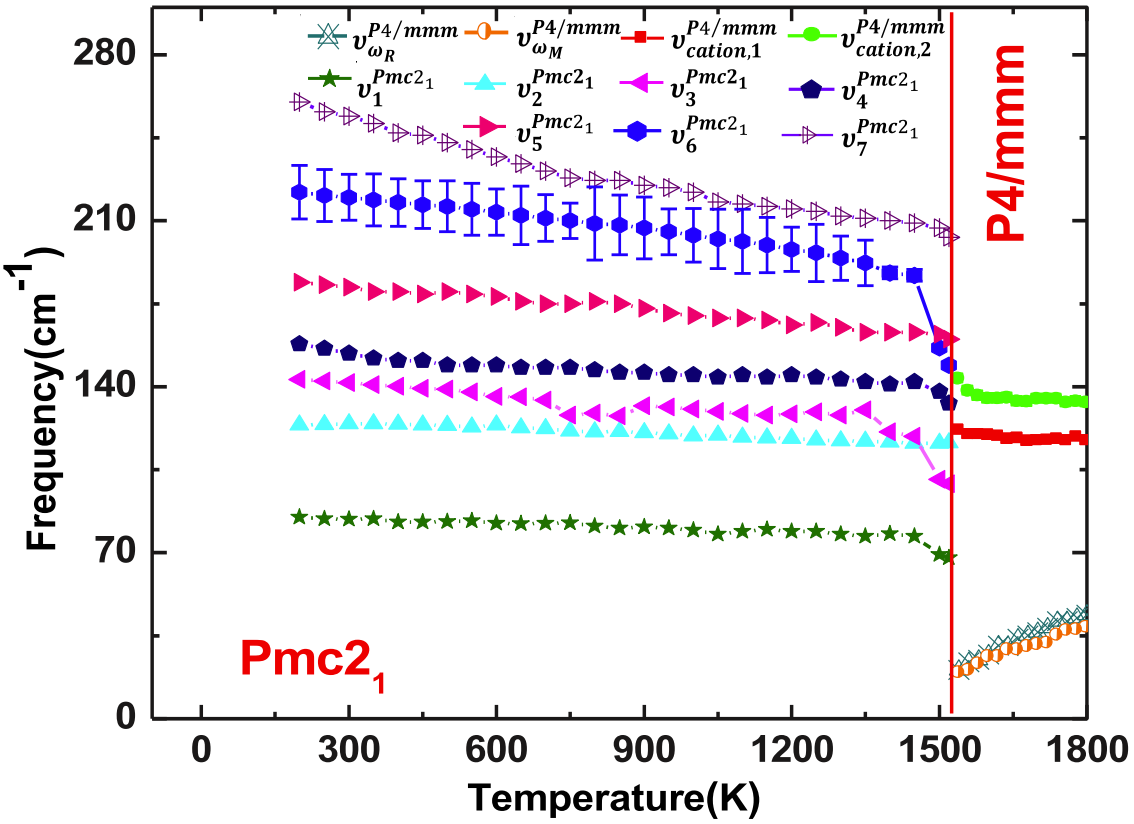

Figure 5.4: Temperature dependence of natural frequencies of phonon modes that have ferroelectric (FE), antiferroelectric (AFE) and antiferrodistortive(AFD) characters. The vertical dashed lines delimit the two different phases obtained in the calculations for our $(BFO)_1/(NFO)_1$ system. Error bars for $\nu_6^{Pmc2_1}$ arise from the slight difference in frequency that different responses (see Fig. 5.3) can have around this frequency.

Figure 5.4 displays the temperature dependences of resonant phonon frequencies, $\nu_{cation,1}^{P4/mmm}$, $\nu_{cation,2}^{P4/mmm}$, $\nu_{\omega_R}^{P4/mmm}$ and $\nu_{\omega_M}^{P4/mmm}$ in the $P4/mmm$ phase, as well as that of the $\nu_i^{Pmc2_1}$'s in the $Pmc2_1$ state.

Several important results can be inferred from this figure.

(1) When the system is cooled from high to low temperature, $\nu_{cation,1}^{P4/mmm}$ and $\nu_{cation,2}^{P4/mmm}$ frequencies remain hard in the entire range of temperature within the $P4/mmm$ state and, in particular, do not

have any tendency of softening when approaching the $P4/mmm - to - Pmc2_1$ phase transition.

(2) The $P4/mmm-to-Pmc2_1$ phase transition is driven by the condensation of the z-component of the $\boldsymbol{\omega_M}$ in-phase oxygen octahedral tiltings and the x and y components of the $\boldsymbol{\omega_R}$ anti-phase oxygen octahedral tiltings below the temperature of 1520K (see Fig. 5.1(c)), and as also demonstrated by the facts that $\nu_{\omega_R}^{P4/mmm}$ and $\nu_{\omega_M}^{P4/mmm}$ both soften dramatically on approaching the phase transition within the $P4/mmm$ state.

(3) On further decreasing the temperature below 1520K, the x and y-components of $\mathbf{u_{Nd}}$ and $\mathbf{u_{Bi}}$ (or, equivalently, of $\mathbf{u_\Gamma}$ and $\mathbf{u_X}$) become finite (see Figs 5.1(a) and 5.1(b)) and are coupled with the x and y-components of $\boldsymbol{\omega_R}$ and $\boldsymbol{\omega_M}$ modes due to the trilinear coupling given Eqn. (5.4) [3]. Such couplings lead to the emergence of the seven peaks seen in Figure 5.3 for all responses.

(4) When temperature is increased within the $Pmc2_1$ state close to the critical temperature of $\simeq$ 1520K, *most* of the seven $\nu_i^{Pmc2_1}$ frequencies soften as they contain AFD characters.

(5) Only one frequency $\nu_2^{Pmc2_1}$ is independent of temperature and rather hard within the stability region of $Pmc2_1$. Because this frequency is associated with the mode which mostly involves motions of Bi ions, and as a result has large FE and AFE characters, along the x' direction. This is indicated by the strong peaks seen in Figs. 5.3(a), (b), and (c) at this frequency. Such features explain why $\nu_2^{Pmc2_1}$ is rather close in value to $\nu_{cation,1}^{P4/mmm}$.

I developed an analytical model to understand the results depicted in Figs 5.2 and 5.3 i.e for the high and low-temperature phases. This model will help us to understand that the $\mathbf{u_{Nd}}$ and $\mathbf{u_{Bi}}$ modes are bilinearly coupled in $P4/mmm$ state while the fluctuations of $\mathbf{u_{Nd}}$, $\mathbf{u_{Bi}}$, $\boldsymbol{\omega_R}$, and $\boldsymbol{\omega_M}$ are all coupled in the $Pmc2_1$ state due to the trilinear energetic coupling.

5.4 Analytical Model

Let us begin with the equation of motion associated with considered degrees of freedom:

$$M_A \frac{d^2 q_{A,l\alpha}}{dt^2} = F_{A,l\alpha} \tag{5.6}$$

where A is one of the structural modes in the system, $q_{A,l\alpha}$ is the α Cartesian component of the corresponding displacement in the l's primitive cell, t is time, and $M(A)$ is the mass of mode A. $F_{A,l\alpha}$ is the force and is defined as:

$$F_{A,l\alpha} = -\frac{dE_{total}}{dq_{A,l\alpha}} \tag{5.7}$$

where E_{total} is the total energy of the system. Let us now define the reduced force as:

$$f_{A,l\alpha} = \frac{F_{A,l\alpha}}{\sqrt{M_A}} \tag{5.8}$$

Correspondingly, the reduced displacement associated with mode A is defined as:

$$S_{A,l\alpha} = \sqrt{M_A} q_{A,l\alpha} \tag{5.9}$$

So Eqn. (5.6) in a symmetrical form that does not contain any mass in an explicit form, can be rewritten in terms of reduced displacement as:

$$\frac{d^2 S_{A,l\alpha}}{dt^2} = f_{A,l\alpha} \tag{5.10}$$

To simplify this differential equation, the reduced displacements is considered in harmonic way:

$$S_{A,j\alpha} = e^{-i[\omega t + \boldsymbol{k_A} \cdot \boldsymbol{R}(j)]} S_{A,\boldsymbol{k_A}\alpha} \tag{5.11}$$

where $\boldsymbol{k_A}$ is a wave vector associated with mode A, $\boldsymbol{R}(j)$ is the vector locating the position of the j-th primitive cell, and $S_{A,\boldsymbol{k_A}\alpha}$ is the Fourier transform of $S_{A,j\alpha}$. Now Equation (5.11) transforms to the following form:

$$-\omega^2 \Delta S_{A,\boldsymbol{k_A}\alpha} = f_{A,\boldsymbol{k_A}\alpha} \tag{5.12}$$

where $\Delta S_{A,\boldsymbol{k_A}\alpha}$ is the fluctuation of mode A and $f_{A,\boldsymbol{k_A}\alpha}$ is the Fourier transform of the reduced force and is given as follows:

$$f_{A,\boldsymbol{k_A}\alpha} = \frac{1}{N} \sum_j e^{i[\omega t + \boldsymbol{k_A}\cdot\boldsymbol{R}(j)]} f_{A,j\alpha} \tag{5.13}$$

with N being the number of sites. Taking the time average of $f_{A,\boldsymbol{k_A}\alpha}$, one obtains the equilibrium condition of mode A in the following form:

$$\left\langle f_{A,\boldsymbol{k_A}\alpha} \right\rangle = 0 \tag{5.14}$$

Here the angle brackets represent averaging over time.

To simplify Equation (5.12) further on, we can linearize it. As the force at equilibrium is zero and gets finite only due to the displacements from the ground state, the reduced force is presented in the form of the expansion with respect to different structural displacements. In the linear approximation neglecting all higher-order terms we get:

$$f_{A,\boldsymbol{k_A}\alpha} = -\sum_{B\beta} D_{A,\boldsymbol{k_A},\alpha;B,\boldsymbol{k_B},\beta} \Delta S_{B,\boldsymbol{k_B},\beta} \tag{5.15}$$

where $D_{A,\boldsymbol{k_A},\alpha;B,\boldsymbol{k_B},\beta}$ is the dynamical matrix defined via:

$$D_{A,\boldsymbol{k_A},\alpha;B,\boldsymbol{k_B},\beta} = -\left\langle \frac{\partial f_{A,\boldsymbol{k_A}\alpha}}{\partial S_{B,\boldsymbol{k_B},\beta}} \right\rangle \tag{5.16}$$

Here the angle brackets represent averaging over time. Note that the temperature dependency of this derivative will only emerge when energy terms are higher than bilinear. For example, the temperature dependence of this quantity can be related to the trilinear coupling term. By plugging Equation (5.15) into Equation (5.12), we now get the final form of our equation:

$$\omega^2 \Delta S_{A,\boldsymbol{k_A}\alpha} = -\sum_{B\beta} D_{A,\boldsymbol{k_A},\alpha;B,\boldsymbol{k_B},\beta} \Delta S_{B,\boldsymbol{k_B},\beta} \tag{5.17}$$

To find the eigenfrequencies of this linear set of equations, one should find the roots of:

$$|\hat{D} - \omega^2 \hat{I}| = 0 \tag{5.18}$$

where $\hat{I}$ is the unity matrix.

Thus the dynamical matrix plays the central role in the model. Based on the dynamical matrix, the basic structural modes should be in compliance with the results obtained. So, I took seven modes, $q_{A,\boldsymbol{k}\alpha}$, that are: $u_{Bi,x}$, $u_{Bi,y}$, $u_{Nd,x}$, $u_{Nd,y}$, $\omega_{M,z}$, $\omega_{R,x}$ and $\omega_{R,y}$. Their associated wave vector $\boldsymbol{k}$, in $2\pi/a$ units, are $[\frac{1}{2}, \frac{1}{2}, \frac{1}{2}]$ for $\omega_{R,x}$ and $\omega_{R,y}$ *versus* $[\frac{1}{2}, \frac{1}{2}, 0]$ for $\omega_{M,z}$.

Table 5.1: Form of the dynamical matrix in our model. For simplification of notations, $u_{Bi,x}$, $u_{Bi,y}$, $u_{Nd,x}$, $u_{Nd,y}$, $\omega_{M,z}$, $\omega_{R,x}$ and $\omega_{R,y}$ are simply denoted here as Bi_x, Bi_y, Nd_x, Nd_y, M_z, R_x and R_y, respectively.

	Bi_x	Bi_y	Nd_x	Nd_y	M_z	R_x	R_y
Bi_x	$\Omega^2_{Bi,x}$		d_{xx}		$\mathrm{d}^{Bi}_{xx}\langle S_{R,x}\rangle$	$\mathrm{d}^{Bi}_{xx}\langle S_{M,z}\rangle$	
Bi_y		$\Omega^2_{Bi,y}$		d_{yy}	$\mathrm{d}^{Bi}_{yy}\langle S_{R,y}\rangle$		$\mathrm{d}^{Bi}_{yy}\langle S_{M,z}\rangle$
Nd_x	d_{xx}		$\Omega^2_{Nd,x}$		$\mathrm{d}^{Nd}_{xx}\langle S_{R,x}\rangle$	$d^{Nd}_{xx}\langle S_{M,z}\rangle$	
Nd_y		d_{yy}		$\Omega^2_{Nd,y}$	$\mathrm{d}^{Nd}_{yy}\langle S_{R,y}\rangle$		$\mathrm{d}^{Nd}_{yy}\langle S_{M,z}\rangle$
M_z	$\mathrm{d}^{Bi}_{xx}\langle S_{R,x}\rangle$	$\mathrm{d}^{Bi}_{yy}\langle S_{R,y}\rangle$	$\mathrm{d}^{Nd}_{xx}\langle S_{R,x}\rangle$	$\mathrm{d}^{Nd}_{yy}\langle S_{R,y}\rangle$	$\Omega^2_{M,z}$	$\mathrm{d}^{Bi}_{xx}\langle S_{Bi,x}\rangle + \mathrm{d}^{Nd}_{xx}\langle S_{Nd,x}\rangle$	$\mathrm{d}^{Bi}_{yy}\langle S_{Bi,y}\rangle + \mathrm{d}^{Nd}_{yy}\langle S_{Nd,y}\rangle$
R_x	$\mathrm{d}^{Bi}_{xx}\langle S_{M,z}\rangle$		$\mathrm{d}^{Nd}_{xx}\langle S_{M,z}\rangle$		$\mathrm{d}^{Bi}_{xx}\langle S_{Bi,x}\rangle + \mathrm{d}^{Nd}_{xx}\langle S_{Nd,x}\rangle$	$\Omega^2_{R,x}$	
R_y		$\mathrm{d}^{Bi}_{yy}\langle S_{M,z}\rangle$		$\mathrm{d}^{Nd}_{yy}\langle S_{M,z}\rangle$	$\mathrm{d}^{Bi}_{yy}\langle S_{Bi,y}\rangle + \mathrm{d}^{Nd}_{yy}\langle S_{Nd,y}\rangle$		$\Omega^2_{R,y}$

Table 5.1 shows the form of the dynamical matrix obtained in the frame of the model considered

here. There are seven diagonal elements denoted as $\Omega^2_{qA,\alpha}$ (see diagonal terms of Table 5.1), since the Nd and Bi have different masses as well as different quadratic energy terms for the local modes. Here the diagonal terms $\Omega^2_{R,x}$ and $\Omega^2_{R,y}$ are the same, similarly $\Omega^2_{Nd,x}$= $\Omega^2_{Nd,y}$ as well as $\Omega^2_{Bi,x}$= $\Omega^2_{Bi,y}$. The non diagonal terms include bilinear and trilinear coupling terms as follows: (i) the elements d_{xx} and d_{yy} are related to the bilinear coupling between the Bi and Nd displacements. These non diagonal elements are related to the microscopic effective Hamiltonian short-range bilinear energetic $J_{ij,\alpha\beta}$ coefficient (see Eqn. (2.33) of chapter 2); and (ii) the product of the elements d^{Bi}_{xx}, d^{Bi}_{yy}, d^{Nd}_{xx} or d^{Nd}_{yy} with the corresponding time-average of the appropriate tilting mode are related to the trilinear terms between local modes and tiltings. These quantities are related to the trilinear coupling coefficients between local modes and AFD motions which are denoted by $\kappa_{ij,\alpha\beta}$ (see Eqn. 2.43 of chapter 2).

Let us now study the solution Equation (5.18) for high temperature and low-temperature phases of RBFO based on the dynamical matrix of Table 5.1.

Case I: The $P4/mmm$ phase

In this case, the average of $\omega_{M,z}$, $\omega_{R,x}$ and $\omega_{R,y}$ all vanish and they are all decoupled from each other and from the local modes centered on Bi and Nd ions. The local modes centered on Bi and Nd ions are coupled to each other via the $d_{\alpha\alpha}$ terms of Table 5.1. The equations of motions are then defined as:

$$(\Omega^2_{Nd,\alpha} - \omega^2)S_{Nd,\alpha} = -d_{\alpha\alpha}S_{Bi,\alpha} \tag{5.19}$$

$$(\Omega^2_{Bi,\alpha} - \omega^2)S_{Bi,\alpha} = -d_{\alpha\alpha}S_{Nd,\alpha} \tag{5.20}$$

So we predict here only two peaks in the dielectric response at this temperature and they correspond

to two modes, which are bilinearly coupled in the x and y directions. Indeed, the responses of the Nd and Bi ions (see Figs 5.2(c) and 5.2(d)) have only two peaks. On solving Eqns. (5.19) and (5.20) one gets the eigenvalues that can be found from Equation (5.18):

$$\omega^2 = \frac{\Omega^2_{Nd,\alpha} + \Omega^2_{Bi,\alpha}}{2} \pm \sqrt{\left(\frac{\Omega^2_{Nd,\alpha} - \Omega^2_{Bi,\alpha}}{2}\right)^2 + d^2_{\alpha\alpha}} \tag{5.21}$$

It can be seen that these two solutions are both very close to the bare frequencies of the Nd and Bi modes for $\alpha = x', y'$, but because of coupling constant $d_{\alpha\alpha}$, are shifted from them.

Case II: The $Pmc2_1$ phase.

This case is more complex. It is seen from Figure 5.3, each of the responses provides seven lines because of the above-mentioned seven modes, all coupled by the trilinear terms reported in Table 5.1. These seven modes are coupled via trilinear terms because all averages of $\omega_{R,x}$, $\omega_{R,y}$ and $\omega_{M,z}$ are all now finite (see figure 1(a, c)).

Moreover, one can determine the improper polarization by employing Eq. (5.14). Indeed, Eq. (5.14) takes, for the Nd and Bi modes in $Pmc2_1$ phase, the following form:

$$\Omega^2_{Nd,\alpha} \left\langle S_{Nd,\alpha} \right\rangle + d_{\alpha\alpha} \left\langle S_{Bi,\alpha} \right\rangle = -d^{Nd}_{\alpha\alpha} \left\langle S_{M,z} \right\rangle \left\langle S_{R,\alpha} \right\rangle \tag{5.22}$$

$$\Omega^2_{Bi,\alpha} \left\langle S_{Bi,\alpha} \right\rangle + d_{\alpha\alpha} \left\langle S_{Nd,\alpha} \right\rangle = -d^{Bi}_{\alpha\alpha} \left\langle S_{M,z} \right\rangle \left\langle S_{R,\alpha} \right\rangle \tag{5.23}$$

The solutions of these equations are:

$$\begin{aligned} < S_{Nd,\alpha} > &= \frac{-d^{Nd}_{\alpha\alpha}\Omega^2_{Bi,\alpha} + d^{Bi}_{\alpha\alpha} d_{\alpha\alpha}}{\Omega^2_{Nd,\alpha}\Omega^2_{Bi,\alpha} - d^2_{\alpha\alpha}} \left\langle S_{M,z} \right\rangle \left\langle S_{R,\alpha} \right\rangle \\ < S_{Bi,\alpha} > &= \frac{-d^{Bi}_{\alpha\alpha}\Omega^2_{Nd,\alpha} + d^{Nd}_{\alpha\alpha} d_{\alpha\alpha}}{\Omega^2_{Bi,\alpha}\Omega^2_{Nd,\alpha} - d^2_{\alpha\alpha}} \left\langle S_{M,z} \right\rangle \left\langle S_{R,\alpha} \right\rangle \end{aligned} \tag{5.24}$$

These formulas show that $\left\langle S_{Nd,\alpha} \right\rangle$ and $\left\langle S_{Bi,\alpha} \right\rangle$ are finite only if $\left\langle S_{M,z} \right\rangle$ and $\left\langle S_{R,\alpha} \right\rangle$ are finite. This means that it is the condensation of the tilting modes that results in finite cation displacements

below 1520K. Note that $d_{\alpha\alpha}^{Nd}$ and $d_{\alpha\alpha}^{Bi}$ have different magnitudes and also have opposite signs. Consequently, and since $\Omega_{Nd,\alpha}^2$ is also different from $\Omega_{Bi,\alpha}^2$, $\left\langle S_{Nd,\alpha} \right\rangle$ and $\left\langle S_{Bi,\alpha} \right\rangle$ have different amplitudes and have different signs. As a result, one can get a finite electrical polarization, which is simply related to $\left\langle \frac{S_{Nd,\alpha}}{\sqrt{M_{Nd}}} \right\rangle + \left\langle \frac{S_{Bi,\alpha}}{\sqrt{M_{Bi}}} \right\rangle = \left\langle u_{\Gamma,\alpha} \right\rangle$ in our superlattice, which is the essence of HIF. Their difference will contribute to the antiferroelectric displacement, i.e $\left\langle \frac{S_{Nd,\alpha}}{\sqrt{M_{Nd}}} \right\rangle$ - $\left\langle \frac{S_{Bi,\alpha}}{\sqrt{M_{Bi}}} \right\rangle = \left\langle u_{X,\alpha} \right\rangle$.

Moreover, when approaching the transition temperature of 1520 K from below (i.e., within the $Pmc2_1$ phase), the bare frequencies of the ω_R and ω_M tilting modes should soften, these behavior can be seen in Figure 5.4 when approaching this transition from above i.e., within the $P4/mmm$ state. When approaching this transition from below, as seen from Figure 5.4, the coupling of these tilting modes with the FE and AFE modes within the $Pmc2_1$ phase naturally decreases towards zero, and, finally, after the phase transition, only the hard AFE modes remain visible.

5.5 Conclusion

In summary, I have studied the temperature dependences of the phonon frequencies in $(BFO)_1/(NFO)_1$ SL. This system has a tetragonal $P4/mmm$ paraelectric state at high temperatures and a low temperature polar $Pmc2_1$ phase.

The resonant frequencies of all polar and antipolar modes are rather hard and nearly independent of temperature within $P4/mmm$ state, while most of them abruptly become very soft in low-temperature $Pmc2_1$ phase near the phase transition temperature, because of very specific trilinear mixing of the soft oxygen octahedral tilting modes with polar and antipolar distortions. Such mixing increases the number of the peaks the correlators of each phonon modes possessing polar, antipolar, and antiferrodistortive distortions, when passing through the phase transition from $P4/mmm$ phase to $Pmc2_1$ phase on cooling. The behavior of the polar modes is different in the high- and low-

temperature regions which render hybrid improper ferroelectrics dramatically different from proper ferroelectrics. In proper ferroelectrics the polar modes soften both in the high- and low-temperature phases when approaching the transition while in improper ferroelectrics the polar modes are hard in the high-temperature phase [126, 127].

A simple analytical model developed here explains all these features. This study is of great importance because it provides a novel mechanism of resulting in HIF. The results obtained here are published in Ref. [128].

Chapter 6

PROPERTIES OF (001) $NANBO_3$ FILMS UNDER EPITAXIAL STRAIN: A FIRST-PRINCIPLES STUDY

6.1 Introduction

Sodium Niobate with the chemical formula $NaNbO_3$ (NNO) is among the most attractive materials due to its application in optics, electronics, photocatalysis, and as thermoelectrics sensors. NNO undergoes the largest set of phase transitions (see [129, 130, 131, 132, 133, 134, 135, 136, 137, 138, 139, 140] and references therein). Darlington and Megaw reported a first detailed discussion of different structural phase transitions in NNO [133]. They suggested that, at high-temperatures, NNO is paraelectric (PE) and cubic ($Pm\bar{3}m$). It undergoes a phase transition to PE tetragonal $P4/mbm$ at a transition temperature of 913K. Next, there appear three distinct phase transitions into orthorhombic phases: to *Cmcm* at 848K, *Pmmn* at 793K, and to *Pmmn* at 753K. All these three orthorhombic phases adopt oxygen octahedral tilting patterns (also known as antiferrodistortive distortions). At 633K, NNO undergoes a phase transition adopting the *Pbcm* phase which is assumed to have a complex crystal structure at room temperature and is stable over a wide temperature range down to 173K. The *Pbcm* phase is antiferroelectric that is particularly promising for energy storage devices [141]. At 173K, NNO undergoes a next phase transition, to rhombohedral FE $R3c$ phase which possesses an electrical polarization. Additional phases, including orthorhombic polar $Pmc2_1$ [135, 136, 137] or monoclinic *Pm* [138], were proposed in NNO. Similarly, recent first-principles-based atomistic simulations [142] predicted that the most stable state near room temperature is not really the antiferroelectric *Pbcm* state but rather another orthorhombic state of $Pca2_1$ symmetry that distinguishes itself from *Pbcm* via the additional occurrence of a small but finite spontaneous

polarization along a [001] crystallographic direction.

The strain engineering in which a material is deposited on different substrates can dramatically alter the properties of perovskites. Epitaxial strain in a thin film changes crystal lattice parameters of the deposited material due to the fit of the in-plane lattice parameters of this material to the lattice parameters of the substrate. One can tune the epitaxial strain to moderate the properties of thin films and to induce phase transitions. This is, e.g., evidenced from the stabilization of a ferroelectric phase in the quantum paraelectric $SrTiO_3$ system when in thin-film form [143], or from the occurrence of the polar $Pmc2_1$ phase at room temperature in NNO thin films [144].

Surprisingly, many questions remain open regarding NNO films, partly due to the fact that only a few substrates have been used so far to grow NNO thin films [137, 144, 145] and due to the fact that the pioneering first-principles study of Ref. [146] did not include oxygen octahedral tilting in their calculations - while such degrees of freedom are important and relevant in NNO systems (see Ref. [142] and references therein). Consequently, the following questions remain open: can epitaxial NNO thin films have different ground states depending on the misfit strain they experience? Are these phases ferroelectric, antiferroelectric, or antiferrodistortive? Can the polar $Pca2_1$ and $Pmc2_1$ be such ground states? What happens to the $R3c$ bulk-ground-state phase under the misfit strain? How do the ferroelectric, antiferroelectric or antiferrodistortive properties evolve within a given phase as a function of strain? For instance, can one enhance the polarization by strain-engineering within a polar phase? Can we also increase the difference in energy between a ferroelectric and antiferroelectric states, which will impact energy-storage properties? The aim of this chapter is providing the answers to all these questions by performing and analyzing first-principles calculations on NNO epitaxial (001) thin films.

6.2 Method

6.2.1 Computational Details.

The results of the present chapter were obtained by means of the density functional theory (DFT) calculations employing the Vienna ab initio simulation package (VASP) [147] together with the Projector Augmented Wave [148, 149] (PAW) formalism. For the latter, standard PAW pseudopotentials supplied with VASP were employed: PBEsol PAW for Na ($2p^6 3s^1$) with seven valence electrons, PBEsol PAW for Nb ($4s^2 4p^6 4d^4 5s^1$) with thirteen valence electrons, and PBEsol PAW for O ($2s^2 2p^4$) with six valence electrons. Structural relaxations was performed using Generalized Gradient Approximation (GGA) within the Perdew-Burke-Ernzerhof functional for solids (PBEsol) [150]. A plane-wave basis with a kinetic energy cutoff of 550 eV is used.

6.2.2 Epitaxial strain.

The epitaxial strain imposed by a cubic substrate is defined as

$$\eta_{\text{misfit}} = \frac{a - a_0}{a_0} \times 100\% \tag{6.1}$$

where a represents the in-plane lattice constant of the substrate and a_0 is the in-plane lattice constant resulting from the energy minimization of the Cc phase. Practically, a_0 is numerically found here to be equal to 3.910 Å, which corresponds to a reasonable overestimation of about 0.9% of the experimental lattice constant of 3.875 Å for the $R3c$ phase of NNO bulk at 12K [151].

To model a perfect epitaxy on a cubic substrate, the strain tensor, in Voigt notation, has three elements that are frozen during each simulation. They are:

$$\eta_1 = \eta_2 = \eta_{\text{misfit}}, \eta_6 = 0 \tag{6.2}$$

η_3, η_4, and η_5 are allowed to relax, along with all internal atomic coordinates, until the Hellmann-

Feynman force on each atom is converged to be less than 0.001eV/Å for each varied misfit strain. To impose these conditions on the unit cell, we set certain components of the cell forces to zero in such a way that the respective components of the lattice vectors feel no force and do not change during the relaxation. Mathematically, the change in the cell shape is expressed as follows (This method was described inside subroutine constr_cell_relax of VASP code, but has not been officially documented yet):

$$a_{i,j}^{new} = a_{i,j}^{old} + \sum_{k} R_{i,k} \cdot a_{k,j}^{old} \tag{6.3}$$

where $a_{k,j}^{old}$ and $a_{i,j}^{new}$ are the lattice vectors before and after each step of relaxation of the cell respectively. i, j, and k are the Cartesian components of the lattice vector, and $R_{i,k}$ is the matrix calculated by VASP on the basis of Hellmann-Feynman forces. At the same time, this matrix allows imposing additional constraints on the change of the lattice parameters. In the case of NNO epitaxial film on a (001) substrate Eqn. (6.3) can be written as follows:

$$\sum_{k} R_{i,k} \cdot a_{k,j}^{old} = a_{i,j}^{new} - a_{i,j}^{old} \tag{6.4}$$

In the equation above, I put all elements $R_{3,i}$'s equal to the values calculated by VASP, but I vanished all other elements of this matrix. Applying this condition to equation (6.4), one gets

$$\begin{pmatrix} 0 & 0 & 0 \\ 0 & 0 & 0 \\ R_{31} & R_{32} & R_{33} \end{pmatrix} \begin{pmatrix} a_{11}^{old} & a_{21}^{old} & a_{31}^{old} \\ a_{12}^{old} & a_{22}^{old} & a_{32}^{old} \\ a_{13}^{old} & a_{23}^{old} & a_{33}^{old} \end{pmatrix} = \begin{pmatrix} a_{11} - a_{11}^{old} & a_{12} - a_{12}^{old} & a_{13} - a_{13}^{old} \\ a_{21} - a_{21}^{old} & a_{22} - a_{22}^{old} & a_{23} - a_{23}^{old} \\ a_{31} - a_{31}^{old} & a_{32} - a_{32}^{old} & a_{33} - a_{33}^{old} \end{pmatrix} \tag{6.5}$$

$$\begin{pmatrix} 0 & 0 & 0 \\ 0 & 0 & 0 \\ R_{11}a_{13}^{old} + R_{12}a_{23}^{old} + R_{13}a_{33}^{old} & R_{21}a_{13}^{old} + R_{22}a_{23}^{old} + R_{23}a_{33}^{old} & R_{31}a_{13}^{old} + R_{32}a_{23}^{old} + R_{33}a_{33}^{old} \end{pmatrix} = \begin{pmatrix} a_{11} - a_{11}^{old} & a_{12} - a_{12}^{old} & a_{13} - a_{13}^{old} \\ a_{21} - a_{21}^{old} & a_{22} - a_{22}^{old} & a_{23} - a_{23}^{old} \\ a_{31} - a_{31}^{old} & a_{32} - a_{32}^{old} & a_{33} - a_{33}^{old} \end{pmatrix} \tag{6.6}$$

One can see that the lattice parameters do not change along the lattice vectors corresponding to the first two strings of matrix “a", but the lattice parameter changes along the third lattice vector. This implies that the cell was allowed to relax along the [001] direction, while the cell along the x- and y- directions was fixed that corresponds to the epitaxial conditions in Eqn. (6.2). Note that I found the equilibrium for each considered point of the strain in the self-consistent manner provided by VASP. The epitaxial strain was imposed by selecting the in-plane lattice constant in $NaNbO_3$ in the range from $0.9566a_0$ to $1.0434\ a_0$. The corresponding misfit strain was calculated by using Equation (6.1).

I investigated different phases, namely $Pna2_1$, $Pnma$, $Pbcm$, $Pmmm$, $Imma$, $P222_1$, $P42nmc$, $Pmnn$, $Cmcm$, Cc, $Pmc2_1$, $Pca2_1$, and $Pmn2_1$. I numerically found that Cc, $Pca2_1$, and $Pmc2_1$

phases are the three low-energy states compared to all other states. The first phase has monoclinic symmetry corresponding to space group Cc (No. 9) with a polarization having an in-plane component along [110] direction and an out-of-plane component, P_z, along [001] direction. This Cc phase can be thought of as originating from the $R3c$ rhombohedral (polar) ground state of NNO bulk [151, 152] but subject to epitaxially-induced monoclinic distortions. The second low energy phase is the $Pca2_1$ phase which belongs to the orthorhombic space group (No. 29), with a polarization P_z being fully along the out-of-plane [001] direction. This $Pca2_1$ state is derived from the antiferroelectric $Pbcm$ state of NNO bulk [153], with additional polarization along [001] direction. The addition of polarization lowers the energy of $Pca2_1$ state as predicted in Ref. [142]. Finally, the third phase is the $Pmc2_1$ phase which has an orthorhombic space group (No. 26) and its polarization is fully in-plane and along [110]. This polar $Pmc2_1$ state has been reported for NNO epitaxial films under electric field [137, 144] and has also been proposed for a candidate of the so-called Q phase of NNO bulks [145].

The polarization for each of these low-energy structures was calculated using the Berry phase method [75, 154]. In appendix C, the details of the calculations of polarization using the Berry Phase Method are included.

6.3 Results and Disucussion

Figure 6.1 shows the ground state energy of (001) NNO epitaxial films as a function of the misfit strain for the three aforementioned structural phases. The ground-state for the strain ranging from a compressive strain of -4.34% to a tensile strain of +1.27% is found to be the monoclinic Cc state.

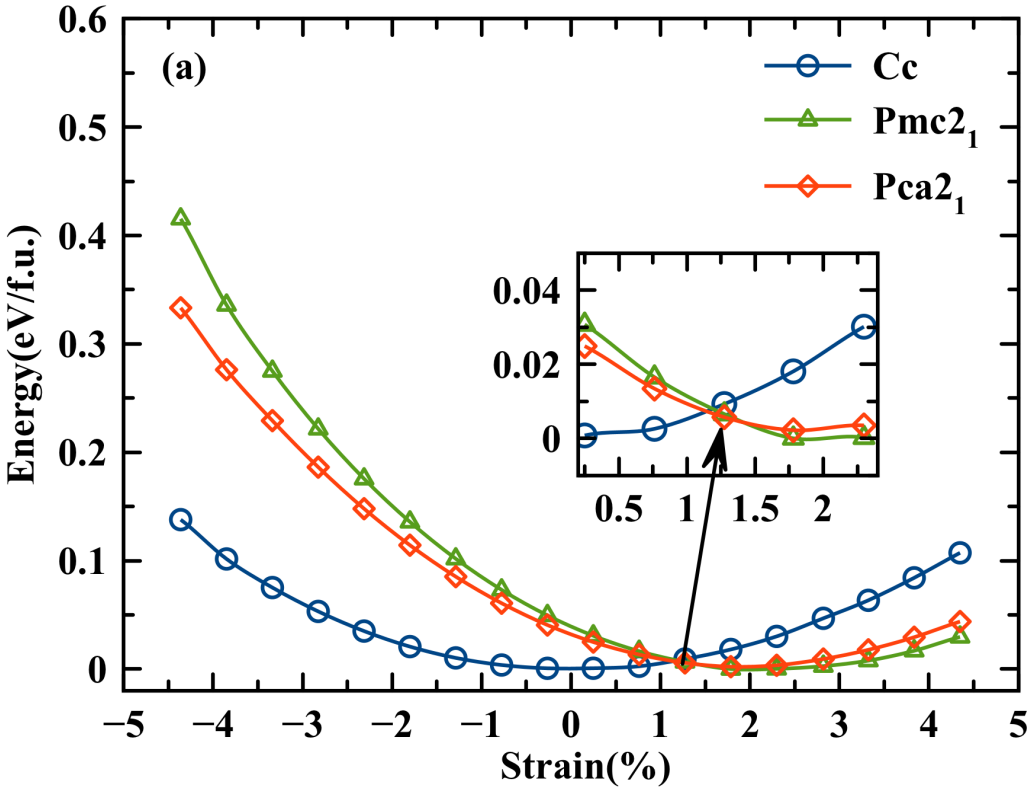

Figure 6.1: Total energy-*versus*-misfit strain for the Cc, $Pca2_1$, and $Pmc2_1$ phases of epitaxial (001) $NaNbO_3$ thin films. The zero of energy corresponds to the minimal energy, which is associated with the $Pmc2_1$ phase at the epitaxial strain of +1.78%.

The orthorhombic $Pca2_1$ phase then becomes the ground state in a narrow misfit strain region varying from +1.27% to +1.50%. For higher misfit tensile strains and up to our largest investigated value of +4.34%, the lowest energy phase is then $Pmc2_1$. Note that the $Pca2_1$, $Pmc2_1$, and Cc phases all have similar energy for a tensile strain of +1.27% (see inset of Figure 6.1), implying that these three phases may all stabilize for strains of this magnitude. The zero of energy is found to correspond to the $Pmc2_1$ state for the tensile strain of 1.78%. With respect to this zero of energy, the lowest energy of the Cc phase is equal to 0.7 meV/f.u and happens for the strain of 0%. Hence, $Pmc2_1$ has the lowest energy among all computed energies. However, in bulk, I found numerically that the $R3c$ state (from which Cc is derived) has the lowest energy which is consistent with the known $R3c$ experimental ground state of NNO bulks (see, e.g., Ref. [151]). Here, different phases

originate from the misfit conditions freezing η_1, η_2 but also imposing $\eta_6 = 0$. We numerically found that allowing η_6 to be finite within Cc will make its energy lower than that of the $Pmc2_1$ state at 1.78% strain.

Next, let us discuss some specific substrates that can help us to check the accuracy of our prediction. One of the most often employed substrates is $SrTiO_3$ (STO) single crystal for the growth of epitaxial perovskite films which has a lattice constant of 3.905Å [155]. Our predicated lattice parameter is 0.9% overestimated and corresponds to a value of 3.940Å and according to Eq. (6.1) a tensile misfit strain is +0.8% that the NNO films will experience. As a result, Figure (6.1) shows that an epitaxial film of NNO on STO is supposed to result in a Cc ground state, but with the $Pca2_1$ and $Pmc2_1$ phases being very similar in energy and therefore also accessible too (especially by, e.g., varying temperature). The $DyScO_3$ substrate has lattice parameters equal to 5.442Å and 5.719Å along two different and perpendicular in-plane $\langle 110 \rangle$ directions. Averaging these two values, dividing by square-root of two, rescaling the resulting number by the explained above 0.9% overestimation and then inserting it into Eqn. (6.1), I got that our a lattice parameter corresponds to a tensile strain of 1.81%. At this tensile strain, the ground state has $Pmc2_1$ symmetry, according to Fig. (6.1). This result is precisely what Ref. [140] observed. When considering a and b lattice parameters different from each other (as consistent with a DyScO3 substrate), I found that the symmetry is then lowered to Pm (space group #6). To help experimentalists to check this prediction, Table 6.1 reports the lattice constants and cell angles for the relaxed Cc phase at 0.24% strain, the $Pca2_1$ state under a misfit strain of 1.45%, and the $Pmc2_1$ phase subject to an epitaxial strain of 1.78%, while Tables 6.2, 6.3, and 6.4 display the corresponding atomic coordinates for these three phases at these selected strains.

Table 6.1: Crystal structure of the Cc phase at 0.24% strain, $Pca2_1$ state at 1.45% strain and $Pmc2_1$ phase at 1.78% strain

Phases	Lattice Constants			Cell angles		
	a	b	c	α	β	γ
Cc	3.920	3.920	3.897	89.34	89.34	90
$Pca2_1$	5.610	5.610	15.721	90	90	90
$Pmc2_1$	5.628	5.628	7.753	90	90	90

Table 6.2: Atomic Coordinates of Cc Phase at 0.24% strain

Label	Symbol	Multiplicity	Wyckoff label	Fractional Coordinates			Occupancy
				x	y	z	
Na1	Na	4	a	0.01555	0.25132	0.29827	1.0
Nb1	Nb	4	a	0.25749	0.25070	0.02621	1.0
O1	O	4	a	0.27645	0.46686	0.73567	1.0
O2	O	4	a	0.71328	0.47034	0.73604	1.0
O3	O	4	a	-0.00277	0.31316	0.73381	1.0

Table 6.3: Atomic Coordinates of $Pca2_1$ Phase at 1.45% strain

Label	Symbol	Multiplicity	Wyckoff label	Fractional Coordinates			Occupancy
				x	y	z	
Na1	Na	4	a	0.26415	0.25717	0.00524	1.0
Na2	Na	4	a	0.22016	0.25698	0.25443	1.0
Nb1	Nb	4	a	0.74020	0.24300	0.13063	1.0
Nb2	Nb	4	a	0.26290	0.75128	0.88029	1.0
O1	O	4	a	-0.03456	0.54048	0.13851	1.0
O2	O	4	a	0.03059	0.46143	0.85740	1.0
O3	O	4	a	0.54517	-0.04153	0.10797	1.0
O4	O	4	a	0.44866	0.04496	0.88772	1.0
O5	O	4	a	0.76999	0.18823	0.24894	1.0
O6	O	4	a	0.74915	0.30923	-0.00113	1.0

Table 6.4: Atomic Coordinates of $Pmc2_1$ Phase at 1.78% strain

Label	Symbol	Multiplicity	Wyckoff label	Fractional Coordinates			Occupancy
				x	y	z	
Na1	Na	2	a	0.00000	0.26065	0.25465	1.0
Na2	Na	2	b	0.50000	0.25754	0.28324	1.0
Nb1	Nb	4	c	0.74962	0.75532	0.26674	1.0
O1	O	4	c	0.71866	0.46202	0.02624	1.0
O2	O	4	c	0.77997	-0.03843	-0.04759	1.0
O3	O	2	a	0.00000	0.69007	0.24259	1.0
O4	O	2	b	0.50000	0.81096	0.22204	1.0

Thus, NNO film undergoes the Cc-$Pca2_1$-$Pmc2_1$ phase transition sequence when epitaxial strain increases from -4.34% to +4.34% as shown in Fig. (6.1). The phase transitions Cc-$Pca2_1$ and $Pca2_1$-$Pmc2_1$ are first-order in nature since the relevant energy-*versus*-strain curves cross each other rather than evolve one into another. I will discuss in detail the effect of strain on some physical properties during these phase transitions in NNO thin film. Let us define some vectorial quantities that will help us to understand the evolution of different ground states as a function of strain:

$$u_{\mathbf{k},\alpha} = \frac{1}{N}|\sum_{i} u_{i,\alpha}\exp(i\mathbf{k}\cdot\mathbf{R}_i)| \tag{6.7}$$

where $\mathbf{k}$ is a vector of the first cubic Brillouin zone and α denotes x, y, or z Cartesian components, with the x-, y- and z-axes being along the [100], [010] and [001] pseudo-cubic directions, respectively; symbol |...| represents the magnitude of a complex number; $\mathbf{u}_i$ is the so-called local mode of the 5-atom cell i located at a vector $\mathbf{R}_i$ from a chosen origin. This local mode is defined as [156]

$$u_{i,\alpha} = \sum_{\tau} \zeta_{\alpha}^{\tau}(i,\alpha)v_{\alpha}^{\tau} \tag{6.8}$$

where α is a Cartesian direction, τ is the atom's label, v is the corresponding atomic displacement, and ζ represents the eigenvectors of the force-constant matrix [156]. This local mode corresponds to collective displacements of Na, Nb, and oxygen ions associated with the lowest optical phonon branch of the cubic phase, and is centered on Na ions. The summation is carried over all N 5-atom cells i present in the supercell. Note that if k=0 then $\mathbf{u}_i$ in Eqn. (6.7) is related to the electrical polarization.

Similarly, one can also define a local pseudo-vector, ω_i, for which the direction is the axis of rotation of the oxygen octahedron centered at the Nb-center i and for which the magnitude is the angle of such rotation [80]. One can then calculate another vectorial quantity, which is the Fourier

transform of ω_i:

$$\omega_{\mathbf{k},\alpha} = \frac{1}{N}|\sum_i \omega_{i,\alpha}\exp(i\mathbf{k}\cdot\mathbf{R}_i)| \tag{6.9}$$

For our selected Cc, $Pca2_1$ and $Pmc2_1$ phases, Below, I will analyze the quantities Eqn. (6.7) and Eqn. (6.9) in each of the three found low-energy phases of NNO-film.

6.3.1 Cc phase in its equilibrium region

The Cc phase possesses two order parameters. The first one is the electrical polarization and the second one is the antiphase tilting of oxygen octahedra. Let us denote the x-, y-, and z- components of the polarization as P_x, P_y, and P_z respectively. The polarization is calculated using the Berry phase method. The x-, y-, and z- components of the antiphase tiltings of the oxygen octahedra are denoted as $\omega_{R,x}$, $\omega_{R,y}$, and $\omega_{R,z}$ respectively. The antiphase tilting ω_R at the R-point of the cubic first Brillouin zone located at $\frac{2\pi}{a_{lat}}(\frac{1}{2},\frac{1}{2},\frac{1}{2})$ is calculated by using Eqn. (6.9).

As shown in Fig. 6.2(a), the P_x and P_y components are identical and increase with the increase of the strain. Simultaneously P_z in the same range of the strain is reduced and differs from P_x=P_y. Hence, the polarization is along a [uuv] crystallographic direction and such direction changes with strain; from strain of -4.43% towards [110] with an increase of the strain and reaches [111] direction for nearly vanishing strain. At nearly zero misfit strain total polarization is 0.49 C/m^2. This value is in good agreement with the experimentally measured value of 0.59 C/m^2 at 12K in the $R3c$ phase of NNO bulk [151]. Our computed value of polarization in Cc phase is also in good agreement with computational results of 0.50 and 0.58 C/m^2 reported in Refs. [157] and [158], respectively, for $R3c$ state of NNO bulk. It follows from Figure 6.2(a) as the magnitude of the polarization in this Cc phase almost stays constant as a function of strain. This implies that the polarization is "simply" rotating and not elongating/shrinking during the strain variation.

Figure 6.2(b) displays the tilting of the oxygen octahedra within Cc symmetry for NNO thin film as a function of misfit strain. As consistent with the space group, $\omega_{R,x}$ is equal to $\omega_{R,y}$, but, differs from $\omega_{R,z}$. This tilting pattern can be represented as $a^-a^-c^-$ in Glazer notation [15]. Let us denote, the axis of the oxygen octahedral tilting as $[u'u'v']$. This axis evolves from [001] direction at -4.43% strain and rotates towards [110] direction as strain increases. Such axis of rotation is precisely along the [111] direction for zero misfit strain. And a resulting total angle of rotation being 0.23 radian (12.90°) at 0K at zero misfit strain. This value of angle of rotation is in agreement with the experimental value of 0.17 radian (10°) obtained for the $R3c$ phase of NNO bulk at 123K in Ref. [152]. Moreover, in agreement with my results, the tilting angles are known to increase when cooling down the system [159].

Very interestingly an inflection point for all the Cartesian components of the polarization and $\omega_{\mathbf{R}}$ is observed near a misfit strain of -3%. Such features are signatures of the inherent coupling between electric dipoles and oxygen octahedral tiltings occurring in many perovskites [160].

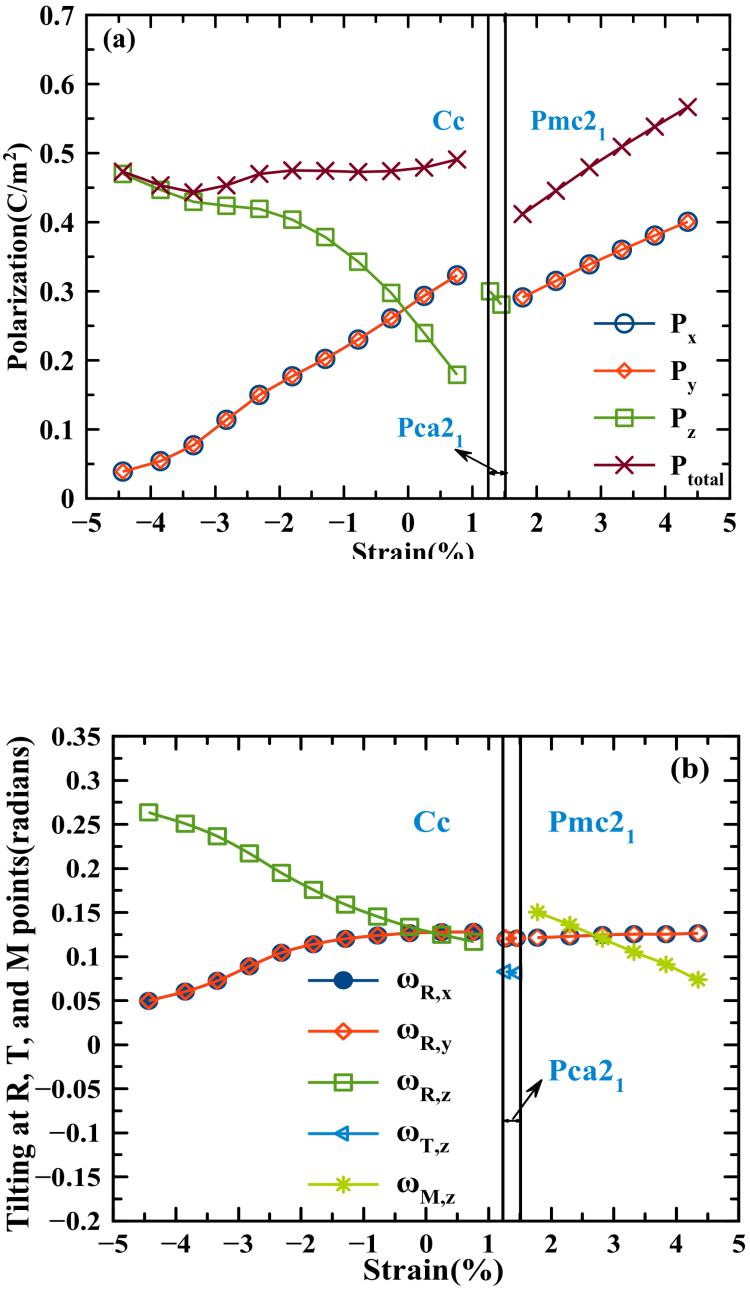

Figure 6.2: Misfit strain dependence of (a) the polarization and (b) oxygen octahedral tilting for the three low-energy phases of epitaxial (001) $NaNbO_3$ thin films.

6.3.2 $Pca2_1$ phase in its equilibrium region

The Cc phase is destabilized at a tensile strain of ≈1.27% via a first-order phase transition to a $Pca2_1$ orthorhombic phase. The latter phase remains stable up to a tensile strain of about 1.70%. For each point of strain, I conducted Fourier transforms of the patterns associated with the local mode displacements (using Eqn. (6.7)) and the oxygen octahedral tiltings [161] to determine which order parameters are associated with this phase. I found that the $Pca2_1$ phase is characterized by four order parameters: (1) the polarization which is along the [001] direction and that is thus fully characterized by P_z; (2) the displacements of the local mode associated with the Δ k-point located at $\frac{\pi}{a}(0, 0, \frac{1}{4})$ in the cubic first Brillouin zone. Such quantities characterize the antiferroelectric (AFE) displacements, for which NNO is famous for [132, 151, 162, 163, 164]. These AFE displacements are along the [110] direction and are denoted as $u_{\Delta,x}$ and $u_{\Delta,y}$. Both $u_{\Delta,x}$ and $u_{\Delta,y}$ are the same in magnitude and are finite, while $u_{\Delta,z}$ is zero. The associated x- or y- components of the local mode displacements have the "–++–" pattern in four subsequent (001) Na planes; (3) the antiphase tilting of oxygen octahedra at R point about the [110] axis and are denoted as $\omega_{R,x}$ and $\omega_{R,y}$; and (4) a more complex tilting at T point located at $\frac{\pi}{a}(\frac{1}{2}, \frac{1}{2}, \frac{1}{4})$ k-point in the cubic first Brillouin zone about the [001] axis. This complex tilting at T point is denoted as $\omega_{T,z}$ along the [001] direction and is determined from Eqn. (6.9). It is found that this complex tilting corresponds to periodic series of '+0-0' when moving along the [001] direction. Hence, the $Pca2_1$ phase is a specific nanoscale twin phase of Refs [8, 114] with a periodicity of 4 lattice constants along z-axis, and adding there a polarization along the same z-axis. The overall tilting pattern of this $Pca2_1$ phase can be expressed in Glazer notation as $a^-a^-c^{complex,4}$, where $c^{complex,4}$ represents the 4-lattice-constant-periodic tilting pattern about the z-axis. As briefly discussed in Ref [142], there is also an energetic coupling of the form

$u_z\ u_x\ \omega_z\ \omega_x$ (and, equivalently, $u_z\ u_y\ \omega_z\ \omega_y$ and $u_x\ u_y\ \omega_x\ \omega_y$). It forces u_z to have a finite value at the Γ-point, because of the existence of u_x (and u_y) at the Δ point, ω_z at the T-point, and ω_x (and ω_y) at the R-point. In agreement with this finding, Ref. [142] shows that the Γ mode is unstable in the *Pbcm* phase of NNO bulk, but it is stable in the $Pca2_1$ phase. This polarization is thus of improper-type but due to a quadra-linear, rather than a trilinear energy, term.

There is a $\simeq 67\%$ increase of the out-of-plane polarization, i.e P_z, when the system undergoes a phase transition from Cc–to–$Pca2_1$ due to the tensile strain (see Figure 6.2(a)). The P_z component is finite while the in-plane polarization is annihilated. As a result, the magnitude of the total polarization decreases from 0.49 C/m^2 in the C_c phase to 0.30 C/m^2 in the $Pca2_1$ state. As shown in Figure 6.3(a), this annihilation of the in-plane polarization favors the emergence of the in-plane antipolar displacements of the local mode at Δ k-point and this antipolar displacement increases with tensile strain. The antiphase oxygen octahedra tilting at R point along the [110] direction and complex tilting at T point along the [001] direction remain nearly constant in $Pca2_1$ phase when changing the strain, as seen in Fig. 6.3(b).

It is also interesting to realize that the energy difference between $Pca2_1$ and Cc phases increases when strengthening the strain above 1.27% as this is seen from Figure 6.1. Such increase in energy difference implies that the energy-storage density can be altered by strain since, the electric field should increase with the strain to make the transition between these two phases.

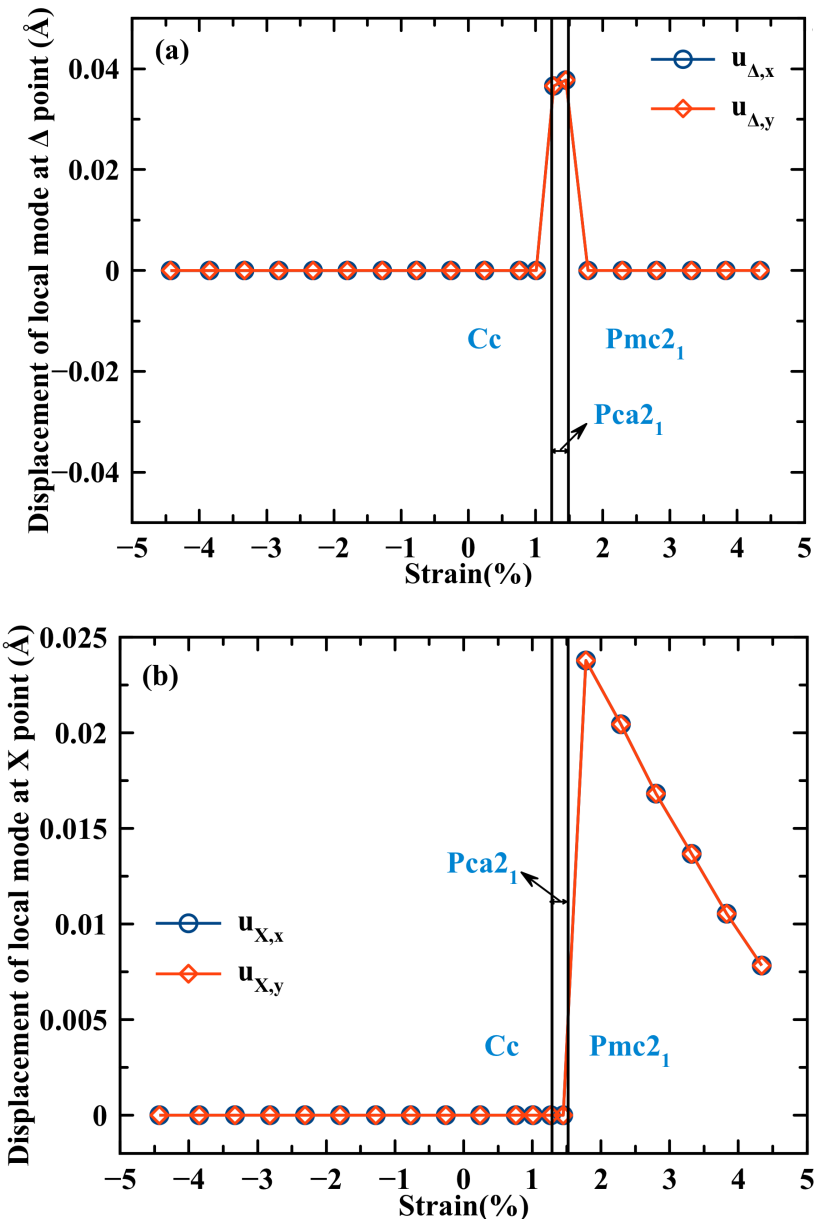

Figure 6.3: Misfit strain dependence of antipolar displacements associated with (a) the Δ and (b) X points of the cubic first Brillouin zone, for the three low energy phases of epitaxial (001) $NaNbO_3$ thin films.

6.3.3 $Pmc2_1$ phase in its equilibrium region

At the tensile strain of ≈1.50%, the $Pca2_1$ state is destabilized in favor of a phase transition to an orthorhombic $Pmc2_1$ phase. From Fourier transform of the local mode displacement and tilting of oxygen octahedra (Eqn. (6.9)), I found that $Pmc2_1$ phase has the following order parameters:

(1) a polarization lying along the [110] direction, and thus having only P_x=P_y finite components; (2) antipolar displacement of the local mode along the [110] direction associated with the X-point located at q=$\frac{\pi}{a}(0, 0, \frac{1}{2})$. These AFE displacements are denoted as $u_{X,x}$ and $u_{X,y}$, and both are equal in magnitude and are finite, while $u_{X,z}$ is null. This AFE displacement pattern is of the type of "+–+–" when moving along [001]; (3) antiphase tilting of oxygen octahedra at R k-point is along the [110] direction. Both $\omega_{R,x} = \omega_{R,y}$ are finite, while $\omega_{R,z}$ is null; and (4) in-phase oxygen octahedral tilting about the z-axis at M k-point i.e $\frac{\pi}{a}(\frac{1}{2}, \frac{1}{2}, 0)$ of the First Brillouin zone, therefore leading to non-zero $\omega_{M,z}$, while $\omega_{M,x} = \omega_{M,y} = 0$. Hence, the overall tilting pattern in $Pmc2_1$ phase is therefore $a^-a^-c^+$ in Glazer notations [15]. This tilting pattern is most commonly found in perovskites having *Pnma* symmetry. Very interestingly, in $Pca2_1$, phase according to Ref. [8], $u_{X,x}$, $\omega_{R,x}$ and $\omega_{M,z}$ are coupled to each other by a trilinear energy coupling. In $Pmc2_1$ phase, such coupling also exists, but, as I mentioned above, it has another, quadrolinear coupling leading to the finite polarization.

Figure 6.2(a) reveals that the phase transition from $Pca2_1$-to-$Pmc2_1$ is of first-order. In line with this fact, the in-plane polarization at this phase transition jumps and the out-of-plane polarization abruptly vanishes, as this is seen from Figure 6.2. Note that the in-plane polarization increases with the increase of the tensile strain and that Figure 6.3(b) shows that $u_{X,x}$=$u_{X,y}$ decreases from 0.023Å to 0.007Å when the tensile strain increases from 1.50% to +4.43% within $Pmc2_1$ phase.

Let us now compare the computed results in the $Pmc2_1$ phase with the experimental study done by H. Shimizu *et al.* [157]. The P-E loops of the x$CaZrO_3$-(1-x)$NaNbO_3$ (CZNN) ceramics at 120°C and zero electric fields gave a value of the polarization of about 0.40 C/m^2 for x=0, which is remarkably close to our predicted value of 0.41 C/m^2 at 1.80% tensile strain. This value of polarization i.e. 0.41 C/m^2 also agrees well with the DFT value of 0.47 C/m^2 obtained in

the generalized gradient approximation for the $P2_1ma$ phase (which is the $Pmc2_1$ phase in our calculations) of bulk NNO bulk.

As shown in Fig. 6.2(b), in $Pmc2_1$ phase, the anti-phase oxygen octahedral tilting quantified by $\omega_{R,x} = \omega_{R,y}$ is independent on the strain, while the in-phase tilting (characterized by $\omega_{M,z}$) decreases with strain. The latter decrease of the in-phase tilting can be due to two effects: (1) polarization and tiltings tend to compete [80] and as a result, the strain-induced polarization increases suppressing the oxygen octahedral tiltings (see Figure 6.2(a)) and (2) the AFE displacements associated with the X-point are trilinearly coupled with the antiphase and in-phase tiltings [8]. Therefore, the decrease of $u_{X,x}$ and $u_{X,y}$ with strain tends to decrease oxygen octahedral tiltings.

6.4 Conclusion

In summary, first-principles calculations were conducted to predict the existence of three different ground states in epitaxial (001) NNO films, depending on the misfit strain these films experience. These three states have monoclinic Cc, orthorhombic $Pca2_1$ and orthorhombic $Pmc2_1$ symmetry, respectively, and each exhibits a different direction for their electrical polarization, as well as, a different tilting pattern. The $Pca2_1$ and $Pmc2_1$ states also possess different antiferroelectric displacements. These features, as well as the reported strain-induced control of ferroelectric, antiferrodistortive and antiferroelectric properties within these three states, are promising to design NNO films with desired characteristics, via strain-engineering.

Chapter 7

CONCLUSION

In the first part of dissertation, an elemental atomistic energy has been investigated, which naturally explains a variety of structurally complex ABO_3 perovskites. This energy bilinearly couples the antiferroelectric displacement patterns of cations with the rotations of the oxygen octahedra. The proposed mechanism drives structural instability that is hybrid in nature, in the sense that it combines the (anti)polar (antiferroelectric) and octahedral-rotational dynamical modes. Analytical derivations from this atomistic energy explain the existence of of the very complex crystal structure of $PbZrO_3$ and some other antiferroelectrics. In the second part of the dissertation, the dynamics of the antipolar distortion in $BiFeO_3$ under hydrostatic pressure is reported. The numerical and analytical studies of this system found that, at high temperatures, this system undergoes a phase transition from the paraelectric cubic $Pm\bar{3}m$ state to intermediate $P4/mbm$ state followed by $Pnma$ phase at lower temperatures. This study reveals that the AFE modes have very high resonant frequencies which are almost independent of the temperature in the $Pm\bar{3}m$ phase, but, in $P4/mbm$ and $Pnma$ phases, these AFE modes are soft. The softening of the AFE modes is due to a very specific dynamical mixing of the antipolar distortion with octahedral oxygen tiltings. Such mixing increases the number of the peaks of the antipolar phonon modes, when the system passes through $Pm\bar{3}m$-$P4/mbm$-$Pnma$ phase transition sequence. A simple model developed revealed that the number of the phonon peaks increases due to the trilinear energy coupling between the anti-polar motion and in-phase and anti-phase tiltings. In the third part of the dissertation, the temperature dependence of the phonon frequencies in $(BFO)_1/(NFO)_1$ SL is studied. It undergoes a phase transition from tetragonal $P4/mmm$ paraelectric state at high

temperatures to a low temperature polar $Pmc2_1$ phase. In the high-temperature $P4/mmm$ state, all polar and antipolar phonon modes are hard, while most of them abruptly become soft in $Pmc2_1$ phase at transition temperature. The softening of these modes is due to the very specific trilinear energetic coupling of the soft oxygen octahedral tilting modes with polar and antipolar distortions. Because of such mixing, the number of the peaks in each phonon modes possessing polar, antipolar, and antiferrodistortive distortions increases, when system passes through a phase transition. The behavior of the polar modes is different in the high- and low-temperature intervals which renders that hybrid improper ferroelectrics are dramatically different from proper ferroelectrics. In the last part of the dissertation, first-principles calculations were conducted to predict the existence of three different ground states in epitaxial (001) NNO films as a function of misfit strain. These three ground states are: (1) monoclinic Cc phase, (2) orthorhombic $Pca2_1$ phase, and (3) orthorhombic $Pmc2_1$ phase. Each of these phases exhibits different electrical polarization and tilting pattern. The $Pca2_1$ and $Pmc2_1$ states exhibits different antiferroelectric displacements. The strain-induced control of the ferroelectric, antiferrodistortive and antiferroelectric properties of these three states are promising to design NNO films with desired characteristics, via strain-engineering. The results obtained here are published in Ref. [165].

Bibliography

[1] N. A. Benedek and C. J. Fennie, Phys. Rev. Lett. **106**, 107204, (2011).

[2] J. M. Rondinelli and C. J. Fennie, Adv. Mater. **24**, 1961 (2012).

[3] B. Xu, D. Wang, HJ. Zhao, J. X.M. Chen, and L. Bellaiche, Adv. Funct. Mater. **25**, 3626 (2015).

[4] A. T. Mulder, N. A. Benedek, J. M. Rondinelli, and C. J. Fennie, Adv. Funct. Mater. **23**, 4810 (2013).

[5] Z. Zanolli, J. C. Wojdel, J. Íñiguez, and P. Ghosez, Phys. Rev. B. **88**, 060102(R) (2013).

[6] E. Bouqent et. Al., Nature. **452**, 732 (2008).

[7] H. J. Zhao, J. Iniguez, W. Ren, X. M. Chen, and L. Bellaiche, Phys. Rev. B. **89**, 174101 (2014).

[8] L. Bellaiche and J. Íñiguez, Phys. Rev. B. **88**, 014104 (2013).

[9] B. Xu, C. Paillard, B. Dkhil, and L. Bellaiche, Phys. Rev. B. **94**, 140101 (2016).

[10] B. Xu, J. Iniguez, and L. Bellaiche, Nat. Comm. **8**, 15682 (2017).

[11] K. M. Rabe, Antiferroelectricity in Oxides: A Reexamination, in Functional (eds Ogale, S. B., Venkatesan, T. V. and Blamire, M. G.) (Wiley –VCH Verlag GmbH and Co. KGaA, 2013).

[12] B. Ma, D. –K. Kwon, M. Narayanan, and U. Balachandran, J. Mater. Res. **24**, 2993 (2009).

[13] M. H. Park, et al. Adv. Energy Mater. **4**, 1400610 (2014).

[14] B. Wul and I. M. Goldman, C. R. Acad. Sci. URSS. **46**, 139; **49**, 177 (1945).

[15] A. M. Glazer, Acta Cryst., Sect. B: Struct. Cryst. Chem. **28**, 3384 (1972).

[16] L. D. Landau., Phys. Z. SowjUn, **11**, 26, (1937); L. D. Landau, and E. M. Lieshitz., Statistical Physics, Pergamon, London, (1959).

[17] R. A. Cowley, Adv. Phys. **29**, 1 (1980).

[18] A. F. Devonshire, (1949), Phil. Mag. **40**, 1040; Adv. Phys. **3**, 85, (1954).

[19] V. L. Ginzburg, Soviet Physics-Solid State, 2(9):1824 (1961)

[20] V. L. Ginzburg and V. L. Ginzburgm, Fiz. Tverd. Tela, 2(9):2031 (1960).

[21] L. Davidovich Landau and Evgenii Mikhailovich Lifshitz. Statistical physics. Course of theoretical physics. Pergamon, London, 2nd edition, 1968. Trans. from the Russian. Available from: http://cds.cern.ch/record/101802.

[22] A. P. Levanyuk, Sov. Phys. JETP, **9**, 571 (1959).

[23] K.M. Rabe, C.H. Ahn, and J.M. Triscone. Physics of Ferroelectrics: A Modern Perspective. Topics in Applied Physics. Springer Berlin Heidelberg, 2007. Available from: https://books.google.fr/books?id=-QhVI8JTvwwC.

[24] B. A. Strukov and A. P. Levanyuk. Ferroelectric phenomena in crystals: physical foundations. Springer Science and amp; Business Media, (2012).

[25] S. W. Cheong and M. Mostovoy, Nature Materials. **6**, 13 (2007).

[26] A. P. Levanyuk and D. G. Sannikov, Soviet Physics Uspekhi. vol. **17**, 199 (1974).

[27] K. Aizu, J. Phys. Soc. Jpn. **35**, 1704 (1973).

[28] B. Van Aken, T. Palstra, A. Filippetti, and N. Spaldin, Nat. Mater. **3**, 164 (2004).

[29] Z. Huang, Y. Cao, Y. Sun, Y. Xue, and C. Chu, Phys. Rev. B. **56**, 2623 (1997).

[30] B. Jaffe, P Ire **49** (8), 1264 (1961).

[31] X. Hao, J. Adv. Dielectr. **3**, 1330001 (2013).

[32] B. Ma, M. Narayanan, and U. Balachandran, Mater. Lett. **63**, 1353 (2009).

[33] X. Hao, Y. Wang, L. Zhang, and S. An, Appl. Phys. Lett. **102**, 163903 (2013).

[34] B. Peng, Q. Zhang, X. Li, T. Sun, H. Fan, S. Ke, M. Ye, Y. Wang, W. Lu, H.Niu, J.F.Scott, X.Zeng, and H.Huang, Adv. Electron. Mater. **1**, 1500052 (2015).

[35] E. Sawaguchi, G. Shirane, and Y. Takagi, J. Phys. Soc. Jpn. **6**, 333 (1951).

[36] G. Shirane, E. Sawaguchi, and Y. Takagi, Phys. Rev. **84**, 476 (1951).

[37] G. Shirane, Phys. Rev. **86**, 219 (1952).

[38] J. Iniguez, M. Stengel, S. Prosandeev, and L. Bellaiche, Phys. Rev. B. **90**, 220103(R) (2014).

[39] S. Prosandeev, C. Xu, R. Faye, W. Duan, H. Liu, B. Dkhil, P.-E. Janolin, J. Iniguez, and L. Bellaiche, Phys. Rev. B. **89**, 214111 (2014).

[40] J. Hlinka, T. Ostapchuk, E. Buixaderas, C. Kadlec, P. Kuzel, I. Gregora, J. Kroupa, M. Savinov, A. Klic, J. Drahokoupil, I. Etxebarria, and J. Dec, Phys. Rev. Lett. **112**, 197601 (2014).

[41] E. Cockayne and K. M. Rabe, J. Phys. Chem. Solids. **61**, 305 (2000).

[42] A. K. Tagantsev, K. Vaideeswaran, S. B. Vakhrushev, A. V. Filimonov, R. G. Burkovsky, A. Shaganov, D. Andronikova, A. I. Rudskoy, A. Q. R. Baron, H. Uchiyama, D. Chernyshov, A. Bosak, Z. Ujma, K. Roleder, A. Majchrowski, J.-H. Ko, and N. Setter, Nat. Comm. **4**, 2229 (2013).

[43] B. K. Mani, S. Lisenkov, and I. Ponomareva, Phys. Rev. B. **91**, 134112 (2015).

[44] K. Patel, S. Prosandeev, Y. Yang, B. Xu, J. Iniguez, and L. Bellaiche, Phys. Rev. B. **94**, 054107 (2016).

[45] J. Buhot, C. Toulouse, Y. Gallais, A. Sacuto, R. de Sousa, D. Wang, L. Bellaiche, M. Bibes, A. Barthelemy, A. Forget, D. Colson, M. Cazayous, and M-A. Measson, Phys. Rev. Lett. **115**, 267204 (2015).

[46] M. Guennou, P. Bouvier, G. Chen, B. Dkhil, R. Haumont, G. Garbarino, and J. Kreisel, Phys. Rev. B. **84**, 174107 (2011).

[47] S. Gomez-Salces, F. Aguado, F. Rodrigues, R. Valiente, J. Gonzalez, R. Haumont R and J. Kreisel, Phys. Rev. B. **85**, 144109 (2012).

[48] K. Patel, S. Prosandeev, and L. Bellaiche, npj computational materials **3**, 34 (2017).

[49] M. Stengel, C. J. Fennie, and P. Ghosez, Phys. Rev. B. **86**, 094112 (2012).

[50] K. Patel, S. Prosandeev, B. Xu, and L. Bellaiche, Phys. Rev. B. **100**, 214107 (2019).

[51] J. H. Haeni, P. Irvin, W. Chang, et al., Nature **430**, 758 (2004).

[52] K. J. Choi, M. Biegalski, Y. L. Li, et al., Science **306**, 1005 (2004).

[53] I. Lefkowitz, K. Lukaszewicz, and H. D. Megaw, Acta Cryst. **20**, 670 (1966).

[54] L. A. Reznichenko, L. A. Shilkina, E. S. Gagarina, I. P. Raevskii, E. A. Dul'kin, E. M. Kuznetsova, and V. V. Akhnazarova, Cryst. Rep. **48**, 448 (2003).

[55] L. M. Chao, Y. D. Hou, M. P. Zheng, andM. K. Zhu, Appl. Phys. Lett. **108**, 212902 (2016).

[56] Yu. I. Yuzyuk, P. Simon, E. Gagarina, L. Hennet, D. Thiauduere, et al., J. Phys. Condens. Matter **17**, 4977 (2005).

[57] T. Saito, H. Adachi, T. Wada, and H. Adachi, Jpn. J. Appl. Phys. Part 1 **44**, 6969 (2005).

[58] T. Mino, S. Kuwajima, T. Suzuki, I. Kanno, K. Kotera, and K. Wasa, Jpn. J. Appl. Phys. Part 1 **46**, 6960 (2007).

[59] W. Kohn, Nobel Lecture, 1253 (1998).

[60] P. Hohenberg and W. Kohn, Phys. Rev. **136** (3B), B864 (1964).

[61] P. Hohenberg and W. Kohn, Phys. Rev. **136**, B864 (1964).

[62] W. Kohn and L. J. Sham, Phys. Rev. **140**, A1133 (1965).

[63] M. C. Payne, et. al., Rev. Mod. Phys. **64**,1045 (1992).

[64] A. D. Becke, Phys. Rev. A. **38**, 3098 (1988).

[65] C. Lee, W. Yang, and R. G. Parr, Phys. Rev. B. **37**, 785 (1988).

[66] J. P. Perdew, K. Burke, and M. Ernzerhof, Phys. Rev. Lett. **77**, 3865 (1996).

[67] J. P. Perdew, K. Burke, and M. Ernzerhof, Phys. Rev. Lett. **78**, 1396 (1997).

[68] R. Martin, Electronic Structure: Basic Theory and Practical Methods (Cambridge University Press, 2004).

[69] J. P. Perdew, A. Ruzsinszky, G. I. Csonka, O. A. Vydrov, G. E. Scuseria, L. A. Constantin, X. Zhou, and K. Burke, Phys. Rev. Lett. **100**, 136406, (2008).

[70] P. Haas, F. Tran, and P. Blaha, Phys. Rev. B. **79**, 085104, (2009).

[71] P. Haas, F. Tran, and P. Blaha, Phys. Rev. B. **79**, 209902, (2009).

[72] G. I. Csonka, J. P. Perdew, A. Ruzsinszky, P. H. T. Philipsen, S. Lebègue, J. Paier, O. A. Vydrov, and J. G. Ángyán, Phys. Rev. B **79**, 155107 (2009).

[73] J. Sun, M. Marsman, G. I. Csonka, A. Ruzsinszky, P. Hao, Y. S. Kim, G. Kresse, and J. P. Perdew, Phys. Rev. B. **84**, 035117 (2011).

[74] L. Schimka, J. Harl, and G. J. Kresse, Chem. Phys. **134**, 024116 (2011).

[75] R. D. King-Smith, and D. Vanderbilt, Phys. Rev. B. **47**, 1651, (1993).

[76] D. G. Schlom, L.-Q. Chen, C.-B. Eom, K. M. Rabe, S. K. Streiffer and J.-M. Triscone, Annu. Rev. Mater. Res. **37**, 589 (2007).

[77] W. Zhong, D. Vanderbilt, and K. Rabe, Phys. Rev. Lett. **73**, 1861 (1994).

[78] W. Zhong, D. Vanderbilt, and K. Rabe, Phys. Rev. Lett. **52**, 6301 (1995).

[79] N. W. Ashcroft and N. D. Mermin. Solid State Phsyics. Suanders College Publishing, 1967.

[80] I. A. Kornev, L. Bellaiche, P. E. Janolin, B. Dkhil, and E. Suard, Phys. Rev. Lett. **97**, 157601 (2006).

[81] J. B. Neaton, C. Ederer, U. V. Waghmare, N. A. Spaldin, and K. M. Rabe, Phys. Rev. B **71**, 014113 (2005).

[82] P. Fischer, M. Polomska, I. Sosnowska, and M. Szymanski, J. Phys. C: Solid St. Phys. **13**, 1931 (1980).

[83] D. Rahmedov, D. Wang, J. Íñiguez, and L. Bellaiche, Phys. Rev. Lett. **109**, 037207 (2012).

[84] H. J. Zhao, W. Ren, Y. Yang, J. Iñiguez, X. M. Chen, and L. Bellaiche, Nature Communications **5**, 4021 (2014).

[85] Y. Yang, J. Iñiguez, A.-J. Mao, and L. Bellaiche, Phys. Rev. Lett. **112**, 057202 (2014).

[86] D. L. Corker, A. M. Glazer, W. Kaminsky, R. W. Whatmore, J. Dec, and K. Roleder, Acta Cryst. B. **54**, 18 (1998).

[87] S. A. Prosandeev, D. D. Khalyavin, I. P. Raevski, A. N. Salak, N. M. Olekhnovich, A. V. Pushkarev, and Y. V. Radyush, Phys. Rev. B. **90**, 054110 (2014).

[88] D. D. Khalyavin, A. N. Salak, N. M. Olekhnovich, A. V. Pushkarev, Yu. V. Radyush, P. Manuel, I. P. Raevski, M. L. Zheludkevich, and M. G. S. Ferreira, Phys. Rev. B. **89**, 174414 (2014).

[89] Y. Zhu, , R.L. Withers, L. Bourgeois, C. Dwyer, and J. Etheridge, Nat. Mat. **14**, 1142 (2015).

[90] Ph. Ghosez, E. Cockayne, U. V. Waghmare, and K. M. Rabe, Phys. Rev. B. **60**, 836 (1999).

[91] G. Baldinozzi, Ph. Sciau, and A. Bulou, J. Phys. Condens Matter. **9**, 10531 (1997).

[92] G. Baldinozzi, D. Grebille, Ph. Sciau, J-M. Kiat, J. Moret, and J-F. Bérar., Acta Cryst. B **56**, 570 (2000).

[93] V. Heine, and J. D. C. McConnell, J. Phys. C: Solid State Phys. **17**, 1199 (1984).

[94] L. D. Landau and E. M. Lifshitz, Course of theoretical physics, Vol. 5, Statistical Physics, Part 1, Pergamon Press, Oxford, 1980.

[95] A. P. Levanuyk, and D. G. Sannikov, Fiz. Tverd. Tela. **18**, 423 (1976).

[96] P. Goudochnikov and A. J. Bell, J. Phys. Condens Matter. **19**, 176201 (2007).

[97] V. Yu, Topolov, E. S. Gagarina, and V. V. Demidova, Ferroelectrics. **172**, 373 (1995).

[98] S. Prosandeev, D. Wang, W. Ren, J. Íñiguez, and L. Bellaiche, Adv. Funct. Mater. **23**, 234 (2013).

[99] W. Zhong, D. Vanderbilt, and K.M. Rabe, Phys. Rev. B **52**, 6301 (1995).

[100] K. Patel, S. Prosandeev, Y. Yang, B. Xu, J. Íñiguez, and L. Bellaiche, Phys. Rev. B **94**, 054107 (2016).

[101] J. Varignon, N. C. Bristowe, and P. Ghosez, Phys. Rev. Lett. **116**, 057602 (2016).

[102] J. Varignon, N. C. Bristowe, E. EBouqent and P. Ghosez. Sci. Rep. **5**, 15364 (2015).

[103] K. M. Rabe. *Functional Metal Oxides*, edited by S. B. Ogale, T. V. Venkatesan, and M. Blamire. (Wiley, New York, 2013).

[104] B. Ma, D. K. Kwon, M. Narayanan, and U. (Balu) Balachandran J. Mater. Res. **24**, 2993 (2009).

[105] Ma. B., M. Narayanan, and U. (Bala) Balachandran, Mater. Lett. **63**, 1353 (2009).

[106] X. Hao, Y. Wang, L. Zhang, L. Zhang, and S. An, S. Appl. Phys. Lett. **102**, 163903 (2013).

[107] B. Chu, X. Zhou, K. Ren, B. Neese, M. Lin, Q. Wang, F. Bauer, and QM. Zhang, Sci. **313** , 334 (2006).

[108] T. M. Correia, M. McMillen, M. Rokosz, and M. G. Cain, J. Am. Ceram. Soc. **96**, 2699 (2013).

[109] B. Peng, Q. Zhang. X. Li, T. Sun, H. Fan, S. Ke, M. Ye, Y. Wang, W. Lu, H. Niu, J. F. Scott, X. Zeng, and H. Huang, Adv. Electron. Mater. **1**, 1500052 (2015).

[110] M. H. Park, H. J. Kim, Y. J. Kim, T. Moon, K. D. Kim, and C. S. Hwang., Adv. Energy Mater. **4**, 1400610 (2014).

[111] D. Albrecht, S. Lisenkov, W. Ren, D. Rahmedov, I. A. Kornev, and L. Bellaiche, Phys. Rev. B **81**, 140401 (2010).

[112] I. A. Kornet, S. Lisenkov, R. Haumont, B. Dkhil, and L. Bellaiche, Phys. Rev. Lett. **99**, 227602 (2007).

[113] S. Lisenkov, I. A. Kornev, and L. Bellaiche, Phys. Rev. B. **79**, 012101 (2009).

[114] S. Prosandeev, D. Wang, W. Ren, J. Iniguez, and L. Bellaiche, Adv. Funct. Mater. **23**, 234, (2013).

[115] W. Zhong, D. Vanderbilt, and K. M. Rabe, Phys. Rev. Lett. **73**, 1861 (1994); W. Zhong, D. Vanderbilt, and K. M. Rabe, Phys. Rev. B. **52**, 6301 (1995).

[116] Note that comparisons between computations and measurements conducted in Ref. [45] imply that this simulated pressure likely corresponds to an experimental pressure of about 8.2GPa, probably because of the typical underestimation of the lattice constant by first-principles techniques and to correct for the fact that the parameters of the effective Hamiltonian of BFO were all determined from *ab-initio* calculations at an atmospheric pressure.

[117] D. Wang, J. Weerasinghe, and L. Bellaiche, Phys. Rev. Lett. **109**, 067203 (2012).

[118] J. Weerasinghe, D. Wang, and L. Bellaiche, Phys. Rev. B **85**, 014301 (2012).

[119] D. Wang, J. Hlinka, A. A. Bokov, Z.-G. Ye, P. Ondrejkovic, J. Petzelt, and L. Bellaiche, Nature communication DOI: 10.1038/ncomms6100

[120] I. Ponomareva, L. Bellaiche, T. Ostapchuk, J. Hlinka, and J. Petzelt, Phys. Rev. B. **77**, 012102 (2008).

[121] A. Al-Zein, J. Jlinka, J. Rouquette, and B. Hehlen, Phys. Rev. Lett. **105**, 017601 (2010).

[122] C. J. Howard and H. T. Stokes, Acta Cryst. **B54**, 782 (1998).

[123] K. Patel, S. Prosandeev, and L. Bellaiche, npj Computational Materials 3, **34** (2017); doi: 10.1038/s41524-017-0033 (Nature).

[124] H. J. Zhao, W. Ren, Y. Yang, J. Iñiguez, X. M. Chen, L. Bellaiche, Nat. Commun. **5** 4021 (2014).

[125] J. Young and J. M. Rondinelli, Chem. Mater. **25**, 4545 (2013).

[126] A. P. Levanyuk and D. G. Sannikov, Usp. Fiz. Nauk. **112**, 561 (1974).

[127] W. Kaczmarek and F. Gervaid, Ferroelectrics. **80**, 197 (1988).

[128] K. Patel, S. Prosandeev, B. Xu, and L. Bellaiche, Phys. Rev. B, **100**, 212107 (2019).

[129] M. E. Lines and A. M. Glass, Principles and Applications of Ferroelectrics and Related Materials (Clarendon Press, Oxford, 1977).

[130] B. T. Matthias and J. P. Remeika, Phys. Rev. **82**, 727 (1951).

[131] P. Vousden, Acta Cryst. **4**, 545 (1951).

[132] L. E. Cross and B. J. Nicholson, Phil Mag. **46**, 453 (1955).

[133] C. N. W. Darlington and H. D. Megaw, Acta Cryst. **B29**, 2171 (1973).

[134] L. Jiang, D. C. Mitchell, W. Dmowski, and T. Egami, Phys. Rev. B. **88**, 014105 (2013).

[135] K. E. Johnston, C. C. Tang, J. E. Parker, K. S. Knight, P. Lightfoot, and S. E. Ashbrook, J. Am. Chem. Soc. **132**, 8732 (2010).

[136] A. C. Sakowski-Cowley, K. Lukaszewicz, and H. D. Megaw, Act. Cryst. **B25**, 851 (1969).

[137] S. I. Raevskaya, M. A. Malitskaya, C-C. Chou, A. G. Lutokhin, I. P. Raevski, and V. V. Titov, Physica Status Solidi a, **22**,1800972 (2019).

[138] C. I. Cheon, H. W. Joo, K.-W. Chae, J. S. Kim, S. H. Lee, S. Torii and T. Kamiyama, Materials Letters. **156**, 214 (2015).

[139] Y. Shiratori, A. Magrez, J. Dornseiffer, F. H. Haegel, C. Pithan, and R. Waser, J. Phys. Chem. B **109**, 20122 (2005).

[140] J. Schwarzkopf, M. Schmiedbarer, T. Remmelo, A. Duk, A. Kwasniewski, S. B. Anooz, A. Devi, and R. Fornari, J. Appl. Cryst. **45**, 1015 (2012).

[141] M. Chandrasekhar and S. P. Kumar, Physica B: Condensed Matter. **497**, 59 (2016).

[142] Y. Yang, B. Xu, C. Xu, W. Ren, and L. Bellaiche, Phys. Rev B. **97**, 174106 (2018).

[143] J.H.Haeni., et. al., Nature **430**, 758 (2004).

[144] Y. I. Yuzyuk, R. A. Shakhovoy, S. I. Raevskaya, I. P. Raevski, M. El Marssi, M. G. Karkut, and P. Simon, Appl. Phys. Lett. **96**, 222904 (2010).

[145] R. A. Shakhovoy, S. I. Raevskaya, L. A. Shakhovaya, D. V. Suzdalev, I. P. Raevski, Yu. I. Yuzyuk, A. F. Semenchev and M. El Marssi, J. of Raman Spectrosc. **43**, 1141 (2012).

[146] O. Diéguez, K. M. Rabe, and D. Vanderbilt, Phys. Rev. B. **72**, 144101 (2005).

[147] G. Kresse and J. Hafner, Phys. Rev. B. **47**, 558 (1993); G. Kresse and J. Furthmuller, Phys. Rev. B. **54**, 11 169 (1996).

[148] G. Kresse and D. Joubert, Phys. Rev. B. **59**, 1758 (1999).

[149] P. E. Blochl, Phys. Rev. B **50**, 17953 (1994).

[150] J. P. Perdew, A. Ruzsinszky, G. I. Csonka, O. A. Vydrov, G. E. Scuseria, L. A. Constantin, X. Zhou, and K. Burke, Phys. Rev. Lett. **100**, 136406 (2008).

[151] S. K. Mishra, N. Choudhury, S. L. Chaplot, P. S. R. Krishna, and R. Mittal, Phys. Rev. B. **76**, 023110 (2007).

[152] C. N. W. Darlington and H. D. Megaw, Acta Crystallogr. **B29**, 2171 (1973).

[153] R. Von der Mühll, A. Sadel, and P. Hagenmuller, J. Solid State Chem. **51**, 176 (1984).

[154] R. Resta, Rev. Mod. Phys. **66** 809 (1994).

[155] T. Saito, T. Wada, H. Adachi, and I. Kanno, Jpn. J. of Appl. Phys. **43**, 6627 (2004).

[156] R. D. King-Smith and David Vanderbilt, Phys. Rev. B. **49**, 5828, (1994).

[157] H. Shimizu, H. Guo, S. E. Reyes-Lillo, Y. Mizuno, K. M. Rabe and C. A. Randall, Dalton Trans. **44**, 10763 (2015).

[158] Dissertation of S. E. R. Lillo, "First Principles Study of Antiferroelectric Oxide Crystals".

[159] B. Xu, D. Wang, J. Iniquez, and L. Bellaiche, Adv. Func. Mater. **25**, 552 (2014).

[160] I. A. Kornev and L. Bellaiche, Phys. Rev. B. **79**, 100105 (R) (2009).

[161] A.M. George, J. Iniguez and L. Bellaiche, Phys. Rev. B. **65**, 180301(R) (2002).

[162] L. E. Cross, Nature. **181**, 178 (1958).

[163] I. Lefkowitz, K. Lukaszewicz, H. D. Megaw, Acta Cryst. **20**, 670 (1966).

[164] G. Shirane, R. Newnham, R. Pepinsky, Phys Rev. **96**, 581 (1954).

[165] K. Patel, S. Prosandeev, B. Xu, C. Xu, and L. Bellaiche, Phys. Rev. B, **103**, 094103 (2021).

Appendix

Appendix A

EFFECTIVE HAMILTONIAN PARAMETERS USED IN THIS DISSERTATION

The parameters which are related to the structural energies (E^{FE} and E^{AFD}) terms in the effective Hamiltonian explained in detail in Chapters 4 and 5 are listed in Table A1 for $BiFeO_3$ (BFO) and $(BiFeO_3)_1/(NdFeO_3)_1$ ($(BFO)_1/(NFO)_1$).

Table A.1: Expansion parameters of the effective Hamiltonian for $BiFeO_3$ and $(BiFeO_3)_1/(NdFeO_3)_1$. Energies are in hartrees and the reference cubic lattice parameter is 7.02200 Bohr.

Dipole	Z^*	5.868	ϵ_∞	7.164		
u on-site	κ_2	-0.00244873	α	0.02651	γ	0.007373
u short	j_1	-0.008794	j_2	0.012442		
	j_3	0.000684	j_4	-0.0021228	j_5	0.006948
	j_6	0.0010992	j_7	0.0005496		
Elastic	B_{11}	3.585	B_{12}	2.899	B_{44}	1.151
$u\eta_l$ coup.	B_{1xx}	-0.49379	B_{1yy}	-0.23606	B_{4yz}	-0.05358
ω on-site	κ_A	-0.25103	α_A	4.48968	γ_A	-2.29697
ω short	k_1	0.06296	k_2	0.00210	$D^{'}$	-0.159
$\omega\eta_l$ coup.	C_{1xx}	-1.13197	C_{1yy}	-0.12311	C_{4yz}	1.90
ωu coup. ($(BFO)_1/(NFO)_1$)	$\kappa^{Bi}_{ij,xy}$	-0.008	$\kappa^{Nd}_{ij,xy}$	-0.0136		
ωu coup. (BFO)	$D_{ij,xy}$	-0.008				
ωu coup. (bi-quadratic)	E_{xxxx}	0.10554	E_{xxyy}	0.12165	E_{xyxy}	-0.2882
$uu(alloy)$	$\Delta\kappa_u$	0.100				

The analytical expressions for E^{FE} and E^{AFD} were provided in chapters 2, 4, and 5.

Appendix B

BERRY PHASE METHOD TO CALCULATE THE POLARIZATION

This appendix is aimed at providing details about the Berry Phase Method [75, 154] used to calculate the polarization for Cc, $Pca2_1$, and $Pmc2_1$ phases of $NaNbO_3$ thin films.

The polarization is calculated by using Berry phase method. We calculated the differences in polarization between the cubic (λ = 0) and polar phases (λ=1) for NNO thin films. Here, λ is the parameter characterizing the symmetry of the structure, λ =0 corresponds to paraelectric symmetry while λ=1 represents the polar symmetry. Particular attention was paid to have the Berry-phase values onto the same branch of the polarization lattice, by calculating the polarization for a number of intermediate structures along the deformation path between the cubic and polar structures. The calculated polarization branches as a function of the distortion amplitude from the high-symmetry structure i.e. cubic to the lower-in-symmetry polar phase are plotted to find a smooth path connecting the two structures.

The results are shown in Fig. S1 for Cc phase for polarization along the z direction at -0.26% compressive strain. For the specific continuous path connecting the cubic-lattice point corresponding to 0.27 C/m^2 (ΔP = P(λ=1)-P(λ=0)) with the Cc lattice point of -0.036 C/m^2, the polarization is seen to evolve smoothly. Subtracting the two end-point values gives a polarization change of 0.30 C/m^2. This value of polarization along the z direction is same as obtained at nearly zero strain for Cc phase. Similarly we conducted calculations of polarization for the $Pca2_1$ and $Pmc2_1$ phases. As shown in Figs. S2 and S3, other polarization evolves smoothly from λ = 0 to λ = 1 for $Pca2_1$ and $Pmc2_1$ phases, respectively. In the $Pca2_1$ phase at a tensile strain of 1.27%, the corresponding value of polarization P_z is 0.30 C/m^2, while the value of polarization in the

$Pmc2_1$ phase at 2.82% tensile strain is about 0.33 C/m^2.

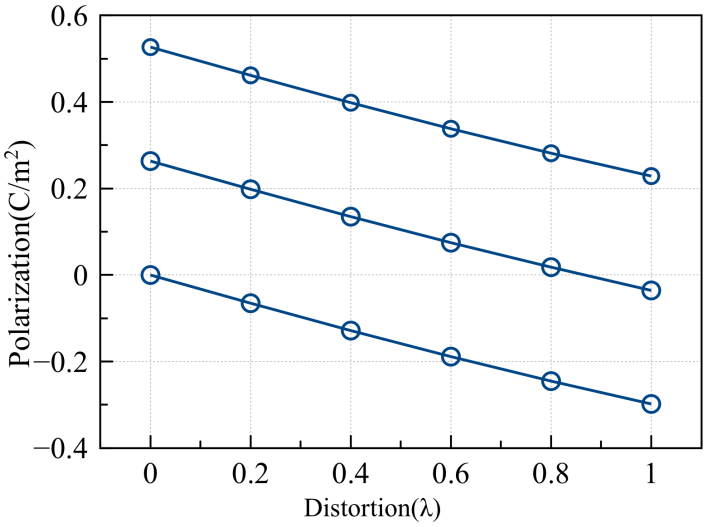

Figure B.1: The z component of polarization as a function of lattice distortion for Cc phase at compressive strain of -0.26% in the NNO thin film.

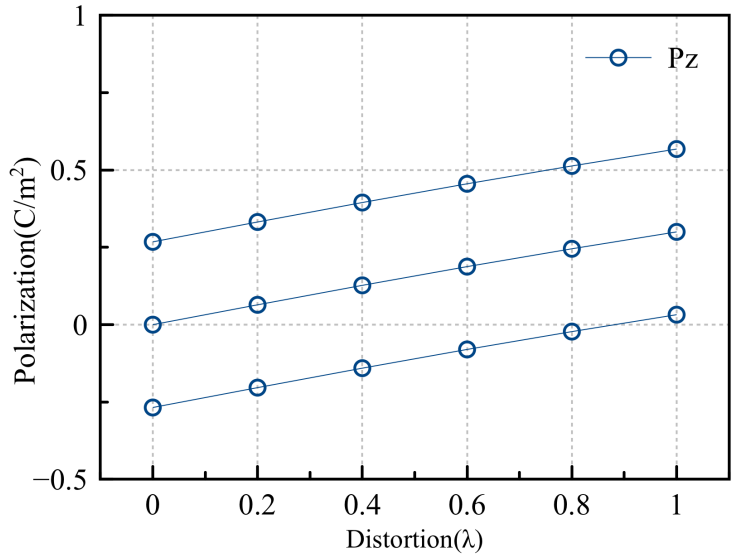

Figure B.2: The z component of polarization as a function of lattice distortion for $Pca2_1$ phase at tensile strain of 1.27% in the NNO thin film.

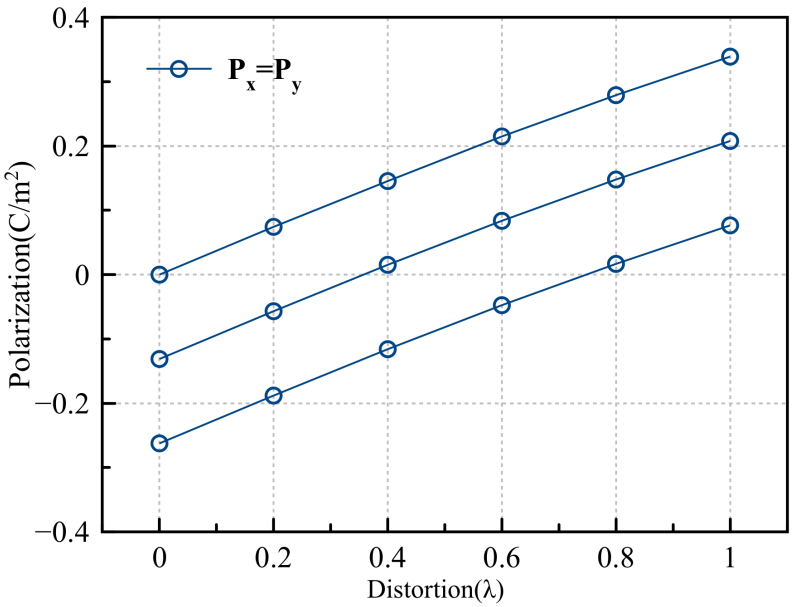

Figure B.3: The x and y components of polarization as a function of lattice distortion for $Pmc2_1$ phase at tensile strain of 2.82% in the NNO thin film.

Appendix C

LIST OF PUBLISHED PAPERS USED IN THIS DISSERTATION

Large parts of Chapters 3, 4, 5, and 6 as well as appendices A and B were originally published as:

(1) 'Atomistic mechanism leading to complex antiferroelectric and incommensurate perovskites', Kinnary Patel, Sergey Prosandeev, Yurong Yang, Bin Xu, Jorge Íñiguez and L. Bellaiche, Physical Review B 94, 054107 (2016).

(2) 'Dynamics of antipolar distortions', Kinnary Patel, Sergey Prosandeev and L. Bellaiche, npj Computational Materials 3, 34 (2017); doi: 10.1038/s41524-017-0033 (Nature).

(3) 'Temperature dependence of polar modes in hybrid improper ferroelectrics', Kinnary Patel, Sergey Prosandeev, Bin Xu and L. Bellaiche, Physical Review B, 100, 212107 (2019).

(4) 'Properties of (001) $NaNbO_3$ films under epitaxial strain: a first principles study', Kinnary Patel, Sergey Prosandeev, Bin, Xu, Changsong Xu, and L. Bellaiche, Physical Review B, 103, 094103 (2021).

Appendix D

COPYRIGHT INFORMATION

American Physical Society
Reuse and Permissions License

25-Feb-2021

This license agreement between the American Physical Society ("APS") and Kinnary Patel ("You") consists of your license details and the terms and conditions provided by the American Physical Society and SciPris.

Licensed Content Information

License Number:	**RNP/21/FEB/036965**
License date:	25-Feb-2021
DOI:	10.1103/PhysRevB.94.054107
Title:	Atomistic mechanism leading to complex antiferroelectric and incommensurate perovskites
Author:	Kinnary Patel et al.
Publication:	Physical Review B
Publisher:	American Physical Society
Cost:	USD $ 0.00

Request Details

Does your reuse require significant modifications: No

Specify intended distribution locations:	United States
Reuse Category:	Reuse in a thesis/dissertation
Requestor Type:	Student
Items for Reuse:	Whole Article
Format for Reuse:	Electronic and Print
Total number of print copies:	Up to 1000

Information about New Publication:

University/Publisher:	University of Arkansas
Title of dissertation/thesis:	Static and dynamics study of complex antiferroelectrics materials
Author(s):	Kinnary Y Patel
Expected completion date:	May. 2021

License Requestor Information

Name:	Kinnary Patel
Affiliation:	Individual
Email Id:	kypatel@uark.edu
Country:	United States

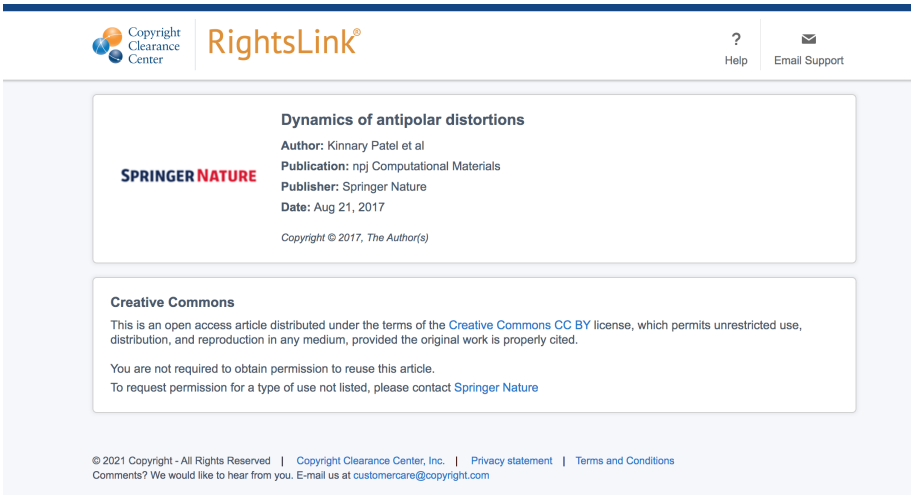

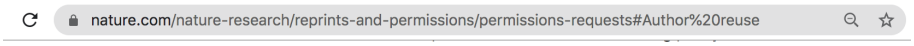

details: http://www.nature.com/authors/policies/license.html

Author reuse

Authors have the right to reuse their article's Version of Record, in whole or in part, in their own thesis. Additionally, they may reproduce and make available their thesis, including Springer Nature content, as required by their awarding academic institution.

Authors must properly cite the published article in their thesis according to current citation standards.

Material from: 'AUTHOR, TITLE, JOURNAL TITLE, published [YEAR], [publisher - as it appears on our copyright page]'

If you are any doubt about whether your intended re-use is covered, please contact journalpermissions@springernature.com for confirmation.

Get permission to reuse Springer Nature content online

Springer Nature is partnered with the Copyright Clearance Center to meet our customers' licensing and permissions needs.

Copyright Clearance Center's RightsLink® service makes it faster and easier to secure permission for the reuse of Springer Nature content.

American Physical Society
Reuse and Permissions License

25-Feb-2021

This license agreement between the American Physical Society ("APS") and Kinnary Patel ("You") consists of your license details and the terms and conditions provided by the American Physical Society and SciPris.

Licensed Content Information

License Number:	**RNP/21/FEB/036967**
License date:	25-Feb-2021
DOI:	10.1103/PhysRevB.100.214107
Title:	Temperature dependence of polar modes in hybrid improper ferroelectrics
Author:	Kinnary Patel et al.
Publication:	Physical Review B
Publisher:	American Physical Society
Cost:	USD $ 0.00

Request Details

Does your reuse require significant modifications: No

Specify intended distribution locations:	United States
Reuse Category:	Reuse in a thesis/dissertation
Requestor Type:	Student
Items for Reuse:	Whole Article
Format for Reuse:	Print and Electronic
Total number of print copies:	Up to 1000

Information about New Publication:

University/Publisher:	University of Arkansas
Title of dissertation/thesis:	Static and dynamics study of complex antiferroelectrics materials
Author(s):	Kinnary Y Patel
Expected completion date:	May. 2021

License Requestor Information

Name:	Kinnary Patel
Affiliation:	Individual
Email Id:	kypatel@uark.edu
Country:	United States

American Physical Society
Reuse and Permissions License

15-Mar-2021

This license agreement between the American Physical Society ("APS") and Kinnary Patel ("You") consists of your license details and the terms and conditions provided by the American Physical Society and SciPris.

Licensed Content Information

License Number:	**RNP/21/MAR/037636**
License date:	15-Mar-2021
DOI:	10.1103/PhysRevB.103.094103
Title:	Properties of (001) ${\mathrm{NaNbO}}_{3}$ films under epitaxial strain: A first-principles study
Author:	Kinnary Patel et al.
Publication:	Physical Review B
Publisher:	American Physical Society
Cost:	USD $ 0.00

Request Details

Does your reuse require significant modifications: No

Specify intended distribution locations:	United States
Reuse Category:	Reuse in a thesis/dissertation
Requestor Type:	Author of requested content
Items for Reuse:	Whole Article
Format for Reuse:	Print and Electronic
Total number of print copies:	Up to 1000

Information about New Publication:

University/Publisher:	University of Arkansas
Title of dissertation/thesis:	Static and dynamics study of complex antiferroelectrics materials
Author(s):	Kinnary Patel
Expected completion date:	May. 2021

License Requestor Information

Name:	Kinnary Patel
Affiliation:	Individual
Email Id:	kypatel@uark.edu
Country:	United States